



**COHERENT THERMAL EMISSION FROM PHOTONIC NANOSTRUCTURES  
COMPOSED OF TA, W, GE, AND HFO<sub>2</sub> THIN FILMS**

**THESIS**

Mark T. Dodd, Mr., Civilian  
AFIT-ENP-MS-15-M-258

**DEPARTMENT OF THE AIR FORCE  
AIR UNIVERSITY**

***AIR FORCE INSTITUTE OF TECHNOLOGY***

---

---

**Wright-Patterson Air Force Base, Ohio**

**DISTRIBUTION STATEMENT A.**  
APPROVED FOR PUBLIC RELEASE; DISTRIBUTION UNLIMITED.

The views expressed in this thesis are those of the author and do not reflect the official policy or position of the United States Air Force, Department of Defense, or the United States Government. This material is declared a work of the U.S. Government and is not subject to copyright protection in the United States.

AFIT-ENP-MS-15-M-258

COHERENT THERMAL EMISSION FROM PERIODIC NANOSTRUCTURES  
COMPOSED OF TA, W, GE, AND HFO<sub>2</sub> THIN FILMS

THESIS

Presented to the Faculty

Department of Engineering and Physics

Graduate School of Engineering and Management

Air Force Institute of Technology

Air University

Air Education and Training Command

In Partial Fulfillment of the Requirements for the  
Degree of Master of Science in Optical Sciences & Engineering

Mark T. Dodd

Mr., Civilian

March 2015

**DISTRIBUTION STATEMENT A.**  
APPROVED FOR PUBLIC RELEASE; DISTRIBUTION UNLIMITED.

AFIT-ENP-MS-15-M-258

COHERENT THERMAL EMISSION FROM PHOTONIC NANOSTRUCTURES

COMPOSED OF TA, W, GE, AND HFO<sub>2</sub> THIN FILMS

Mark T. Dodd  
Mr., Civilian

Committee Membership:

Dr. M. A. Marciniak  
Chair

Dr. J. G. Jones  
Member

Maj M. D. Seal, PhD  
Member

### **Abstract**

Combining an understanding of thin films and structure/property relationships, photonic nano-structured designs were developed in order to affect the spectral and directional radiative properties of coherent thermal emission. The targeted emission range consisted of wavelengths from the short-wave infrared (SWIR, 1.4-3  $\mu\text{m}$ ) to the long-wave infrared (LWIR, 8-15  $\mu\text{m}$ ). Structures with appropriate materials in order to achieve thermal stability were designed for and tested. Using Lumerical's FDTD Solutions software package which implements a Finite Difference Time Domain (FDTD) numerical method, four truncated multilayer resonators were designed to selectively emit at certain transmissive and absorptive wavelength bands in the SWIR to LWIR range. Ellipsometric measurements and models were used in order to extract the optical constants of thin layers of materials chosen for the resonator designs. These values showed significant disagreement with bulk values found in literature and were used to make more accurate theoretical predictions. A Direct Current Magnetron Sputtering (DCMS) technique was used to fabricate the four resonators, tungsten-germanium-tungsten (W-Ge-W), tungsten-hafnium oxide-tungsten (W-HfO<sub>2</sub>-W), tantalum-germanium-tantalum (Ta-Ge-Ta), and tantalum-hafnium oxide-tantalum (Ta-HfO<sub>2</sub>-Ta), with layer thicknesses of 10-760-145 nanometers (nm), 10-701-145 nm, 9.6-728-169 nm, and 9.6-301-169 nm, respectively. The thicknesses of each sample were analyzed using an in-situ ellipsometer upon deposition. Reflectance measurements showed good agreement with the theoretical values except when dealing with absorption features due to the dielectric layer. Also,

reflectance measurements were taken at various high temperatures to investigate the thermal stability of the spectral reflectance of the structures. From these reflectance measurements, the W-Ge-W (10-760-145 nm) and Ta-Ge-Ta (9.6-728-169 nm) designs proved to hold up at higher temperatures better than the other designs.

## Acknowledgments

First, I would like to thank my Creator and Savior, Jesus Christ, who created every aspect of this wonderful universe and gave me the abilities and opportunities to study it.

Secondly, I would like to express my sincere appreciation to my faculty advisor, Dr. Michael Marciniak, for his guidance and support throughout the course of this thesis. His time, insight, and experience were certainly appreciated. I would also like to thank DAGSI for funding this research effort and financially providing for a large amount of my time at AFIT. I would also like to express my appreciation to the members of my thesis committee, Maj Michael Seal and Dr. John Jones, for their support and involvement in this research effort and my time here at AFIT. I would especially like to thank AFRL materials and manufacturing directorate for providing the resources and access to their equipment, such as their PVD Research and Optical Materials Chamber, Infrared-Variable Angle Spectroscopic Ellipsometer (IR-VASE), and Scanning Electron Micrograph (SEM). I would like to thank my family and friends that have supported and helped me through my journey here at AFIT. Lastly, I would like to express my appreciation to the following individuals who have helped make this research possible with their help, advice, and expertise:

- Dr. Kurt Eyink, Ellipsometry and Materials
- Dr. John Jones, Fabrication and Materials
- Mrs. Kathleen Shugart, SEM
- Maj Michael Seal, FDTD Method

Mark T. Dodd

## Table of Contents

	Page
Abstract .....	v
Table of Contents .....	viii
List of Figures .....	x
List of Tables .....	xix
List of Symbols .....	xx
List of Abbreviations .....	xxiv
 I. Introduction .....	 1
General Issue .....	1
Relevant Research .....	3
Problem Statement.....	6
Importance.....	6
Methodology.....	7
Limitations.....	8
Overview .....	9
 II. Theoretical Background .....	 10
Chapter Overview.....	10
Conventions .....	10
Conservation of Energy .....	11
Electromagnetic Theory .....	13
Design of a Thermal Emitter .....	16
Finite Difference Time Domain (FDTD) Analysis .....	17
Reflectance .....	23
Spectroscopic Ellipsometry .....	24
Summary.....	29
 III. Methodology .....	 30
Chapter Overview.....	30
Truncated Multilayer Resonator.....	30
Constituent Material Properties.....	31
<i>Complex Refractive Index</i> .....	31
<i>Skin Depth</i> . ....	42
Fabrication.....	44
Ellipsometric and Reflectance Measurements.....	45
Summary.....	47



IV. Analysis and Results.....	48
Chapter Overview.....	48
Truncated Resonator Design .....	48
Dimensional Analysis.....	49
Spectroscopic Ellipsometry.....	55
Sample 1 (W-HfO <sub>2</sub> -W 10-701-145nm).....	65
Fabrication Results.....	65
Reflectance Measurements.....	67
Sample 2 (Ta-HfO <sub>2</sub> -Ta 9.6-301-169nm).....	74
Fabrication Results.....	74
Reflectance Measurements.....	75
Sample 3 (W-Ge-W 10-760-145nm).....	80
Fabrication Results.....	80
Reflectance Measurements.....	81
Sample 4 (Ta-Ge-Ta 9.6-728-169nm).....	87
Fabrication Results.....	87
Reflectance Measurements.....	88
Summary.....	90
V. Conclusions.....	94
Conclusions of Research .....	94
Recommendations for Future Research.....	97
Appendix A. Linear Plots of Theoretical Emittance of Ta & W Structures .....	100
Bibliography .....	118

## List of Figures

Figure	Page
1. Comparison (p-pol) between the theoretical emittance results (left and experimental emittance results (right) found through measurements taken using a J. A. Woollam Infrared Variable Angle Spectroscopic Ellipsometry (IR-VASE) for a Ag-Ge-Ag structure with thicknesses 6-240-160 nm, respectively. Taken from [31] .....	4
2. Comparison (p-pol) between new theoretical emittance predictions that include derived optical constants (n and k) for the sputter-deposited materials (left) to those calculated (right) from the measurements taken using a J. A. Woollam Infrared Variable Angle Spectroscopic Ellipsometer (IR-VASE) for a Ag-Ge-Ag resonating structure with thicknesses 6-240-160 nm, respectively. Taken from [31] .....	4
3. Scanning Electron Micrograph (SEM) of a Ag-Ge-Ag truncated resonator (6-240-160 nm) on a silicon substrate before (left) and after (right) heating to 400 K. Ag and Ge layers were deposited via a High Power Impulse Magnetron Sputtering (HIPIMS) technique. Both were taken at 100,00x magnification. The pre- and post-heat micrographs were taken at 52° and 35° (left) from surface normal, respectively. Taken from [31] .....	5
4. Illustration of the propagation of radiation being emitted from a lambertian surface in spherical coordinates. The zenith, $\theta$ , and the azimuth, $\phi$ , angles measured using the coordinate system constructed from the surface normal in the $\hat{z}$ direction.....	13
5. Illustration of an optical system that includes a Fabry-Perot etalon. The system creates a pattern of concentric bright and dark rings that indicate constructive and destructive interference from a diffuse, broadband source. The lens on the left of the etalon collimates the source and the lens on the right focuses the beam leaving the etalon to a point on the screen. d is the spacing between the reflectors, n is the index of the medium in the space, and $\theta$ is the angle which the light travels through the etalon. ....	15
6. Concentric ring interference pattern created on the screen due to the multiple reflections from the etalon and focusing lens .....	16
7. Spectral transmittance of the atmosphere when observing an object at medium altitude (about 6km) on a clear, mid-summer day with normal visibility (about 23km) computed using the software package MODTRAN .....	17

8. Yee cell, representing local curl of the fields, used by FDTD numerical method to solve Maxwell's equations .....	19
9. Illustration of incident radiation (red ray) on a surface from a specific direction defined by the elevation angle $\theta$ and azimuthal angle $\phi$ that scatters into a hemisphere (blue rays) .....	24
10. Illustration of truncated multilayer resonator, which is defined as a structure which contains a transparent layer between an optically thin reflective layer and an optically thick layer. The thin reflective layer is exposed to the incident radiation .....	31
11. Spectral absorption coefficients for silver (Ag) [blue], Tungsten (W) [red dash], Tantalum (Ta) [black dash-dot], and Gold (Au) [green]. Properties from [46, 51, 58] .....	32
12. Spectral reflectivity of Ag (blue), W (black dash-dot), Ta (red dash), Au (green), Al (blue dots), and Cu (black dots) as computed by the Fresnel equations for normal incidence .....	34
13. Real ( $\epsilon_1$ ) and imaginary ( $\epsilon_2$ ) parts of the complex dielectric function of tungsten at 294 K (room temperature), 1100 K, 1600 K as calculated from the Drude model, Eq (25), with the measured optical parameters in Table 1 from [67]......	37
14. Complex refractive index for tungsten where $n$ is the real part and $k$ is the imaginary. Values were obtained using the Drude model, Eq (25), with the measured optical parameters in Table 1 from [67] at 294 K, 1100 K, and 1600 K and plotted with measured values reported in Palik [38]......	39
15. Index of refraction for Germanium using temperature dependent Sellmeier equation compared to measured values taken at 500K as reported by Li [77]. .....	42
16. Graphical illustration of the wavelength dependence of the skin depth for silver, tungsten, tantalum, and gold. The optical properties ( $n$ , $k$ ) used for these metals are taken from Palik [46], CRC [51], and Rakic [58] .....	43
17. Illustration of incident hemispherical radiation (blue rays) on a surface where reflected radiation (red ray) is measured at a specific direction defined by the elevation angle $\theta$ and azimuthal angle $\phi$ .....	47
18. Comparison of the theoretical angular emittance spectra for a p-pol source on a Ta-HfO <sub>2</sub> -Ta truncated resonator with varying thicknesses of 6nm (top left), 10nm (top right), 20nm (middle), 30nm (bottom left), and 40nm (bottom right) for the top, optically thin Ta layer .....	52

19. Comparison of the theoretical angular emittance (color bar) spectra for a p-pol source on a Ta-HfO <sub>2</sub> -Ta truncated resonator with varying thicknesses for the middle transparent HfO <sub>2</sub> layer of 300nm (top left), 700nm (top right), 1μm (middle), 1.5μm (bottom left), and 2μm (bottom right). .....	53
20. Comparison of the angle-independent theoretical emittance spectra for a p-pol source on a Ta-HfO <sub>2</sub> -Ta truncated resonator with varying thicknesses of 6 nm, 10 nm, 20 nm, 30 nm, and 40 nm for the top, optically thin W layer .....	53
21. Comparison of the angle-independent theoretical emittance spectra for a p-pol source on a Ta-HfO <sub>2</sub> -Ta truncated resonator with varying thicknesses of 150 nm, 300 nm, 700 nm, and 1 μm for the middle, transparent HfO <sub>2</sub> layer .....	54
22. Amplitude ratio $\psi$ (green) and phase difference $\Delta$ (blue) of ellipsometric measurements made using the J. A. Woollam Infrared Variable Angle Spectroscopic Ellipsometer (IR-VASE) for incident angles of 69°, 71°, and 73° on an optically thick layer of W (145 nm) with associated model fits (red). Error in the measured and modeled values are plotted as error-bars.....	57
23. Amplitude ratio $\psi$ (green) and phase difference $\Delta$ (blue) of ellipsometric measurements made using the J. A. Woollam Infrared Variable Angle Spectroscopic Ellipsometer (IR-VASE) for incident angles of 69°, 71°, and 73° on an optically thin layer of W (~10 nm) with associated model fits (red). Error in the measured and modeled values are plotted as error-bars.....	58
24. Measured real (n) and imaginary (k) parts of index of refraction for DCMS-deposited optically thin, 10 nm, (blue) and thick, 145 nm, (black) W compared with error-bars plotted against bulk optical constants reported in Palik [45] (red) and used in the Lumerical FDTD Solutions software .....	59
25. Measured real (n) and imaginary (k) parts of index of refraction for DCMS-deposited optically thin (10 nm) and opaque (170 nm) Ta layers with error-bars compared against bulk optical constants reported in CRC [46] (red) and used in Lumerical FDTD Solutions solutions.....	60
26. Measured (blue) real (n) and imaginary (k) parts of index of refraction for DCMS-deposited Ge layer (300 nm) with error-bars compared against bulk optical constants reported in Palik [50] (red) and used in Lumerical FDTD Solutions solutions .....	62
27. Measured (blue) real (n) and imaginary (k) parts of index of refraction for DCMS-deposited HfO <sub>2</sub> layers with error-bars compared against bulk optical constants reported by Lts Research Lab [63] (red) .....	62

28. Theoretical emittance values for W-HfO <sub>2</sub> -W 6-700-200 nm obtained using the enhanced transmission matrix approach with extracted optical constants from ellipsometric models for W (10nm) and HfO <sub>2</sub> (300nm) layers .....	63
29. Theoretical emittance values for Ta-HfO <sub>2</sub> -Ta 6-700-200 nm obtained using the enhanced transmission matrix approach with extracted optical constants from ellipsometric models for Ta (10nm) and HfO <sub>2</sub> (300nm) layers .....	64
30. Theoretical emittance values for W-Ge-W 6-700-200 nm obtained using the enhanced transmission matrix approach with extracted optical constants from ellipsometric models for W (10nm) and Ge (300nm) layers .....	64
31. Theoretical emittance values for Ta-Ge-Ta 6-700-200 nm obtained using the enhanced transmission matrix approach with extracted optical constants from ellipsometric models for Ta (10nm) and Ge (300nm) layers .....	65
32. SEM of a pre-heated W-HfO <sub>2</sub> -W truncated resonator of dimensions 10-701-145 nm on a silicon substrate. The W and HfO <sub>2</sub> layers were deposited using the Direct Current Magnetron Sputtering (DCMS) technique. The micrograph was taken at 20,000x magnification with 2 kV at 45° from surface normal .....	66
33. Measured (top left) and theoretical emittance values for W-HfO <sub>2</sub> -W structure with designed thicknesses (6-700-200 nm, top right) and estimated thicknesses after fabrication (10-701-145 nm, bottom right) obtained using the enhanced transmission matrix approach with extracted optical constants from ellipsometric models for W (10nm) and HfO <sub>2</sub> (300nm). Emittance values for an incidence angle of 25° for both theoretical models and what was measured are plotted together (bottom left).....	69
34. Inferred angular HDR emittance for p-pol source on a HfO <sub>2</sub> -W structure of dimensions 303-145 nm at room temperature.....	70
35. Inferred angular HDR emittance for p-pol source on a W-HfO <sub>2</sub> -W structure of dimensions 10-701-145 nm at 80°C (top left), 130°C (top right), 180°C (middle), 230°C (bottom left), and 280°C (bottom right).....	71
36. Inferred angular HDR emittance for p-pol source on a W-HfO <sub>2</sub> -W structure of dimensions 10-701-145 nm for incident angles 15° (top left), 35° (top right), 45° (middle left), 55° (middle right), 65° (bottom left), 75° (bottom right) at temperatures 80°C, 130°C, 180°C, 230°C, 280°C, and 330°C .....	72
37. SEM of a W-HfO <sub>2</sub> -W truncated resonator of dimensions 10-701-145 nm on a silicon substrate after heating to temperatures up to about 550 K. The W and HfO <sub>2</sub> layers were deposited using the Direct Current Magnetron Sputtering (DCMS) technique.	

The micrograph was taken at 20,000x magnification with 5 kV at 45° from surface normal .....	73
38. SEM of a pre-heated Ta-HfO <sub>2</sub> -Ta truncated resonator of dimensions 9.6-301-169 nm on a silicon substrate. The Ta and Ge layers were deposited using the Direct Current Magnetron Sputtering (DCMS) technique. The micrograph was taken at 20,000x magnification with 2 kV at 45° from surface normal .....	75
39. Measured (top left) and theoretical emittance values for Ta-HfO <sub>2</sub> -Ta structure with designed thicknesses (6-300-200 nm, top right) and estimated thicknesses after fabrication (9.6-301-169 nm, bottom right) obtained using the enhanced transmission matrix approach with extracted optical constants from ellipsometric models for W (10nm) and HfO <sub>2</sub> (300nm). Emittance values for an incidence angle of 25° for both theoretical models and what was measured are plotted together (bottom left).....	76
40. Inferred angular HDR emittance for p-pol source on a Ta-HfO <sub>2</sub> -Ta structure of dimensions 9.6-301-169 nm at 80°C (top left), 130°C (top right), 180°C (middle left), 230°C (middle right), 280°C (bottom left), and 330°C (bottom right) .....	78
41. Inferred angular HDR emittance for p-pol source on a Ta-HfO <sub>2</sub> -Ta structure of dimensions 9.6-301-169 nm for incident angles 15° (top left), 35° (top right), 45° (middle left), 55° (middle right), 65° (bottom left), 75° (bottom right) at temperatures 80°C, 130°C, 180°C, 230°C, 280°C, and 330°C .....	79
42. SEM of a Ta-HfO <sub>2</sub> -Ta truncated resonator of dimensions 9.6-301-169 nm on a silicon substrate after heating to temperatures up to about 600 K. The Ta and Ge layers were deposited using the Direct Current Magnetron Sputtering (DCMS) technique. The micrograph was taken at 35,000x magnification with 2 kV at 45° from surface normal .....	80
43. SEM of a pre-heated W-Ge-W truncated resonator of dimensions 10-760-145 nm on a silicon substrate. The W and Ge layers were deposited using the Direct Current Magnetron Sputtering (DCMS) technique. The micrograph was taken at 20,000x magnification with 5 kV at 45° from surface normal .....	81
44. Measured (top left) and theoretical emittance values for W-Ge-W structure with designed thicknesses (6-700-200 nm, top right) and estimated thicknesses after fabrication (10-760-145 nm, bottom right) obtained using the enhanced transmission matrix approach with extracted optical constants from ellipsometric models for W (10nm) and Ge (300nm). Emittance values for an incidence angle of 25° for both theoretical models and what was measured are plotted together (bottom left).....	82

45. Inferred angular HDR emittance for p-pol source on a W-Ge-W structure of dimensions 10-760-145 nm at 80°C (top left), 130°C (top right), 180°C (middle left), 230°C (middle right), 280°C (bottom left), and 330°C (bottom right) .....	84
46. Inferred angular HDR emittance for p-pol source on a W-Ge-W structure of dimensions 10-760-145 nm for incident angles 15° (top left), 35° (top right), 45° (middle left), 55° (middle right), 65° (bottom left), 75° (bottom right) at temperatures 80°C, 130°C, 180°C, 230°C, 280°C, and 330°C .....	85
47. SEM of a W-Ge-W truncated resonator of dimensions 10-760-145 nm on a silicon substrate after heating to temperatures up to about 600 K. The W and Ge layers were deposited using the Direct Current Magnetron Sputtering (DCMS) technique. The micrograph was taken at 20,000x magnification with 5 kV at 45° from surface normal .....	86
48. SEM of a pre-heated Ta-Ge-Ta truncated resonator of dimensions 9.6-728-169 nm on a silicon substrate. The Ta and Ge layers were deposited using the Direct Current Magnetron Sputtering (DCMS) technique. The micrograph was taken at 35,000x magnification with 2 kV at 45° from surface normal .....	87
49. Measured (top left) and theoretical emittance values for W-Ge-W structure with designed thicknesses (6-700-200 nm, top right) and estimated thicknesses after fabrication (10-760-145 nm, bottom right) obtained using the enhanced transmission matrix approach with extracted optical constants from ellipsometric models for W (10nm) and Ge (300nm). Emittance values for an incidence angle of 25° for both theoretical models and what was measured are plotted together (bottom left) .....	89
50. Inferred angular HDR emittance for p-pol source on a Ta-Ge-Ta structure of dimensions 9.6-728-169 nm at 80°C (top left), 130°C (top right), 180°C (middle left), 230°C (middle right), 280°C (bottom left), and 330°C (bottom right) .....	91
51. Inferred angular HDR emittance for p-pol source on a Ta-Ge-Ta structure of dimensions 9.6-728-169 nm for incident angles 15° (top left), 35° (top right), 45° (middle left), 55° (middle right), 65° (bottom left), 75° (bottom right) at temperatures 80°C, 130°C, 180°C, 230°C, 280°C, and 330°C .....	92
52. SEM of a Ta-Ge-Ta truncated resonator of dimensions 9.6-728-169 nm on a silicon substrate after heating to temperatures up to about 600 K. The Ta and Ge layers were deposited using the Direct Current Magnetron Sputtering (DCMS) technique. The micrograph was taken at 20,000x magnification with 2 kV at 45° from surface normal .....	93

53. Inferred angular HDR emittance for p-pol source on a Ta-Ge-Ta structure of dimensions 9.6-728-169 nm at room temperature plotted with atmospheric transmittance (dotted line).....	96
54. Graphical representation of a metal slab with a periodic lattice of holes with period $\Lambda$ for the excitation of SPPs. $\vec{k}_0$ is the wave vector of the incident light, $\vec{k}_x$ and $\vec{k}_y$ are the components of the incident radiation parallel to the surface interface. Taken from [84] .....	98
55. Calculated SPP modes for the extraordinary transmission filter with $\Lambda = 2.08 \mu\text{m}$ where $\phi_{inc} = 0^\circ$ (right) and $\phi_{inc} = 45^\circ$ (left). In parentheses are the mode order ( $i, j$ ) and $m$ is the Wood's anomaly modes. Taken from and see [84] for more information. ....	99
56. Theoretically inferred total emittance for p-pol source on a Ta-HfO <sub>2</sub> -Ta 6-700-160nm structure simulated using Lumerical FDTD Solutions. ....	100
57. Theoretically inferred total emittance for p-pol source on a Ta-HfO <sub>2</sub> -Ta 10-700-160nm structure simulated using Lumerical FDTD Solutions .....	100
58. Theoretically inferred total emittance for p-pol source on a Ta-HfO <sub>2</sub> -Ta 20-700-160nm structure simulated using Lumerical FDTD Solutions .....	101
59. Theoretically inferred total emittance for p-pol source on a Ta-HfO <sub>2</sub> -Ta 30-700-160nm structure simulated using Lumerical FDTD Solutions .....	101
60. Theoretically inferred total emittance for p-pol source on a Ta-HfO <sub>2</sub> -Ta 40-700-160nm structure simulated using Lumerical FDTD Solutions .....	102
61. Theoretically inferred total emittance for p-pol source on a Ta-HfO <sub>2</sub> -Ta 6-150-160nm structure simulated using Lumerical FDTD Solutions .....	102
62. Theoretically inferred total emittance for p-pol source on a Ta-HfO <sub>2</sub> -Ta 6-300-160nm structure simulated using Lumerical FDTD Solutions .....	103
63. Theoretically inferred total emittance for p-pol source on a Ta-HfO <sub>2</sub> -Ta 6-1um-160nm structure simulated using Lumerical FDTD Solutions .....	103
64. Theoretically inferred total emittance for p-pol source on a Ta-HfO <sub>2</sub> -Ta 6-1.5um-160nm structure simulated using Lumerical FDTD Solutions .....	104
65. Theoretically inferred total emittance for p-pol source on a Ta-HfO <sub>2</sub> -Ta 6-2um-160nm structure simulated using Lumerical FDTD Solutions .....	104



66. Theoretically inferred total emittance for p-pol source on a Ta-HfO <sub>2</sub> -Ta 6-2.5 $\mu$ m-160nm structure simulated using Lumerical FDTD Solutions .....	105
67. Theoretically inferred total emittance for p-pol source on a Ta-Ge-Ta 6-150-160nm structure simulated using Lumerical FDTD Solutions.....	105
68. Theoretically inferred total emittance for p-pol source on a Ta-Ge-Ta 6-300-160nm structure simulated using Lumerical FDTD Solutions.....	106
69. Theoretically inferred total emittance for p-pol source on a Ta-Ge-Ta 6-700-160nm structure simulated using Lumerical FDTD Solutions.....	106
70. Theoretically inferred total emittance for p-pol source on a Ta-Ge-Ta 6-1 $\mu$ m-160nm structure simulated using Lumerical FDTD Solutions.....	107
71. Theoretically inferred total emittance for p-pol source on a Ta-Ge-Ta 6-1.5 $\mu$ m-160nm structure simulated using Lumerical FDTD Solutions .....	107
72. Theoretically inferred total emittance for p-pol source on a Ta-Ge-Ta 6-2 $\mu$ m-160nm structure simulated using Lumerical FDTD Solutions.....	108
73. Theoretically inferred total emittance for p-pol source on a Ta-Ge-Ta 6-2.5 $\mu$ m-160nm structure simulated using Lumerical FDTD Solutions .....	108
74. Theoretically inferred total emittance for p-pol source on a W-Ge-W 6-700-160nm structure simulated using Lumerical FDTD Solutions.....	109
75. Theoretically inferred total emittance for p-pol source on a W-Ge-W 10-700-160nm structure simulated using Lumerical FDTD Solutions.....	109
76. Theoretically inferred total emittance for p-pol source on a W-Ge-W 20-700-160nm structure simulated using Lumerical FDTD Solutions.....	110
77. Theoretically inferred total emittance for p-pol source on a W-Ge-W 30-700-160nm structure simulated using Lumerical FDTD Solutions.....	110
78. Theoretically inferred total emittance for p-pol source on a W-Ge-W 40-700-160nm structure simulated using Lumerical FDTD Solutions.....	111
79. Theoretically inferred total emittance for p-pol source on a W-Ge-W 6-300-160nm structure simulated using Lumerical FDTD Solutions.....	111

80. Theoretically inferred total emittance for p-pol source on a W-Ge-W 6-1um-160nm structure simulated using Lumerical FDTD Solutions.....	112
81. Theoretically inferred total emittance for p-pol source on a W-Ge-W 6-1.5um-160nm structure simulated using Lumerical FDTD Solutions.....	112
82. Theoretically inferred total emittance for p-pol source on a W-Ge-W 6-2um-160nm structure simulated using Lumerical FDTD Solutions.....	113
83. Theoretically inferred total emittance for p-pol source on a W-Ge-W 6-2.5um-160nm structure simulated using Lumerical FDTD Solutions.....	113
84. Theoretically inferred total emittance for p-pol source on a W-HfO <sub>2</sub> -W 6-150-160nm structure simulated using Lumerical FDTD Solutions .....	114
85. Theoretically inferred total emittance for p-pol source on a W-HfO <sub>2</sub> -W 6-300-160nm structure simulated using Lumerical FDTD Solutions .....	114
86. Theoretically inferred total emittance for p-pol source on a W-HfO <sub>2</sub> -W 6-700-160nm structure simulated using Lumerical FDTD Solutions .....	115
87. Theoretically inferred total emittance for p-pol source on a W-HfO <sub>2</sub> -W 6-1um-160nm structure simulated using Lumerical FDTD Solutions .....	115
88. Theoretically inferred total emittance for p-pol source on a W-HfO <sub>2</sub> -W 6-1.5um-160nm structure simulated using Lumerical FDTD Solutions .....	116
89. Theoretically inferred total emittance for p-pol source on a W-HfO <sub>2</sub> -W 6-2um-160nm structure simulated using Lumerical FDTD Solutions .....	116
90. Theoretically inferred total emittance for p-pol source on a W-HfO <sub>2</sub> -W 6-2.5um-160nm structure simulated using Lumerical FDTD Solutions .....	117

## List of Tables

	Page
1. Results of analysis of temperature dependent optical data for tungsten, performed and reported by [67]. ( ) indicates tentative estimates. Conductivities ( $\sigma_1$ , ect.) are in units of $10^6 \text{ ohm}^{-1}\text{m}^{-1}$ . The dc conductivity is $\sigma_0$ . Wavelengths ( $\lambda_{r1}$ , $\lambda_{s1}$ , ect.) are in $\mu m$ .	36
2. Material and Thermal Properties of Crystalline Germanium (Ge) and Hafnium Oxide ( $\text{HfO}_2$ ) from [61-64].	40

## List of Symbols

Symbol

$^{\circ}$	Degree
$\theta$	Incident Zenith
$\phi$	Incident Azimuth
$\psi$	Amplitude Ratio
$\Delta$	Phase Difference
$\alpha$	Absorptance
$\alpha_c$	Attenuation Constant
$\beta$	Phase Variation
$\mu$	Permeability
$\varepsilon$	Emittance, Permittivity
$\varepsilon_1$	Real Part of Complex Dielectric Constant
$\varepsilon_2$	Imaginary Part of Complex Dielectric Constant
$\Phi_{incident}$	Incident Energy
$\Phi_{reflected}$	Reflected Energy
$\Phi_{absorbed}$	Absorbed Energy
$\Phi_{transmitted}$	Transmitted Energy
$\rho$	Reflectance, Complex Reflection Coefficient
$\tau$	Transmittance
$r$	Reflectance
$L$	Radiance

$L_s$	Source Radiance
$L_{BB}$	Blackbody Radiance
$M$	Exitance
$M_s$	Source Exitance
$M_{BB}$	Blackbody Exitance
$T$	Temperature
$h$	Planck's Constant
$c$	Speed of Light in Vacuum
$\lambda$	Wavelength
$\lambda_c$	Center Wavelength
$\omega$	Angular Frequency
$\omega_o$	Initial Angular Frequency
$\omega_p$	Plasma Frequency
$\omega_c$	Collisional Frequency
$\vec{k}$	Propagation Vector
$\vec{r}$	Position Vector
$t$	Time in seconds
$t_o$	Initial time
$k$	Boltzmann's Constant
$z$	Propagation Distance
$\xi, \eta$	Dimensions in Surface Plane
$D$	Aperture Size

$\vec{E}$	Electric Field
$\vec{M}_i$	Impressed Magnetic Current Density
$\vec{B}$	Magnetic Flux Density
$\vec{H}$	Magnetic Field
$\vec{J}_i$	Impressed Magnetic Current Density
$\vec{J}_c$	Conduction Electric Current Density
$\vec{D}$	Electric Flux Density
$q_{ev}$	Electric Charge Density
$q_{mv}$	Magnetic Charge Density
$N$	Complex Refractive Index
$n$	Real Part of Complex Refractive Index
$k$	Imaginary Part of Complex Refractive Index, Extinction Coefficient
sr	Steradian
Si	Silicon
SiC	Silicon Carbide
Ag	Silver
Au	Gold
Na	Sodium
Cu	Copper
K	Potassium
Al	Aluminum

Ge	Germanium
HfO <sub>2</sub>	Hafnium Oxide
W	Tungsten
Ta	Tantalum

## **List of Abbreviations**

### Abbreviation

1-D	One Dimensional
2-D	Two Dimensional
3-D	Three Dimensional
AFIT	Air Force Institute of Technology
AFRL	Air Force Research Laboratory
BC	Boundary Condition
C	Celsius
cm	Centimeter
EM	Electromagnetic
far-IR	Far-Infrared
FDT	Fluctuation-Dissipation Theorem
FDTD	Finite Difference Time Domain
HDR	Hemispherical Directional Reflectance
DCMS	Direct Current Magnetron Sputtering
IR	Infrared
IR-VASE	Infrared Variable Angle Spectroscopic Ellipsometer
K	Kelvin
km	Kilometer
kV	Kilovolt
MODTRAN	Moderate-Resolution Atmospheric Radiance and Transmittance Model



SWIR	Short-Wave Infrared
MWIR	Middle-Wave Infrared
LWIR	Long-Wave Infrared
nm	Nanometer
PC	Photonic Crystal
PML	Perfectly Matched Layer
RMSE	Root Mean Square Error
SE	Spectroscopic Ellipsometry
SEM	Scanning Electron Micrograph
SOC	Surface Optics Corporation
TE	Transverse Electric
TM	Transverse Magnetic
UD	University of Dayton
UV	Ultraviolet
$\mu\text{m}$	Micrometer, Micron
p-pol, p	Parallel-polarized, P-polarized
s-pol, s	Perpendicular-polarized, S-polarized

# **COHERENT THERMAL EMISSION FROM PHOTONIC NANOSTRUCTURES COMPOSED OF TA, W, GE, AND HFO<sub>2</sub> THIN FILMS**

## **I. Introduction**

### **General Issue**

Due to the principle of the conservation of energy, any electromagnetic (EM) radiation that is incident on a surface will have a portion of its energy reflected, transmitted, or absorbed. The portion of the energy that is reflected, transmitted, or absorbed is dependent on the characteristics of the source, medium, and the material properties of the illuminated surface or structure.

Thermal radiation is EM radiation emitted by all matter that has a temperature greater than absolute zero and is due to the thermal motion of charged particles [1]. Thermal radiation includes all wavelengths in the range of 0.1-100 microns ( $\mu\text{m}$ ) [2]. Thermal radiation has a coherence length of approximately one wavelength [3], which means that the frequency, or spacing, of the wave-fronts and the shape of the wave-fronts stay the same for a length equal to one wavelength [4]. Coherence is key to achieving interference effects of multiple wave-fronts. In turn, manipulating wave-fronts to constructively and destructively interfere can be used to create selective reflection and absorption for a particular wavelength and direction.

Many types of optical nano-structures have been investigated to engineer unique radiative properties. Those types of nano-structures that have generated the most interest are metamaterials, photonic crystals (PC), and plasmonic structures. Metamaterials are a

category of engineered structures that have unnatural electromagnetic properties [2, 5-8]. Photonic crystals are structures whose properties vary periodically in one, two, or all three dimensions. The most extensively investigated structure is the one-dimensional (1-D) PC. One-dimensional PCs are usually made of alternating layers with two lossless dielectrics [9]. Many optical nano-structures are designed to take advantage of surface waves in order to achieve spatial and temporal coherence [10-12]. Interference effects from a resonating cavity with highly reflective boundaries can also be utilized to achieve coherent emission [13-16].

There are multi-layer nano-structure designs which incorporate thin layers of material, thin films, which act as optical filters (*e.g.* antireflective coatings) and are used to achieve unique optical properties [17-19]. Mathematically, a thin film is regarded as a plane-parallel layer of essentially infinite extent whose thickness is comparable with the wavelength of light. Thin film optics is a branch of physical optics that deals with the reflection, transmission, and absorption of light by single and multilayer films [20]. It is possible to construct assemblies of thin films which will reduce the reflectance of a surface and increase the transmittance or absorptance of a component [13, 21-29]. While thin films are very attractive and useful in creating structures with unique optical properties, they also present some challenges, especially when dealing with thicknesses on the order of a few hundred nanometers ( $\sim 100\text{nm}$ ). The properties of the material (*e.g.* melting point and optical properties) change as a function of thickness [30-31].

Depending on the application, optical nano-structures designed to be selective thermal absorbers can be expected to operate in environments greater than 1000 K [32].

Therefore, materials that can be used to design thermally stable structures, structures that

can withstand high temperature environments and remain unchanged, are desirable. However, because many of these designs utilize thin films, a greater amount of consideration is needed when choosing the material(s) that will compose the thin layers.

## **Relevant Research**

There have been several nano-structured designs which have been reported to coherently emit thermal radiation in the far field. The simplest design is planar structures. There have been several planar designs ranging from a bi-layer to multilayer structures [13, 15, 22, 24, 33-36]. A majority of the multilayer resonator designs utilize complex reflective layers consisting of Bragg reflectors or photonic crystals [14-16], but there are tri-layer designs that utilize a metal as a reflective coating and boundary in order to form a resonant cavity [32, 37]. Many of these planar cavity designs have achieved coherence based on interference effects [13-16, 24, 33]. None of these emitter designs were tested as a function of temperature, even though selective emitters are expected to operate in high-temperature environments.

In a previous AFIT thesis, one of the most notable designs was done by McConnell [31]. McConnell produced two tri-layer resonators that utilized thin films composed of a silver-germanium-silver (Ag-Ge-Ag) structure. He tested his tri-layer structures for various incidence angles of 15-75° over the wavelength range of 2-20  $\mu\text{m}$  for a parallel-polarized (p-pol) source. Figure 1 shows the theoretical and experimental emittance plotted against angle and wavelength for the structure with dimensions 6-240-160 nm. McConnell reported differences between the spectral location and bandwidth of

his emission peaks of the theoretical model that used bulk material parameters reported by Palik [38] and the experimental results for both structures. He found a closer agreement between the model and experimental results by measuring and deriving the optical properties of the thin layers and utilizing them in the model, see Figure 2.

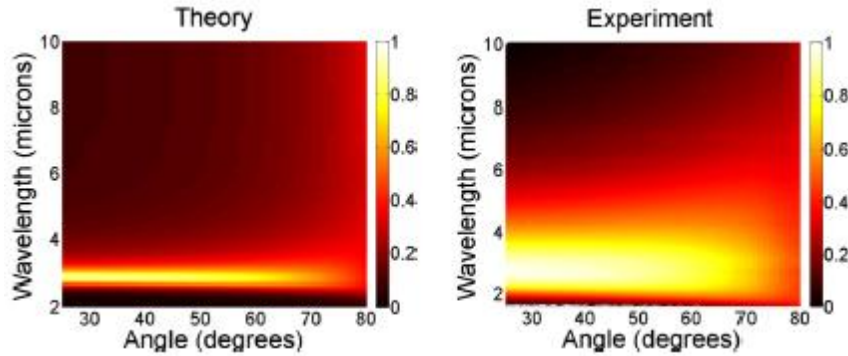


**Figure 1.** Comparison (p-pol) between the theoretical emittance results (left) and experimental emittance results (right) found through measurements taken using a J. A. Woollam Infrared Variable Angle Spectroscopic Ellipsometry (IR-VASE) for a Ag-Ge-Ag structure with thicknesses 6-240-160 nm, respectively. Taken from [31].

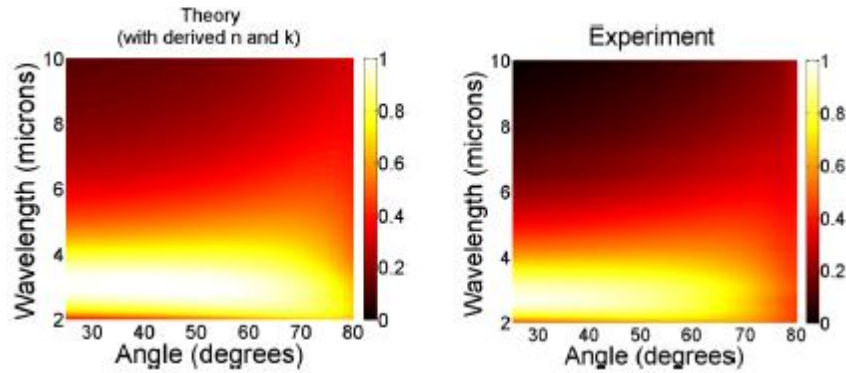


**Figure 2.** Comparison (p-pol) between new theoretical emittance predictions that include derived optical constants ( $n$  and  $k$ ) for the sputter-deposited materials (left) to those calculated (right) from the measurements taken using a J. A. Woollam Infrared Variable Angle Spectroscopic Ellipsometer (IR-VASE) for a Ag-Ge-Ag resonating structure with thicknesses 6-240-160 nm, respectively. Taken from [31]

McConnell also tested the thermal stability of his structures. He found that at temperatures around 400 K and 600 K, there was a 55% and 40% drop in the emittance

and negligible angular sensitivity centered at 2.6  $\mu\text{m}$  and 7.75  $\mu\text{m}$  for the 6-240-160 nm and 6-700-200 nm structures, respectively. He found that the 6 nm surface layer of Ag had partially melted and formed Ag spheres which caused a breakdown in the resonator structures, see Figure 3.

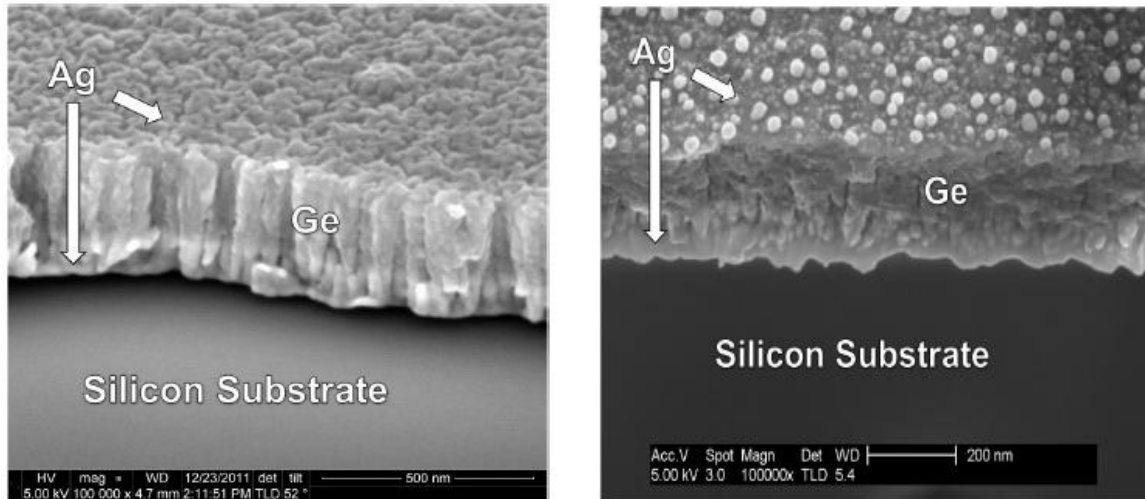


**Figure 3. Scanning Electron Micrograph (SEM) of a Ag-Ge-Ag truncated resonator (6-240-160 nm) on a silicon substrate before (left) and after (right) heating to 400 K. Ag and Ge layers were deposited via a High Power Impulse Magnetron Sputtering (HIPIMS) technique. Both were taken at 100,00x magnification. The pre- and post-heat micrographs were taken at 52° and 35° (left) from surface normal, respectively. Taken from [31]**

There have also been several authors who have demonstrated coherent emission from thermally excited surface waves by using 2-D cavity [32, 37] and grating structures [39], and 3-D structures [40-42]. There is also a reported 2-D grating design that takes advantage of the magnetic polariton to coherently emit thermal radiation [43], alongside of other articles which discuss surface plasmons at metal interfaces and in thin films [44-46].

## **Problem Statement**

In this thesis, the ability to produce and selectively affect the spectral and directional properties of coherent thermal radiation of a structure through use of thin films, nano-structured materials, and an understanding of structure/property relationships of material systems will be explored. The goal of this work is to improve upon McConnell's design which showed, at best, 40% lower emittance at temperatures of 600 K [31]. Therefore, this study is going to focus on a similar design that achieves coherent thermal emission in the farfield, but is thermally stable. During the design phase, materials that show high thermal stability (*e.g.* high melting temperatures, low thermal expansions) are going to be considered and used to construct a resonator that is able to withstand high temperatures. Angular and spectral sensitivities of the emittance to parallel-polarized (p-pol) incident light will be observed at room temperature. Afterwards, the effects of increased temperature, up to 600 K, on spectral emittance will be determined over SWIR and LWIR wavelengths, 2-20  $\mu\text{m}$ .

## **Importance**

Thin films have thicknesses smaller than the wavelength of interest. When considering thermal radiation, which covers wavelengths between 0.1-100  $\mu\text{m}$ , thin films will range from nanometers to a few microns. Photonic nano-structures with layers at this scale can have remarkable reflective properties due to light wave interference and the difference in the refractive index between the deposited layers, the air, and the substrate.

Thin films and optical coatings play an important role in increasing the sensitivity of sensors and detectors, as well as enhancing the performance of a variety of optical components. Everyday examples of thin films include low emissivity panes of glass for windows and cars, anti-reflective coatings on glasses, reflective baffles on car headlights, and high precision optical filters. Thin films have also been used to achieve spatial filtering [18].

This thesis deals with how to design structures that achieve coherent thermal emission in the far-field, and how to utilize the unique properties of thin films in order to affect thermal radiation. Thermal radiation modification has significant applications in the areas of solar cell technology, thermal photovoltaics, and solar absorbers/emitters [13, 24].

## **Methodology**

The design of photonic nanostructures for this work will involve modeling and simulation software based on numerical methods of electromagnetics. Four thermal emitter designs are planned to be fabricated and experimentally analyzed. These designs are four variations on a 1-D multilayer resonator structure. Electromagnetic modeling software will be used to design these multilayer structures.

After performing an initial modeling process, thin films of the desired materials will be deposited using a Direct Current Magnetron Sputtering technique (DCMS). The optical properties of the thin layers in the IR region will be measured using a J. A. Woollam Infrared-Variable Angle Spectroscopic Ellipsometer (IR-VASE). The complex



refractive index,  $n$  and  $k$ , of the layers will be estimated from the IR-VASE measurements. These values will be compared to the bulk parameters reported in literature and used to perform an iteration on the modeling and design process.

After completing the design, fabrication efforts for the 1-D multilayer designs will be accomplished using Air Force Research Laboratory (AFRL) facilities and resources. A DCMS deposition technique will be used to deposit the desired materials. Since the materials that will be analyzed in this study are conductive, this chosen deposition technique is adequate for all of the materials.

Reflectance measurements in the 2-20  $\mu\text{m}$  range will be taken using the Air Force Institute of Technology's (AFIT's) Surface Optics Corporation's instrument (SOC-100) which measures hemispherical-directional reflectance (HDR). This reflectometer also comes with a heater stage that will be utilized to test the thermal stability of the designs by measuring the reflectance at various high temperatures. The results will be analyzed to determine the temperature stability of these designs.

## **Limitations**

In designing engineered structural materials for a specific application, the optical dispersion of each material must be considered so a model describing the structure can be determined. However, the optical dispersion for bulk materials are rarely representative of the dispersion in thin films, and this can lead to a disparity between modeled and experimental results. Measurements of thin films with the IR-VASE are included in this study in order to minimize this disparity. However, the optical properties obtained

through the IR-VASE are only as accurate as the modeling technique used to represent the measured data. The model is limited by the effect of quantizing infinite oscillatory functions which are implemented in characterizing films.

## **Overview**

Chapter II provides a general theoretical background on the key topics involved and discussed in the later chapters. Chapter III describes the methodology used in designing, fabricating, and characterizing the multilayer resonator nanostructures. Chapter IV discusses the effects of changing the material and dimensions of a resonator design, fabrication results of the four resonators, and analyzes the measured data. Chapter V summarizes the work of this study, the importance of its findings, and makes recommendations for possible future work. Appendix A provides supplemental theoretical emittance plots for the dimensional analysis conducted for each design.

## **II. Theoretical Background**

### **Chapter Overview**

This chapter provides an overview of the physics and mathematics which this research is based on. A background on the primary topics that consist of the conservation of energy, electromagnetic (EM) theory, finite difference time domain, reflectance, and ellipsometry is provided. Relevant citations have been provided to supplement a given discussion or offer a resource for a more detailed development of a specific topic.

### **Conventions**

Due to various conventions found in literature, a few assumptions are made here for clarity and consistency. Following the Fresnel convention [47], reflection and transmission will be viewed as general processes, while the numerical measurements made on a sample will be referred to as the reflectance and transmittance. Emissivity is the ratio between the exitance of the source and the exitance of a blackbody at the same temperature. In this work, emittance will be used exclusively in order to avoid confusion between “emittance” and “emissivity”.

Also, a distinction between transverse electric (TE) and transverse magnetic (TM) linear polarizations must be made. In electromagnetics, TE or TM waves refer to field configurations whose electric or magnetic field components are transverse to the direction of propagation [8]. In physics, a Fresnel convention is used where a TE and TM wave refers to a field configuration where the electric field components are orthogonal or

parallel, respectively, to the plane of incidence [47,48]. To avoid confusion, the Fresnel convention for linearly polarized waves will be assumed for this thesis.

### Conservation of Energy

In an isolated system, energy is always conserved over time. Assuming a structure is held in thermal equilibrium with its environment, conservation of energy requires that the incident flux ( $\Phi_{incident}$ ) which is energy per unit time be either reflected ( $\Phi_{reflected}$ ), absorbed ( $\Phi_{absorbed}$ ), or transmitted ( $\Phi_{transmitted}$ )

$$\Phi_{incident} = \Phi_{reflected} + \Phi_{absorbed} + \Phi_{transmitted} . \quad (1)$$

Dividing both sides by the incident flux ( $\Phi_{incident}$ ) results in

$$1 = \rho + \alpha + \tau \quad (2)$$

where  $\rho$  is the reflectance,  $\alpha$  is the absorptance, and  $\tau$  is the transmittance. An opaque structure is defined as a boundary which blocks the passage of radiant energy and has a theoretical transmittance of zero. Therefore, assuming the structure is opaque produces

$$1 = \rho + \alpha . \quad (3)$$

According to Kirchhoff's law of thermal radiation, if a material body is held in thermal equilibrium, then all the energy which is absorbed by the body is re-emitted, or

$$\alpha = \varepsilon \quad (4)$$

where  $\varepsilon$  is the emittance. By substitution, the following equation can be found for emittance

$$\varepsilon = 1 - \rho . \quad (5)$$

It is well-known that when dealing with radiation in the far-field, a blackbody source follows a Planckian distribution for its radiance. Spectral radiance ( $L$ ) is the amount of power radiated per unit projected source area, per unit solid angle leaving a surface, per wavelength

$$L(\lambda, T) = \frac{2hc^2}{\lambda^5(e^{hc/\lambda kT} - 1)} \left[ \frac{\text{watt}}{\text{cm}^2 - \text{sr} - \mu\text{m}} \right], \quad (6)$$

where  $T$  is the source temperature,  $h$  is Planck's constant,  $c$  is the speed of light in a vacuum,  $\lambda$  is the wavelength, and  $k$  is Boltzmann's constant. Exitance ( $M$ ) is the amount of power per unit area that leaves a surface and is related to the radiance by

$$M(\lambda, T) = \iint L(\lambda, T) \cos\theta \sin\theta d\theta d\phi \left[ \frac{\text{watt}}{\text{cm}^2 - \mu\text{m}} \right], \quad (7)$$

where  $\theta$  is the radiated zenith angle,  $\phi$  is the radiated azimuthal angle. Assuming that the source is Lambertian and that the power leaving the surface is radiated equally into a hemisphere, as illustrated in Figure 4, then

$$M(\lambda, T) = \pi L(\lambda, T) \left[ \frac{\text{watt}}{\text{cm}^2 - \mu\text{m}} \right]. \quad (8)$$

Emissivity is defined as the ratio between the exitance of the actual source and that of a blackbody at the same temperature [5]. Therefore, emissivity is always less than one and can be defined as follows,

$$\varepsilon(\lambda, T) = \frac{M_s(\lambda, T)}{M_{BB}(\lambda, T)}. \quad (9)$$

Given the previously stated conditions, Lambertian source and uniform distribution into a hemisphere, then

$$\varepsilon(\lambda, T) = \frac{L_s(\lambda, T)}{L_{BB}(\lambda, T)}, \quad (10)$$

where  $L_s$  is the source radiance,  $L_{BB}$  is the blackbody radiance,  $\lambda$  is the wavelength, and  $T$  is the source temperature. A blackbody source will always have an emissivity  $\varepsilon = 1$  for all wavelengths. A selective emitter is a source whose emittance is dependent on wavelength.

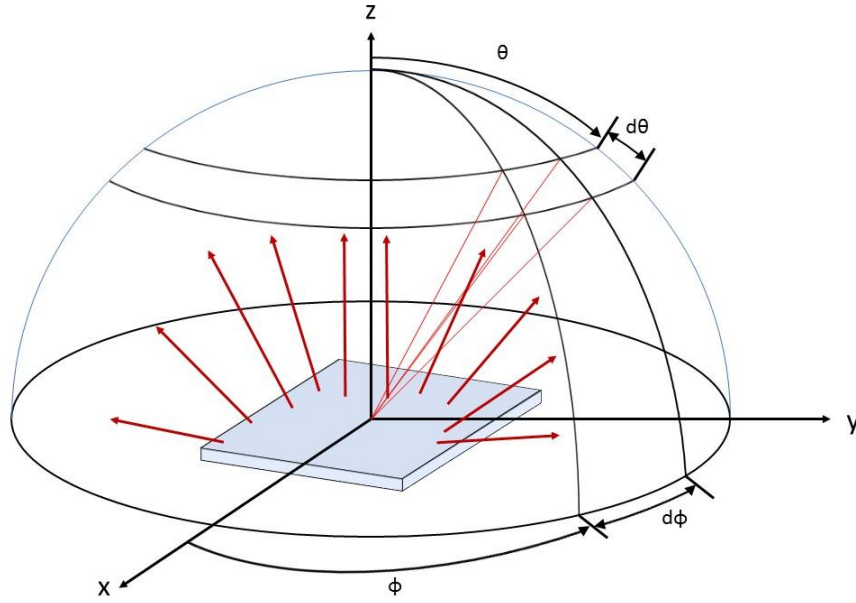


**Figure 4. Illustration of the propagation of radiation being emitted from a lambertian surface in spherical coordinates. The zenith,  $\theta$ , and the azimuth,  $\phi$ , angles measured using the coordinate system constructed from the surface normal in the  $\hat{z}$  direction.**

### Electromagnetic Theory

The far-field is considered when the distance away from a source is much greater than a wavelength. This is also known as the Fraunhofer Approximation and its range as defined by Goodman [5:74] is

$$z \gg \frac{\pi(\xi^2 + \eta^2)_{max}}{\lambda}, \quad (11)$$

where  $\xi, \eta$  are source-plane dimensions and  $z$  is the distance away from the source plane. The max value of  $\xi^2 + \eta^2$  corresponds to the coherence length of the source. For a thermal source, the coherence length is approximately one wavelength [3],  $(\xi^2 + \eta^2)_{max} = \lambda^2$ . Therefore, for a thermal source, the far field determined by the Fraunhofer Approximation is

$$z \gg \pi\lambda, \quad (12)$$

In the far-field, thermal radiation is generally considered spectrally and spatially incoherent. However, coherent thermal emission was observed for the first time in the far-field by Greffet *et al.* in 2002 [7]. Greffet *et al.* showed that by combining a comprehension of electromagnetics, surface waves and modes, and optical properties of materials, they could create a grating structure which showed coherent angular selective emission. Therefore, an electromagnetic approach is needed in order to understand and produce coherent thermal radiation in the far field.

However, McConnell and many others were able to achieve coherent thermal emission in the far-field using designs based on a Fabry-Perot etalon [13, 17, 28, 31]. A Fabry-Perot etalon consists of two plane, parallel, highly reflective surfaces separated by some distance  $d$ . This is typically used in an optical system that includes collimating and focusing lenses, see Figure 5. Consider a single ray from a diffuse, broadband source that is placed in the focal plane of the collimating lens. As the ray passes through the plane, parallel, reflective surfaces, it is multiply reflected to produce multiple transmitted rays

which are collected and focused by the second lens to a point. The summation of all the points produces an interference pattern that creates a set of concentric rings, see Figure 6. The interference pattern is the result of the multiple reflections of light between the two surfaces. Constructive interference occurs if the transmitted beams are in phase, and destructive interference when the beams are out-of-phase. The phase difference ( $\delta$ ) between each transmitted beam pair is given by

$$\delta = \left(\frac{2\pi}{\lambda}\right) 2nd \cos\theta , \quad (13)$$

where  $n$  is the refractive index of the medium between the reflective surfaces,  $d$  is the spacing between the reflective surfaces, and  $\theta$  is the angle which the light travels through the etalon [49]. However, there are multiple wavelengths that can resonate within the cavity for a particular angle ( $\theta$ ) and spacing ( $d$ ) given by

$$\lambda = \frac{2nd \cos\theta}{q} , \quad (14)$$

where  $q = 1, 2, \dots$  represents the mode resonating in the cavity.

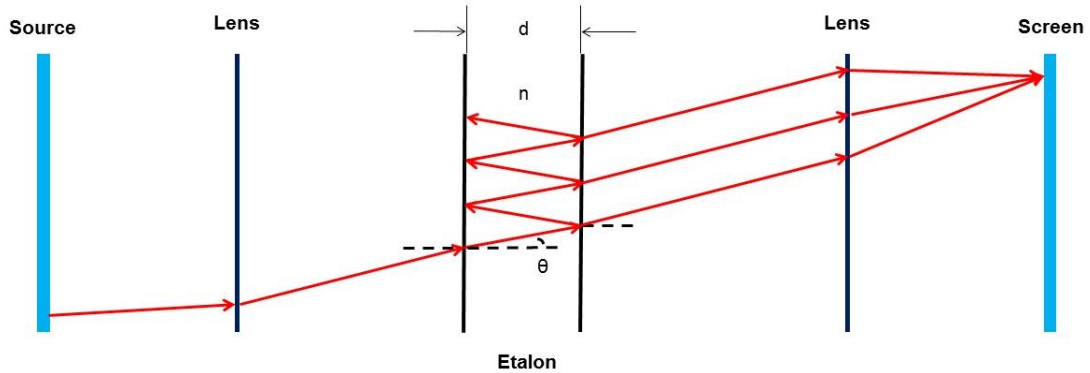


**Figure 5. Illustration of an optical system that includes a Fabry-Perot etalon. The system creates a pattern of concentric bright and dark rings that indicate constructive and destructive interference from a diffuse, broadband source. The lens on the left of the etalon collimates the source and the lens on the right focuses the beam leaving the etalon to a point on the screen.  $d$  is the spacing between the reflectors,  $n$  is the index of the medium in the space, and  $\theta$  is the angle which the light travels through the etalon.**



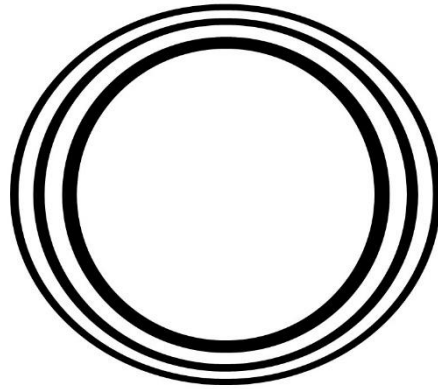


**Figure 6. Concentric ring interference pattern created on the screen due to the multiple reflections from the etalon and focusing lens.**

### **Design of a Thermal Emitter**

When designing a thermal emitter, the application and its use play a vital role. The application of the emitter and the environment in which it is to operate have a direct influence on the wavelength at which the device is designed to absorb and emit thermal radiation. For instance, if a device is to be used outside and a detector/collector is located a distance away from the emitter, then atmospheric absorption will need to be taken into account. The impact the atmosphere has on the signal depends on the path length travelled through the atmosphere and the emitted, or source, wavelength. If the wavelength range of interest is 2-20  $\mu\text{m}$  and the source is at a medium altitude, about 6 kilometers (km), on a clear, mid-summer day with normal visibility, about 23 km, then the atmosphere will absorb a significant portion of the signal if it is in the range of 5-8  $\mu\text{m}$  and 14-20  $\mu\text{m}$ . Figure 7 is a plot the spectral transmittance of the atmosphere for the

conditions described above computed using the Moderate-Resolution Atmospheric Radiance and Transmittance Model (MODTRAN) software package.

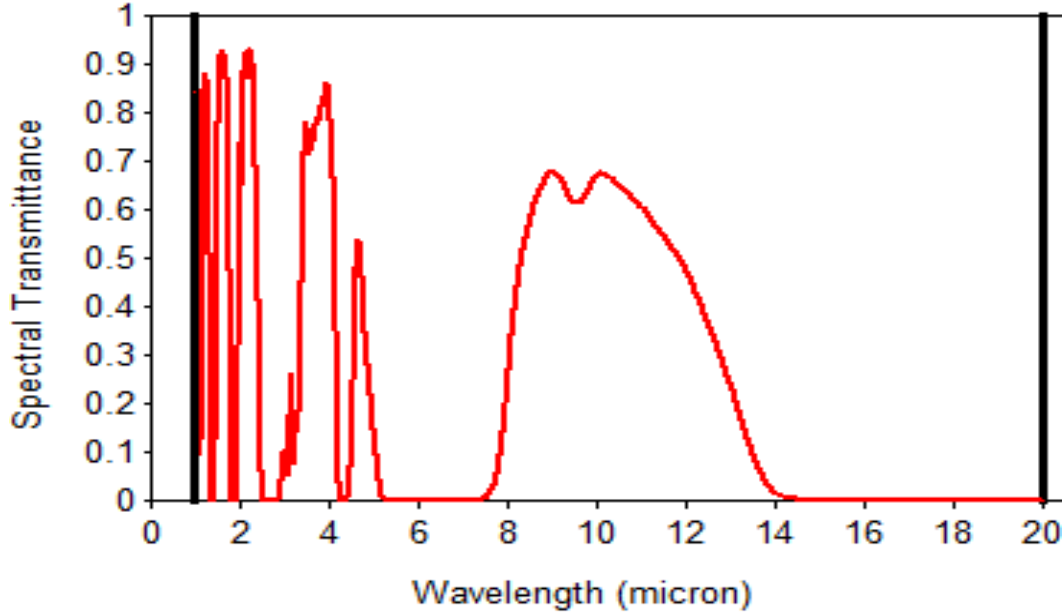


**Figure 7.** Spectral transmittance of the atmosphere when observing an object at medium altitude (about 6km) on a clear, mid-summer day with normal visibility (about 23km) computed using the software package MODTRAN.

Wavelengths of 2-10  $\mu\text{m}$  are the focus for this study. Thermal emitter designs will be proposed which utilize the atmospheric transmission bands between 3-5  $\mu\text{m}$  and 8-14  $\mu\text{m}$  and the absorption bands 5-8  $\mu\text{m}$  and 14-20  $\mu\text{m}$ .

### **Finite Difference Time Domain (FDTD) Analysis**

The physics of the finite difference time domain (FDTD) method is buried in Maxwell's equations,

$$\nabla \times \vec{E} = -\vec{M}_i - \frac{\delta \vec{B}}{\delta t} \quad (15)$$

$$\nabla \times \vec{H} = \vec{J}_i + \vec{J}_c - \frac{\delta \vec{D}}{\delta t} \quad (16)$$

$$\nabla \cdot \vec{D} = q_{ev} \quad (17)$$

$$\nabla \cdot \vec{B} = q_{mv} \quad (18)$$

where  $\vec{E}$  is the electric field (volts/meter),  $\vec{M}_i$  is the impressed magnetic current density (volts/square meter),  $\vec{B}$  is the magnetic flux density (webers/square meter),  $\vec{H}$  is the magnetic field (amperes/meter),  $\vec{J}_i$  is the impressed electric current density (amperes/square meter),  $\vec{J}_c$  is the conduction electric current density (amperes/square meter),  $\vec{D}$  is the electric flux density (coulombs/square meter),  $q_{ev}$  is the electric charge density (coulombs/cubic meter), and  $q_{mv}$  is the magnetic charge density (webers/cubic meter). The EM fields and material geometries are discretely described by Yee mesh cells, see Figure 8. Maxwell's equations can be discretely described in time where the time step is related to the mesh size by the speed of light. This discrete formula is a solution to Maxwell's equations for the limit that the mesh cell size approaches zero. These discretized electric and magnetic fields contain past, present, and future time step components. The fields containing the future time components are solved for in terms of the present and past fields. These equations are known as the update equations,

$$\vec{H}\left(t + \frac{\Delta t}{2}\right) = \vec{H}\left(t - \frac{\Delta t}{2}\right) - \frac{\Delta t}{\mu} \nabla \times \vec{E}(t) \quad (19)$$

$$\vec{E}(t + \Delta t) = \vec{E}(t) - \frac{\Delta t}{\varepsilon} \nabla \times \vec{H}\left(t + \frac{\Delta t}{2}\right) \quad (20)$$

where  $\Delta t$  is a small increment in time. At any point in space, the updated field value is dependent on a previously stored value of that field and the numerical curl of the local distribution of the other field.

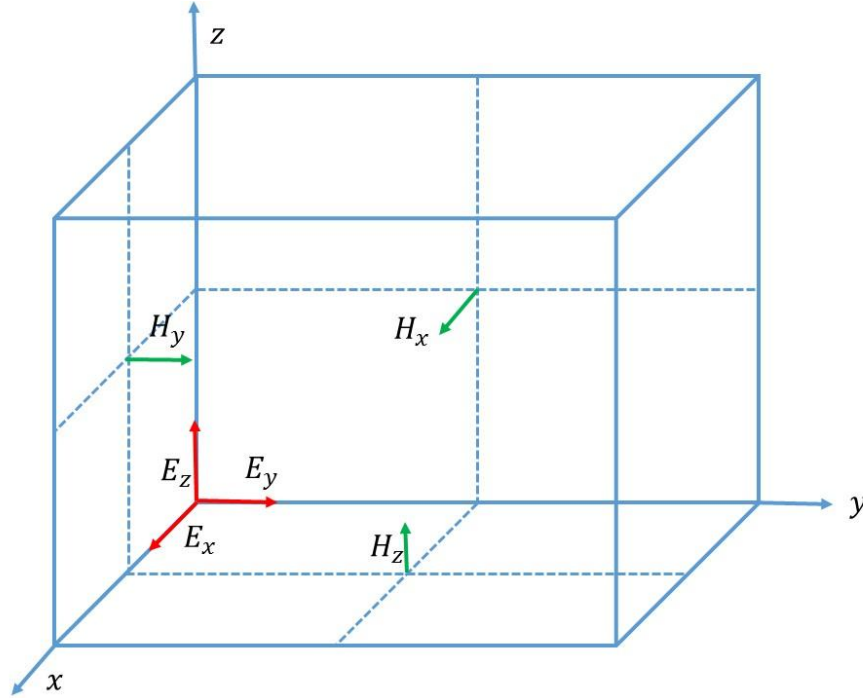


**Figure 8. Yee cell, representing local curl of the fields, used by FDTD numerical method to solve Maxwell's equations.**

Lumerical's FDTD Solutions software will be used to design the nano-structures of this research. This software implements the update equations in order to solve Maxwell's equations. This software is heavily dependent on the user to set up the proper boundary conditions and solver mesh. Lumerical's software has a preloaded database of the optical properties of various materials as reported by Palik's *Handbook of Optical Constants* and the *CRC Materials Science and Engineering Handbook* [50, 51]. If a material that needs to be modeled is not in the database, the user can define its properties

and load it into the simulation either by utilizing a materials script or uploading a predefined text file containing the values.

Since FDTD is a time domain method, the EM fields are calculated as a function of time. The time signal of the source is a pulse defined by

$$s(t) = \sin[\omega_o(t - t_o)] e^{-\frac{(t-t_o)^2}{2(\Delta t)^2}} \quad (21)$$

where  $t_o$  is the initial time,  $\omega_o$  is the initial angular frequency, and  $\Delta t$  is the time step.

The Fourier transform of  $s(t)$  is

$$s(\omega) = \int e^{i\omega t} s(t) dt \quad (22)$$

where  $\omega$  is angular frequency. The ideal scenario would be for  $s(t)$  to be a Dirac delta function. For this case, the Fourier transform would produce the system's response for all frequencies. However, when utilizing Lumerical's FDTD Solutions software, it is more efficient and numerically accurate to excite the system with a short pulse such that  $|s(\omega)|^2$  has a reasonably large value over all frequencies of interest [52].

Lumerical's FDTD Solutions software comes with several boundary condition (BC) definitions. The choice of which BCs to use depends on what the user is attempting to simulate. The computations done in this study used the Perfectly Matched Layer (PML), Bloch, and Periodic BCs. The PML acts as a perfect absorber, allowing the fields to decay in the defined direction or axis. This is useful in confining the system's response to the physical structure being modeled. The Bloch and Periodic BCs are used when dealing with periodic structures. As long as there exists a phase shift between the periodic unit cells of the structure, then only a single unit cell needs to be enclosed in the boundaries. The Periodic BC applies when using a source at normal incidence, and the

Bloch BC applies for the case of off-normal source incidence. The reason for this difference is because Lumerical has built into the Bloch BC the ability to maintain the phase information of the propagation vector while the Periodic BC does not.

There are many radiation sources available in FDTD Solutions. The one used for this study was a linearly polarized, plane wave source of unit amplitude. This source is only used with periodic BCs (Bloch and Periodic) placed at normal or less than 90° from the propagation vector and PML BCs in the forward/reverse direction of propagation. The plane wave is assumed to be infinite in extent, 1-D (width) or 2-D (area), and propagating into an absorbing boundary. Therefore, the source is to be set up in the model so that it extends outside the periodic boundaries. By default, this source is linearly polarized. However, different polarizations can be simulated by using the superposition of multiple sources.

There exists a limitation of the FDTD method concerning off-normal broadband source simulation with Bloch BCs. Broadband sources inject fields that require a constant in-plane wave vector at all wavelengths, as described by

$$k_{in-plane} = \frac{2\pi}{\lambda_c} \sin(\theta_d) \quad (23)$$

where  $\lambda_c$  is the center wavelength and  $\theta_d$  is the incident elevation angle defined by the user. However, in the FDTD method, the broadband source angle  $\theta_i$  will vary with respect to the wavelength for off-normal incidence, but the in plane propagation vector value must be constant for all wavelengths. Therefore,

$$\sin[\theta_i(\lambda)] = \frac{k_{in-plane}}{|k(\lambda)|}. \quad (24)$$

Using the definition of  $k_{in-plane}$  from Equation (23) and  $k(\lambda) = 2\pi/\lambda$ , then

$$\theta_i(\lambda) = \sin^{-1} \left( \frac{\sin(\theta_d) \lambda}{\lambda_c} \right) \quad (25)$$

If a system response that is dependent on  $\theta_i$  and  $\lambda$  (*e.g.* dispersion relation) is desired, then this limitation presents a challenge. Lumerical's software presents two options for overcoming this difficulty. The first solution is to create a two dimensional sweep where a simulation is run for each  $\theta_i - \lambda$  combination. This technique is very easy to implement since the creation of sweeps is very straightforward. There are also many examples and helpful information about sweeps on Lumerical's website [52]. This option also produces good results at the expense of being very time consuming. For example, a simulation for a truncated resonator design over the wavelength range of 2-20  $\mu m$  for seven angles between 15° and 75° will take approximately one week to run on one of AFIT's LoreNet computers.

The second option is to perform a broadband sweep at  $\theta_i$  and interpolate the data points into a common source angle with a post-processing script. This technique is easy to implement because the data points for each  $\theta_i$ - $\lambda$  combination are stored and simply need to be aligned and interpolated into a common step size. One drawback to this technique is the constraint placed on  $\theta_d$ . The range of  $\theta_d$  is a function of the bandwidth of interest as given by

$$\max(\theta_d) = \sin^{-1} \left( \frac{\lambda_c}{\lambda_{max}} \right). \quad (26)$$

Therefore, a full angle range of  $\theta_d$ , from 0° to 90°, cannot be evaluated using this method.

In FDTD Solutions, the system's response is measured by monitors. There are multiple monitors available to the user, but only the frequency domain power monitor was used for this study. This monitor collects the time signal at a specified distance from the structure of interest and can be used in 2-D (as a line) and 3-D (as a plane) simulations. This monitor performs the Fourier transform on the collected signal and returns the complex field values for the specified location. An additional feature for monitors is the analysis group. Analysis groups are collections of monitors that allow the user to write a script and define functions in order to extract desired simulation characteristics.

Lumerical's FDTD Solutions is a powerful 3-D Maxwell equation solver, capable of analyzing interactions of ultraviolet (UV), visible, and IR radiation with complicated structures with wavelength-scale features [52]. The software's interface is user friendly, easy to use, and there is extensive documentation/information available on Lumerical's website.

## **Reflectance**

The reflectance of a surface will largely be determined by the characteristics of that unique surface, such as roughness, particulates, porosity, defects, and surface-bulk interactions. How strongly these characteristics manifest within the surface is dependent on the type of deposition used to fabricate the material and the deposition process. Surfaces such photonic nano-structures can have unique optical properties seldom found in natural materials. To gain physical insight into the phenomena related to optical



observables, spectral directional hemispherical reflectance of the surfaces will be measured. The directional hemispherical reflectance (DHR) of a surface is defined as the ratio of the total energy reflected into the subtending hemisphere to the energy incident on the surface from a specific direction  $(\theta, \phi)$  as shown in Figure 9.

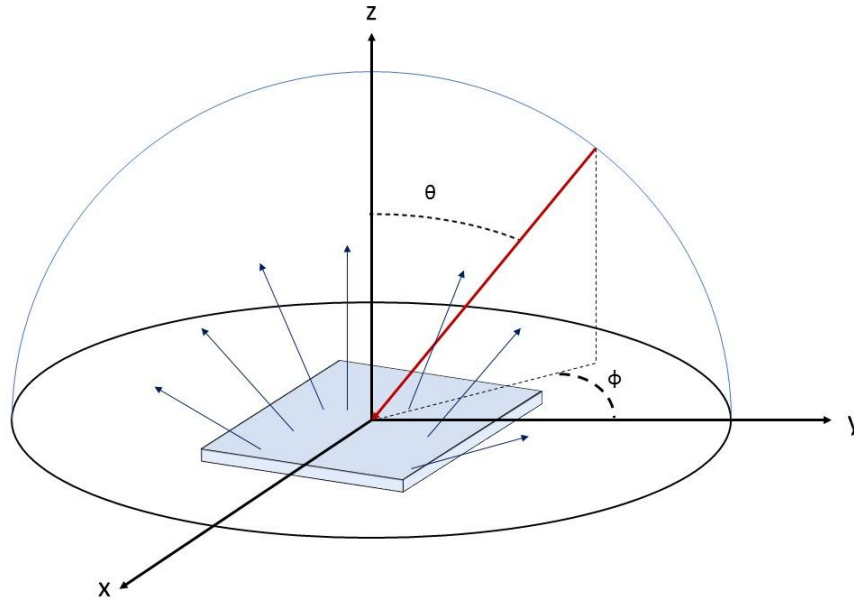


**Figure 9. Illustration of incident radiation (red ray) on a surface from a specific direction defined by the elevation angle  $\theta$  and azimuthal angle  $\phi$  that scatters into a hemisphere (blue rays).**

The measured total reflectance of a surface from a specific incident direction may be used to compute the total emittance from a specific incident direction which is important in describing radiative heat transfer using Kirchhoff's law.

### **Spectroscopic Ellipsometry**

The chosen method used to deposit materials onto a substrate has a significant impact on the optical properties of the material. Since all evaporated films are amorphous

to some extent, the resulting microstructure of the material will affect the way light interacts with that material. Ellipsometry is an optical measurement technique that characterizes light reflection, or transmission, from samples [53]. This method measures the change in the polarization of incident light as it is reflected from or transmitted through the sample in order to determine its optical and physical properties.

Light is a solution to Maxwell's equations. Due to the principle of superposition, there are many solutions which can exist in the same space [54]. Any combination of fields sharing the same direction of propagation can be expressed as the sum of two independent fields whose amplitudes are orthogonal to one another. This simplified field can be thought of as a field which exhibits elliptical polarization. Therefore, when considering an electric field which is incident on a surface, the part of the field which is parallel to the plane of incidence is referred to as p-polarization (p-pol or p), and the part which is perpendicular to the plane is s-polarization (s-pol or s). When polarized light is incident on a material, the material changes the polarization of the light by affecting the direction of propagation, amplitudes of the orthogonal components, and phase of the fields.

Two distinct values,  $\psi$  and  $\Delta$ , are measured in ellipsometry. These represent the amplitude ratio  $\psi$  and phase difference  $\Delta$  between the incident p-pol and s-pol fields and reflected or transmitted p-pol and s-pol fields, respectively, and are expressed as

$$\psi \equiv \tan\left(\frac{E_s}{E_p}\right) \quad (27)$$

$$\Delta \equiv \phi_p - \phi_s, \quad (28)$$

where  $E_p$  and  $E_s$  are the amplitudes of the p- and s-pol fields and  $\phi_p$  and  $\phi_s$  are the phases of the p- and s-pol fields. These values,  $\psi$  and  $\Delta$ , are used to define a quantity known as the complex reflection coefficient,

$$\rho \equiv \tan\psi \exp(i\Delta) \equiv \frac{r_p}{r_s} \equiv \left( \frac{E_{rp}}{E_{ip}} \right) / \left( \frac{E_{rs}}{E_{is}} \right), \quad (29)$$

where  $r_p$  and  $r_s$  are the amplitude reflection coefficients for the p- and s-polarizations and are defined as the ratios of the reflected electric fields ( $E_{rp}$ ,  $E_{rs}$ ) to the incident electric fields ( $E_{ip}$ ,  $E_{is}$ ). The complex reflection coefficient  $\rho$  is a ratio used to express the portion of incident light which is reflected by the sample.

The Fresnel equations describe the reflection and transmission of electromagnetic waves at a boundary between media of differing refractive indices. Therefore, when there exists light reflection off of an air/sample interface and the sample is a layer deposited on a substrate assumed to be infinitely thick, the following equation can be found

$$\rho = \frac{r_{012,p}}{r_{012,s}} = \left( \frac{r_{01,p} + r_{12,p} \exp(-i2\beta)}{1 + r_{01,p} r_{12,p} \exp(-i2\beta)} \right) / \left( \frac{r_{01,s} + r_{12,s} \exp(-i2\beta)}{1 + r_{01,s} r_{12,s} \exp(-i2\beta)} \right), \quad (30)$$

where  $r_{012,p}$  is the total reflectance for the p-pol wave,  $r_{012,s}$  is the total reflectance for the s-pol wave,  $r_{01,p}$  and  $r_{01,s}$  are the reflectances from the air(0)/layer(1) interface for the p- and s-pol waves, respectively,  $r_{12,p}$  and  $r_{12,s}$  are the reflectances from the layer(1)/substrate(2) interface for the p- and s-pol waves, respectively, and  $\beta$  is the phase variation between the waves that are reflected at the air/layer interface and the layer/substrate interface. More detailed information on the derivation and  $\beta$  can be found in Fujiwara *et al.* [54]. Utilizing the Fresnel equations, the reflectance at each of the

boundaries ( $r_{01}$ ,  $r_{12}$ ) can be related to the complex refractive indices for the air ( $N_0$ ), material layer ( $N_1$ ), and substrate ( $N_2$ ) by the following generalized formula

$$r_{jk,p} = \frac{N_k \cos \theta_j - N_j \cos \theta_k}{N_k \cos \theta_j + N_j \cos \theta_k} \quad (31)$$

$$r_{jk,s} = \frac{N_j \cos \theta_j - N_k \cos \theta_k}{N_j \cos \theta_j + N_k \cos \theta_k}, \quad (32)$$

where the subscripts  $j$  and  $k$  represent the top (lower numerical value) and bottom (higher numerical value) materials at an interface, respectively,  $\theta_j$  is the incident angle on the interface, and  $\theta_k$  is the transmitted/refracted angle. Therefore, by measuring  $\psi$  and  $\Delta$ , it is possible to determine the optical properties of a material, which can be summarized as

$$N \equiv n + ik, \quad (33)$$

where  $N$  is the complex index of refraction,  $n$  is the refractive index, and  $k$  is the extinction coefficient.

When the complex refractive indices are functions of wavelength  $N(\lambda)$ , the optical constants can be found using spectroscopic ellipsometry. Spectroscopic ellipsometry (SE) is performed by changing the wavelength of the incident light. In general, SE measurements are carried out for the ultraviolet, visible, and infrared (IR) regions. SE presents many distinct advantages as a measuring technique. Specifically, it has a high thickness sensitivity ( $\sim 1$  nm), nondestructive, and only takes a few seconds. Due to these advantages, SE is of particular importance for real-time monitoring of thin-film growth, etching, and thermal oxidization. However, there are some restrictions on the SE measurement. Specifically, the surface roughness of the sample has to be small,

and the measurement must be performed at oblique incidence. Generally, when the surface roughness exceeds ~30% of a measurement wavelength, errors increase due to the loss of collected intensity from surface scatter which is needed to determine the polarization state.

In ellipsometry, an incidence angle is chosen so that sensitivity for the measurement is maximized. When dealing with isotropic materials, the normal angle is never chosen because it is impossible to distinguish between the s- and p-pols. Typically, the angle of incidence chosen is close to the Brewster angle in order to ensure a maximal difference in  $r_p$  and  $r_s$  [55].

The main drawback to ellipsometry is its indirect method of characterization for a layered structure. The data acquired through ellipsometry is for the effective medium, or the entire structure. In order to characterize a layer of the structure, a modeling technique which accounts for the reflections and transmissions at each boundary must be implemented. However, using an optical model tends to become complicated, especially when dealing with thin layers (~10 nm).

The ellipsometer is sensitive to several different material parameters, such as strain, composition, size of the particle, thickness, and optical properties [56]. This is useful as it is able to sense changes in these parameters, and through modeling, extract the optical properties and thicknesses of the materials. However, in order to accurately model a sample with these properties, a greater understanding of the optical properties of materials and their dependence on material structure is required, especially when dealing with thin layers. Lastly, as layers become thinner, there is a coupling between the extracted thickness and refractive index based on the change in phase due to the path

length. For more information and a deeper discussion on determining the optical properties of materials by ellipsometry, see [46, 57].

## **Summary**

The goal of the background theory presented was to provide a basis for undertaking the design, fabrication, and characterization of infrared nano-structures. Relevant publications were cited and emphasized for further study and in-depth background into the pertaining subject matter. With the understanding of this theory, the approach and process chosen for further investigation and observation of coherent thermal emission will be explained next.

### **III. Methodology**

#### **Chapter Overview**

The goal of this study is to design, fabricate, and measure the performance of a few different nanostructures that act as selective emitters, both spectrally and directionally, at infrared wavelengths of interest and are shown to be thermally stable. SWIR to LWIR wavelengths of 2-20  $\mu m$  were chosen as the design wavelengths of interest given their relevance in practical thermal radiation emission and detection problems. The thermal emitter surfaces are also expected to perform in high-temperature environments, up to 1000 Kelvin (K) [32], so the constituent materials were required to be thermally stable when heated. This made high melting points and thermally matched expansion coefficients between constituent materials necessary in order to prevent destruction and delamination of the samples.

Four thermal emitter designs are proposed in this work. A few iterations will be made on the truncated resonator design in which the materials and dimensions of the resonator are changed in order to achieve sharp emission at the desired wavelengths. The methodology behind each of these thermal emitter designs is described below in detail with associated fabrication and characterization techniques.

#### **Truncated Multilayer Resonator**

The first thermal emitter design is a truncated resonator design based on a multilayer resonator. This planar structure was chosen for its relative ease in fabrication

while still achieving coherent thermal radiative properties through wave interference effects. The resonant cavity is formed by sandwiching a transparent medium between two reflective media. One of the reflective media is optically thick, while the other is optically thin (thickness below intrinsic penetration depth). Figure 10 shows an illustration of a truncated multilayer resonator.

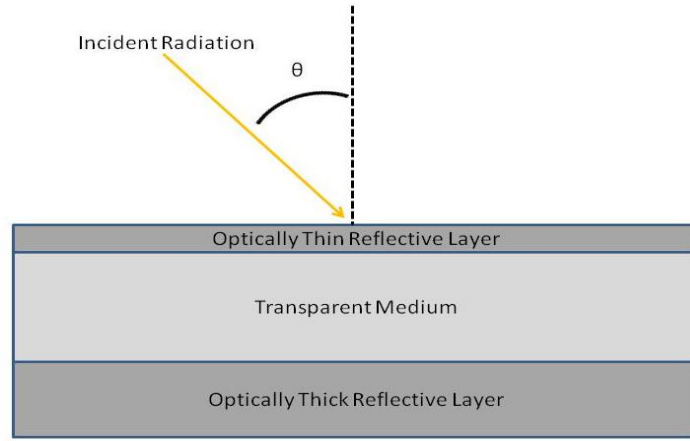


**Figure 10. Illustration of truncated multilayer resonator, which is defined as a structure which contains a transparent layer between an optically thin reflective layer and an optically thick reflective layer. The thin reflective layer is exposed to the incident radiation.**

### **Constituent Material Properties.**

#### *Complex Refractive Index.*

As previously mentioned, these structures are expected to perform in environments as hot as 1000 K [32]. Therefore, metals such as tungsten (W) and tantalum (Ta) which have high melting points, 3695 K and 3290 K, respectively, and low thermal expansion coefficients,  $4.5 \frac{\mu m}{m K}$  and  $6.3 \frac{\mu m}{m K}$ , respectively, are very attractive. W and Ta also have lower absorption coefficients than some of the other popular reflective materials, such as silver (Ag) and gold (Au), see Figure 11. This becomes important



when dealing with thin metal films because a smaller absorption coefficient allows for a thicker layer to be deposited without losing as much incident radiation through the thin film, or a smaller absorption coefficient means the point at which the metal becomes optically opaque is at a thicker depth. This depth is also referred to as the skin depth and is discussed in more detail later. Therefore, the properties (*e.g.*, optical constants and melting point) of a thicker metal layer will not change as much.

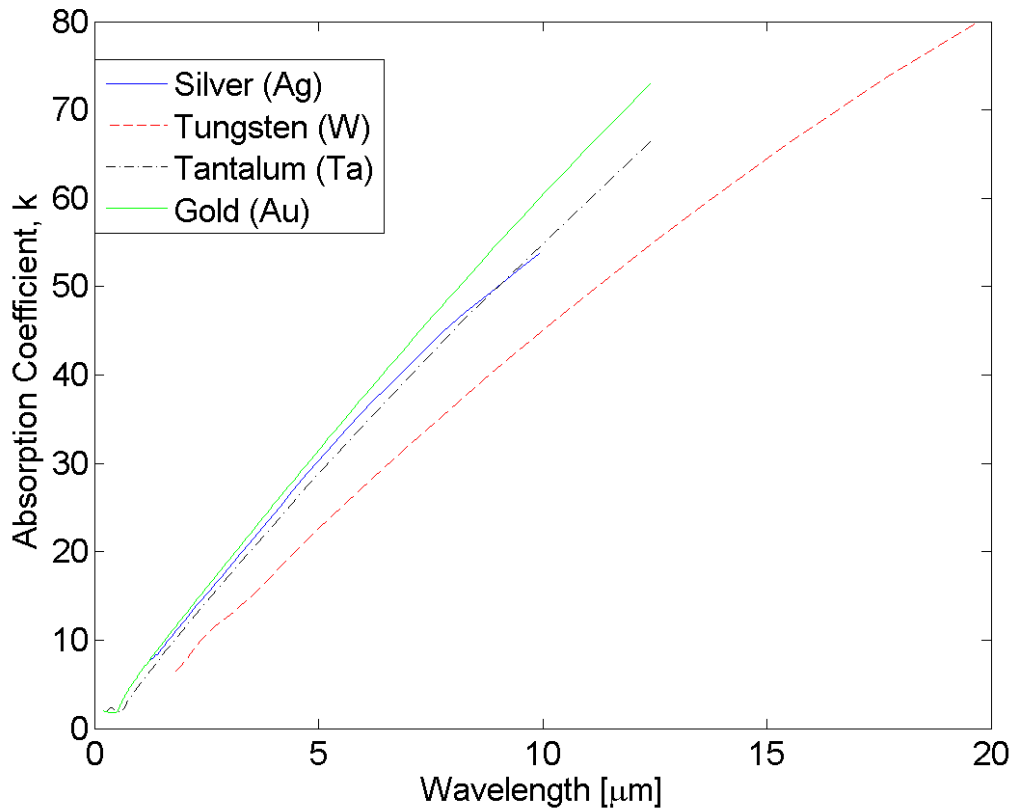


**Figure 11.** Spectral absorption coefficients for silver (Ag) [blue], Tungsten [red dash] (W), Tantalum (Ta) [black dash-dot], and Gold (Au) [green]. Properties from [46, 51, 58].

Often, different properties (*e.g.*, melting point, complex refractive index, and thermal conductivity) are reported from different sources for the same material [59-66]. Little temperature-dependent optical constant data was found for W [67]. Unfortunately,

no temperature-dependent data was found for Ta. Ag, W, and Ta have different advantages in being chosen for the reflective layer of the resonator. Ag exhibits the highest thermal conductivity of all metals. See Figure 12 for a plot of the reflectivity of a few metals as a function of wavelength. High reflectivity is desired for sharp spectral responses of the cavity. However, the reflectivity of Ag, W, and other metals in the IR wavelength range is a decreasing function of temperature [14, 68, 69]. The reduction of reflectivity at longer wavelengths is much lower than that at shorter wavelengths. For example, Ujihara *et al.* showed that aluminum (Al) experiences a 2% reduction in reflectivity at  $10.6\ \mu\text{m}$  for a temperature of 925 K, whereas at  $0.69\ \mu\text{m}$  for the same temperature, Al experiences a 30% reduction [69]. The reduction in reflectivity a metal experiences is dependent on the type of metal and the temperature of the metal [69]. Ujihara also tested the reduction for Ag, Au, sodium (Na), copper (Cu), potassium (K), and Al over the temperature range of 300 K to 1300 K at  $0.69\ \mu\text{m}$  and  $10.6\ \mu\text{m}$ . He found that for metals like Au and Ag, reduction in reflectivity as a function of increasing temperature is almost negligible, especially over longer IR wavelengths. This makes Ag a very appealing choice as a reflective boundary.

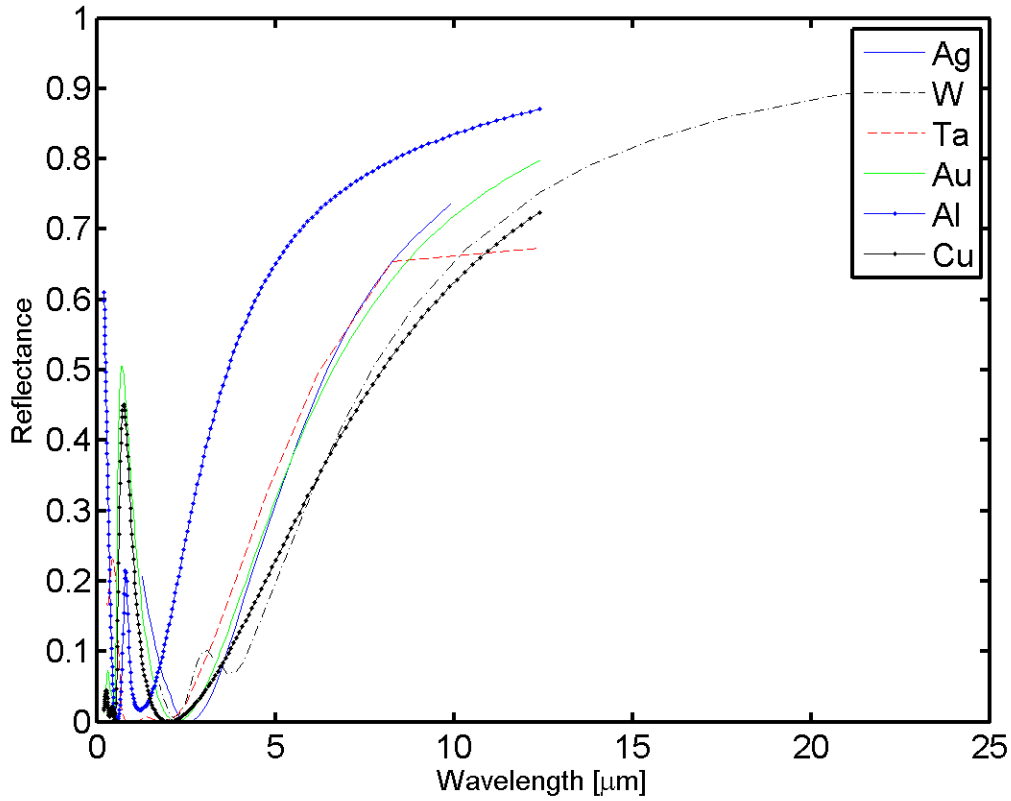


**Figure 12. Spectral reflectivity of Ag (blue), W (black dash-dot), Ta (red dash), Au (green), Al (blue dots), and Cu (black dots) as computed by the Fresnel equations for normal incidence.**

However, Ag has a lower melting point than W at 1235 K, a higher thermal expansion coefficient,  $18.9 \frac{\mu m}{m K}$ , and larger absorption coefficient values. Therefore, W and Ta are expected to perform better, in maintaining the optical and emissive properties of their solid states, at the higher temperatures than Ag. This is anticipated because it has been shown that the melting point of thin metal films is lower than the values reported for the bulk material and continues to decrease as the material becomes thinner [30, 70-71]. In fact, in a study done by a former AFIT student, McConnell, on a truncated resonator composed of Ag and Ge, it was observed that the top, thin Ag metal layer of

approximately 6 nm partially melted and balled up, causing a breakdown of the structure and its emissive properties [31]. Therefore, W and Ta will be the metals under consideration for the reflective layers of the resonator due to their high thermal properties.

A model was used to approximate the optical constants of W at high temperatures. This was accomplished using a dielectric function by the free-electron/Drude model

$$\varepsilon(\omega) = 1 - \left( \frac{\omega_p^2}{\omega(\omega - i\omega_c)} \right) \quad (34)$$

where  $\omega$  is the frequency,  $\omega_p$  is the plasma frequency, and  $\omega_c$  is the electron collision frequency [58, 69]. As temperature increases, so does the electron collision frequency  $\omega_c$  [69]. This results in increased absorption of the metal at high temperatures which affects cavity losses. Drude's formula for the dielectric constant  $\varepsilon$  can take different forms depending on the information available about the material and assumptions made (*e.g.*, approximating sum). Equation (35) is a version of Drude's model adapted to accommodate for the multiple resonances inherent in a material. It was taken from Eq (39) in [72:398] and the presented form differs only in notation.

$$\varepsilon = 1 + \sum_m \frac{\varepsilon_{0m}\lambda^2}{\lambda^2 - \lambda_{sm}^2 + i\delta_m\lambda_{sm}\lambda} - \frac{\lambda^2}{2\pi c\varepsilon_0} \sum_n \frac{\sigma_n}{\lambda_{rn} - i\lambda}, \quad (35)$$

where  $\lambda$  is the wavelength in vacuum,  $c$  is the speed of light,  $\varepsilon_0$  is the permittivity of vacuum (in mks units), and the other parameters are arbitrary coefficients which are adjusted independently to characterize any given metal. Roberts conducted experiments at a range of temperatures (294K, 1100 K, 1600 K) in order to determine these coefficients for W over a wavelength range of 0.365 to 2.65  $\mu m$  [67]. Table 1 contains

some of these coefficient values for the various temperatures at which Roberts made measurements.

**Table 1. Results of analysis of temperature dependent optical data for tungsten, performed and reported by [67]. ( ) indicates tentative estimates. Conductivities ( $\sigma_1$ , ect.) are in units of  $10^6 \text{ ohm}^{-1}\text{m}^{-1}$ . The dc conductivity is  $\sigma_0$ . Wavelengths ( $\lambda_{r1}$ ,  $\lambda_{s1}$ , ect.) are in  $\mu\text{m}$ .**

Temp	298 K	1100 K	1600 K
$\sigma_1$	17.50	3.5	2.14
$\sigma_2$	(0.21)	0.16	0.19
$\lambda_{r1}$	45.5	9.3	6.0
$\lambda_{r2}$	(3.7)	< 0.36	< 0.36
$K_{01}$	12.0	10.9	10.9
$K_{02}$	14.4	13.4	13.4
$K_{03}$	12.9	12.0	12.0
$\lambda_{s1}$	1.26	1.40	1.40
$\lambda_{s2}$	0.60	0.57	0.57
$\lambda_{s3}$	0.30	0.25	0.25
$\delta_1$	0.6	1.0	1.0
$\delta_2$	0.8	1.2	1.2
$\delta_3$	0.6	1.0	1.0
$\sigma_0$	17.7	3.67	2.34

Assuming these coefficients do not vary significantly over the SWIR to LWIR range of 2-20  $\mu\text{m}$ , this data can be used to compute temperature dependent dielectric constant values for W. Figure 13 shows the real and imaginary parts of the complex dielectric function of W at 294 K, 1100 K, and 1600 K as calculated using the measured parameters in the Drude model, Eq (25), from 2-20  $\mu\text{m}$ .

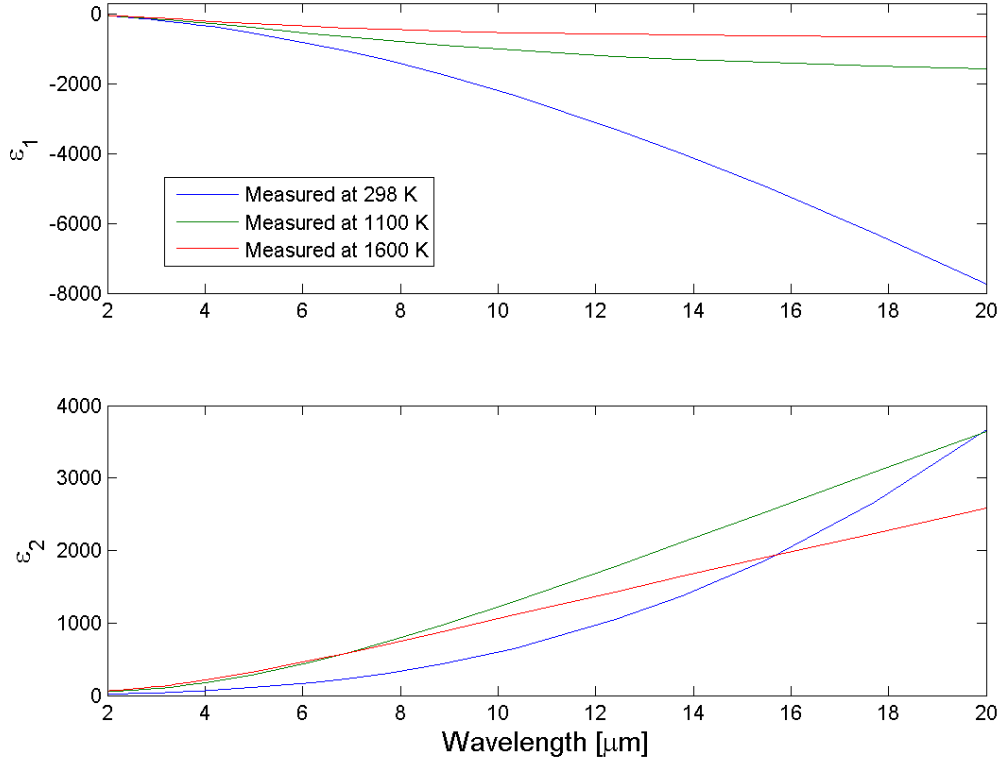


**Figure 13.** Real ( $\epsilon_1$ ) and imaginary ( $\epsilon_2$ ) parts of the complex dielectric function of tungsten at 294 K (room temperature) , 1100 K, 1600 K as calculated from the Drude model, Eq (25), with the measured optical parameters in Table 1 from [67].

The complex dielectric constant  $\epsilon$  of a material, which is a function of temperature, is equal to the square of the complex refractive index,

$$\epsilon(T) = [n(T) \pm ik(T)]^2, \quad (36)$$

where  $n$  is the real part of the refractive index and  $k$  is the imaginary part, also known as the extinction coefficient. The choice of using  $n - ik$  or  $n + ik$  depends on the sign of the assumed plane-wave solution in Maxwell's equations. For this study, a forward propagating wave is chosen to have the form  $e^{-j\vec{k}\cdot\vec{r}}$ , where  $\vec{k}$  is the propagation vector (direction of propagation) and  $\vec{r}$  is the position vector. Thus,  $n - ik$  is the convention

used here. Therefore, the relationship between the real ( $\varepsilon_1$ ) and imaginary ( $\varepsilon_2$ ) parts of the dielectric constant to the refractive index for this study is

$$\begin{aligned}\varepsilon(T) &= \varepsilon_1(T) - i\varepsilon_2(T) \\ &= [n(T) - ik(T)]^2.\end{aligned}\tag{37}$$

From the free electron/Drude model given above, the real and imaginary parts of the dielectric constant were solved for over a range of IR frequencies at a given temperature  $T$ . Taking into account the frequency-dependence of the complex dielectric constant gives rise to the following expressions for the real and imaginary parts of the complex refractive index as a function of frequency  $\omega$ ,

$$n(\omega, T) = \sqrt{\frac{1}{2}\{\varepsilon_1(\omega, T) + [\varepsilon_1^2(\omega, T) + \varepsilon_2^2(\omega, T)]^{\frac{1}{2}}\}}\tag{38}$$

and

$$k(\omega, T) = \sqrt{\frac{1}{2}\{[\varepsilon_1^2(\omega, T) + \varepsilon_2^2(\omega, T)]^{\frac{1}{2}} - \varepsilon_1(\omega, T)\}}\tag{39}$$

Temperature-dependent optical constants for Ag were calculated at various high temperatures. Therefore, using Equations (37), (38) and (39), values for temperature-dependent optical constants of W were calculated based on the values found for the complex dielectric constant. Figure 14 compares the complex refractive index of bulk W at room temperature to several high-temperature values over the IR wavelength range of 2-20  $\mu m$ .

The difference between the refractive index values at room temperature which can be observed from Roberts' [67] measurements and what Palik reports increases at longer wavelengths. In fact, the average root-mean-square error (RMSE) value for  $n$  and  $k$

between the two sets of values for the range of 2-20  $\mu m$  is 4.73 and 3.7, respectively. Whereas, the average RMSE for the range of 2-8  $\mu m$  is 0.54 and 0.82, respectively. Unfortunately, no existing form derived from Drude's model has been found to fit the optical characteristics reported for Ta.

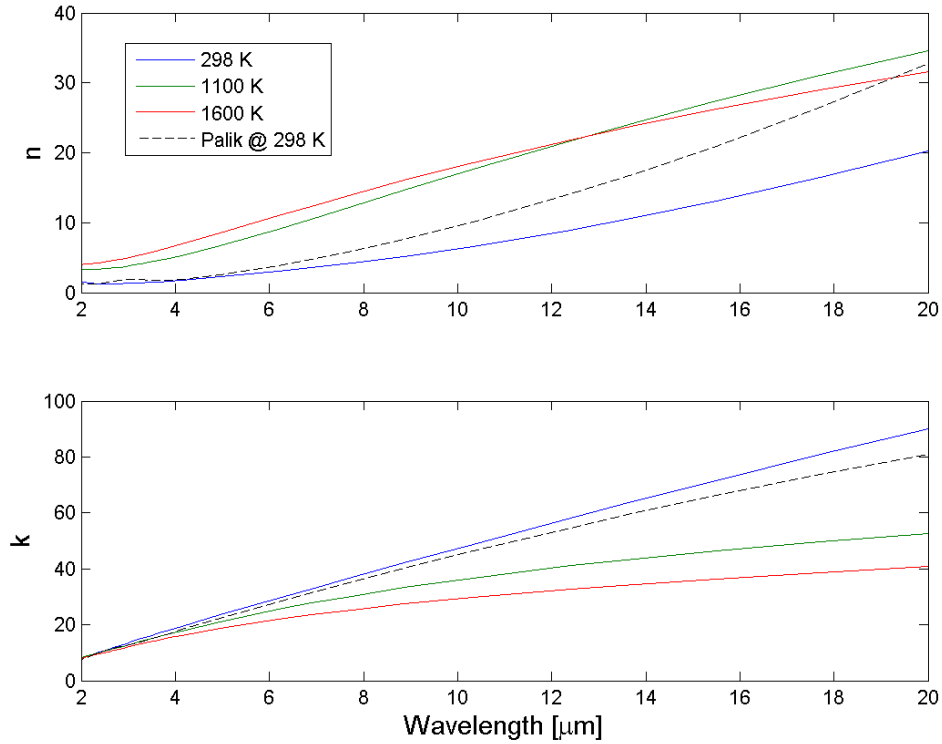


**Figure 14. Complex refractive index for tungsten where  $n$  is the real part and  $k$  is the imaginary. Values were obtained using the Drude model, Eq (25), with the measured optical parameters in Table 1 from [67] at 294 K, 1100 K, and 1600 K and plotted with measured values reported in Palik [38].**

Two materials were chosen to be compared for the dielectric/transparent layer, germanium (Ge) and hafnium oxide ( $HfO_2$ ). They were chosen for their range of transparency in the SWIR to LWIR, appealing material properties, and different refractive indices.  $HfO_2$  was chosen for its high thermal stability and a transmission range of 0.25 to 9  $\mu m$ . Its primary application is in ultraviolet (UV) to IR multilayer materials



[73]. Due to the challenges of working with HfO<sub>2</sub>, which were that not a lot of literature was found with optical properties at room and none for elevated temperatures [63-64], a more well-known material, Ge, was also chosen. Ge is a high index semiconductor that is used in many IR applications, from substrates to optical filters and lenses to attenuated total reflection prisms for spectroscopy, and has a transmission range of 1.8 to 23  $\mu\text{m}$  [74]. Representative values of refractive index, melting point, thermal expansion, and transmission range for Ge and HfO<sub>2</sub> are given in Table 2.

**Table 2. Material and Thermal Properties of Crystalline Germanium (Ge) and Hafnium Oxide (HfO<sub>2</sub>) from [61-64]**

	Crystalline Ge	Crystalline HfO <sub>2</sub>
Thermal Expansion Coefficient (per K)	$6.1 \times 10^{-6}$	$6 \times 10^{-6}$
Melting Point (K)	1210	3085
Refractive Index	4	2
Transmission Range ( $\mu\text{m}$ )	2 – 14	0.25 - 9

Since these thermal emitters will be tested at temperatures higher than room temperature, temperature-dependent optical constants are desired for Ge and HfO<sub>2</sub>. Barnes and Piltch [75] calculated temperature-dependent coefficients for Ge from accepted empirical optical constants for the Sellmeier equation

$$n^2(\lambda) = A + \frac{B\lambda^2}{\lambda^2 - C} + \frac{D\lambda^2}{\lambda^2 - E} \quad (40)$$

where  $n$  is the real part of the refractive index, and  $A, B, C, D$ , and  $E$  are Sellmeier coefficients. Using temperature dependent values of refractive index  $n$ , Barnes and Piltch calculated the following values for the Sellmeier coefficients of Ge:

$$\begin{aligned}
A(T) &= -6.040 \times 10^{-3}T + 11.05128 \\
B(T) &= 9.295 \times 10^{-3}T + 4.00536 \\
C(T) &= -5.392 \times 10^{-4}T + 0.599034 \\
D(T) &= 4.151 \times 10^{-4}T + 0.09145 \\
E(T) &= 1.51408T + 3426.5
\end{aligned} \tag{41}$$

Potter evaluated the Sellmeier equation at room temperature over a range of IR wavelengths [76], and this data can be found in Palik's *Handbook of Optical Constants for Solids* [57].

Figure 15 compares the calculated refractive index for Ge using the Sellmeier equation at 294 K (room temperature), 500 K, and 1000 K along with the measured refractive index values published by Li for intrinsic Ge at 500 K [77]. The measured and modeled refractive index values for Ge at 500 K are observed to be in close agreement with a RMSE of 0.025. Unfortunately, no temperature-dependent data, theoretical or experimental, was found for the optical properties of HfO<sub>2</sub>.

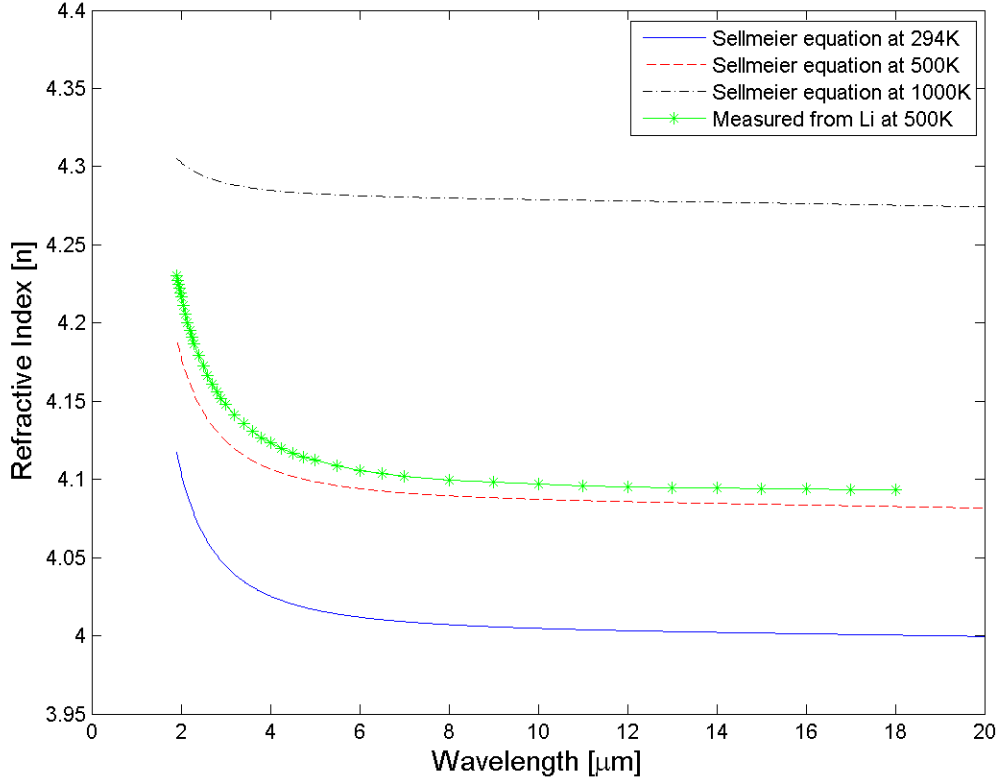


**Figure 15. Index of refraction for Germanium using temperature dependent Sellmeier equation compared to measured values taken at 500K as reported by Li [77].**

### *Skin Depth.*

The bottom metal layer of the resonator must be opaque in order to produce negligible transmission of incident radiation through the cavity. The depth at which a material is considered optically thick, or skin depth, is the depth at which there exists less than  $1/e$  transmission of incident radiation through the material,

$$\tau(\lambda, x) = e^{-\frac{4\pi k(\lambda)}{\lambda}x} = 1/e \quad (42)$$

where  $\tau$  is the transmission,  $\lambda$  is the wavelength,  $k$  is the extinction coefficient as a function of wavelength, and  $x$  is the skin depth. Therefore, skin depth as a function of wavelength can be expressed by

$$x(\lambda) = \frac{\lambda}{4\pi k(\lambda)}, \quad (43)$$

which means that the point at which a material is optically thick is dependent on the type of material and the wavelength range of interest. Figure 16 is a graphical representation of how the skin depth of Ag, W, and Ta changes over the IR wavelength range for which Palik [38] reports values for the extinction coefficients.

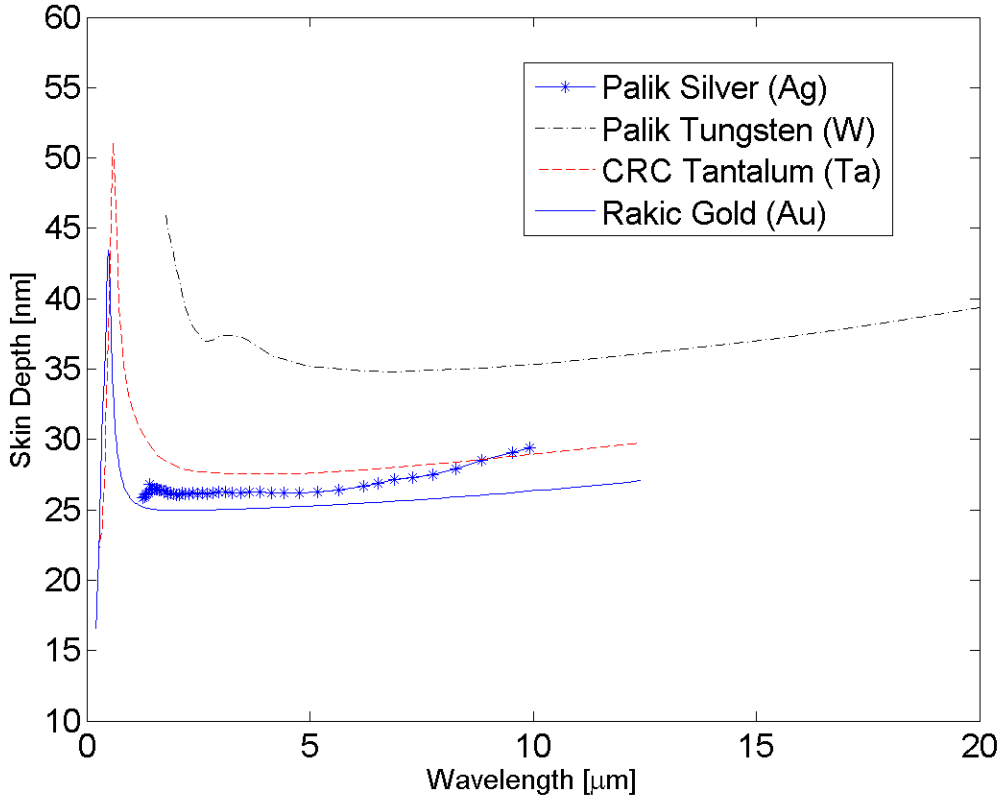


**Figure 16. Graphical illustration of the wavelength dependence of the skin depth for silver, tungsten, tantalum, and gold. The optical properties ( $n$ ,  $k$ ) used for these metals are taken from Palik [46], CRC [51], and Rakic [58].**

It is important to note that all the measurements which Palik reports were taken at room temperature. In general, the skin depth of a metal increases as temperature increases. This is numerically observed to be most prevalent at longer wavelengths [69].

For example at  $10.6\ \mu\text{m}$ , Ujihara experimentally determined that the skin depth of Ag rises from about 30 nm near room temperature (300 K) to 50 nm near its melting point (1230 K) [69]. When a material is deposited, the atomic structure of the material is amorphous which allows electromagnetic waves to penetrate deeper into the metal than would be expected for a bulk, crystalline metal. A thickness between 200-300 nm was targeted to ensure that the bottom reflective, metallic layer was predominately opaque with respect to IR wavelengths.

### **Fabrication.**

There are many nano-fabrication techniques used to create micro- and nano-scaled optical structures, including electron-beam lithography, direct laser writing [78], and sputtering deposition. Fabrication from this work will be conducted using AFRL facilities.

Material deposition will be accomplished in collaboration with AFRL, Materials and Manufacturing Directorate. Substrates chosen for this study consisted of p-type silicon (Si) wafers having Prime grade, 1-10  $\Omega$  resistivity, and (100) orientation. These Si wafers were obtained by AFRL from *University Wafer*. All of the designs will begin with a DCMS deposition technique that will be used for layering the metal and dielectric layers. DCMS is an ionized plasma vapor deposition technique, capable of depositing dense, uniform films at room temperatures [79]. Material deposition was within high-vacuum chamber, evacuated to a pressure at 15 mTorr for HfO<sub>2</sub> deposition and 8 mTorr for Ta, W, and Ge.

## Ellipsometric and Reflectance Measurements

The J. A. Woollam IR-VASE is capable of measuring reflection and transmission in addition to the change in polarization ( $\psi$ ,  $\Delta$ ) at the specular angle. However, this study will utilize the ellipsometric measurements to measure the change in polarization and use the SOC-100 HDR reflectometer to measure the reflectance.

There are two purposes of concern for this study to take ellipsometric measurements with the IR-VASE. First, given J. A. Woollam's modeling tools, it is possible to approximate the thickness of the structure or layers of material which compose the structure. The second and more important to this study is, using the same modeling tools, it is possible to extract the optical properties from the measured data. J. A. Woollam provides a library of preloaded materials to be used in the modeling; however, it is far from exhaustive. Many of the models are based on the data reported by Palik [46, 50, 57] and some are based on measured data from J. A. Woollam. Materials such as W, Ta, and HfO<sub>2</sub> are not included in this database. J. A. Woollam provides the means for the user to create their own models through the use of the general oscillator model. Therefore, individual films of these materials will be measured, and a general oscillator model will be used to characterize their properties. Additionally, the properties reported by Palik, while extensive for room temperature, do not contain temperature-dependent optical constants. This is due to the fact that temperature-dependent measurements are sparse in comparison to room temperature in literature. For example, materials such as Ag, Au, and Cu have been measured by a few sources but materials like W, Ta, and HfO<sub>2</sub> are not well known at this point [69, 80, 81].

The IR-VASE is capable of making measurements at incident angles between 25-90° over a wavelength range of 1-40  $\mu\text{m}$ . This study will focus on looking at measurements around the Brewster's angle (65-75°) and over a specular range of 2-20  $\mu\text{m}$ . Brewster's angle is chosen in order to maximize the difference between the p-pol and s-pol reflectances. Also, the chosen wavelength range will help cut out a lot of the inherent noise of the system that is prevalent near the upper and lower angular and specular limits of the machine.

The SOC-100 HDR reflectometer is used to make reflectance measurements. This reflectometer measures hemispherical-directional reflectance (HDR), see Figure 17. It was stated in chapter II that in this study, reflectance will be discussed in terms of DHR. DHR and HDR can be defined in terms of bi-directional reflectance distribution functions (BRDFs),

$$HDR(\theta_r, \phi_r) = \int_0^{2\pi} \int_0^{\pi/2} f_r(\theta_i, \phi_i, \theta_r, \phi_r) \cos(\theta_i) \sin(\theta_i) d\theta_i d\phi_i \quad (44)$$

$$DHR(\theta_i, \phi_i) = \int_0^{2\pi} \int_0^{\pi/2} f_r(\theta_r, \phi_r, \theta_i, \phi_i) \cos(\theta_r) \sin(\theta_r) d\theta_r d\phi_r \quad (45)$$

where  $f_r$  is the BRDF,  $\theta_i, \phi_i$  are the angles describing the incident radiation direction, and  $\theta_r, \phi_r$  are the angles describing the reflected radiation direction. These two functions can be shown to be equivalent through the law of reciprocity. The law of reciprocity states that the path of light is independent of the propagation vector. Essentially, this means that the subscripts of the angles in equations (44) and (45) can be switched from incident to reflected, and the value obtained by integration will remain the same. Therefore, HDR and DHR are the same.

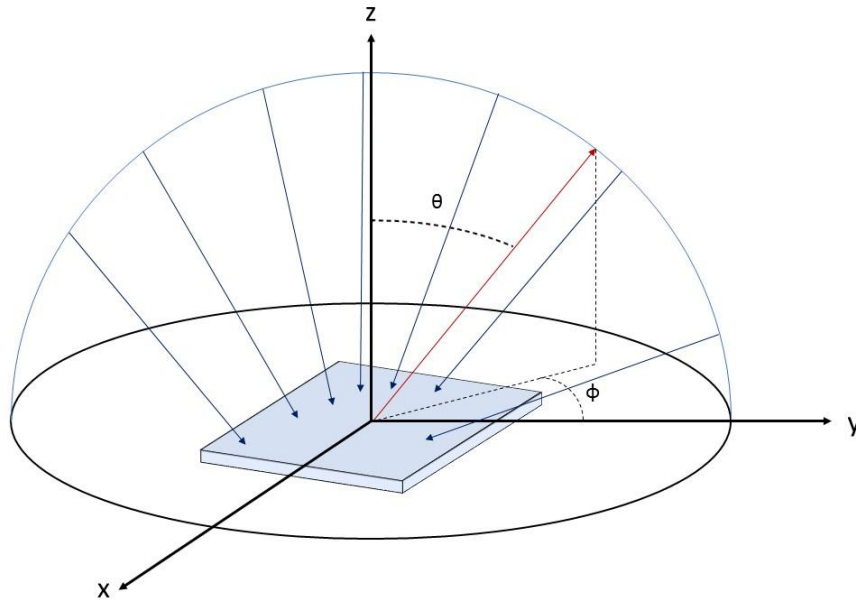


**Figure 17. Illustration of incident hemispherical radiation (blue rays) on a surface where reflected radiation (red ray) is measured at a specific direction defined by the elevation angle  $\theta$  and azimuthal angle  $\phi$ .**

## Summary

The purpose of this chapter was to define and describe the selected design, fabrication, and characterization processes for the chosen selective thermal emitters. The next chapter will follow-up by reporting the resulting fabricated designs and measured data taken for each design from room temperature up to 600 K. Lastly, the measured data will be analyzed and compared to the theoretical data obtained from Lumerical's FDTD Solutions.



## **IV. Analysis and Results**

### **Chapter Overview**

The purpose of this chapter is three-fold. The design and fabrication results for the truncated resonators are discussed first. Secondly, the reflectance measurements and inferred emittance for each design is analyzed and compared. The third purpose is to discuss the ellipsometric measurements that were made and the optical properties found through modeling. A comparison between the modeled optical properties and those found in published sources is also made.

### **Truncated Resonator Design**

The goal of the design process was to create truncated resonators which displayed spectrally selective absorption features within the wavelength range of interest, 2-20  $\mu\text{m}$ . This wavelength band was chosen because of the unique spectral transmittance and absorptance features of the atmosphere. Therefore, these designs are for devices which are exposed to the atmosphere or operate in equivalent environments. The various resonator designs with different materials (W, Ta,  $\text{HfO}_2$ , and Ge) will be modeled with various dimensions tailored to achieving absorption at wavelengths at which the atmosphere transmits, 2-5  $\mu\text{m}$  and 8-14  $\mu\text{m}$ , and absorbs, 5-8  $\mu\text{m}$  and 14-20  $\mu\text{m}$ . After appropriate designs are found through modeling, the next step is the fabrication of the

appropriate structures. Thin films of the chosen materials are also going to be fabricated and measured using the J. A. Woollam IR-VASE. Models will be used to approximate the ellipsometric measurements and derive the complex refractive index for each material. These derived properties will be used to make more accurate predictions of the resonator's behavior. Also, due to the material properties of Ge, W, and Ta combined with the type of deposition method chosen, the exact thicknesses designed for were not always realized. Therefore, the reported dimensions of the structures were estimated using an in-situ UV/IR ellipsometer during the deposition process.

### **Dimensional Analysis.**

Many designs involving the materials W, Ta, Ge, and HfO<sub>2</sub> were modeled using Lumerical's FDTD Solutions software. These designs were truncated resonators consisting of the above materials (*e.g.*, W-Ge-W or Ta-HfO<sub>2</sub>-Ta) where the interest for this study is how the different dimensions for the top metal layer and middle transparent layer affect the absorption characteristics of the structure. Specifically, this theoretical study is performed in order to determine any trends that may exist between the dimensions of the top and middle layers and the location of an absorption peak at a particular wavelength. Utilizing this information, designs were purposed in order to achieve absorption in the wavelength bands in which the atmosphere transmits, 2-5  $\mu\text{m}$  and 8-14  $\mu\text{m}$ .

The theoretical analysis began with the Ta-HfO<sub>2</sub>-Ta resonator because the absorption properties of this structure are not as well known. The effects of the top metal layer are analyzed first. Therefore, an arbitrary value for the Ge layer was chosen to be

700 nm and the bottom metal layer was 160 nm to ensure that the layer would be opaque over all wavelengths of interest. Figure 18 shows emittance results from the designs which vary from 6-40 nm for the top Ta layer, See Appendix A for larger scale versions of these figures. The minimum and maximum thicknesses of 6 nm and 40 nm were chosen due to the limitations from the fabrication process and the point at which Ta becomes optically thick in the range of 2-20  $\mu\text{m}$  which is approximately 27 nm. Note, that the values in Figure 18 show angle-independence. Therefore, the emittance values for the different thicknesses of the top Ta layer are re-plotted in order to better show any trends, see Figure 19. All of the theoretical emittance values calculated for the dimension analysis show angle-independence and will be shown in the same manner as Figure 19. The theoretical angular emittance values can be seen in Appendix A.

Reduced emittance, centered at 3.2  $\mu\text{m}$ , 1.8  $\mu\text{m}$ , and 1.1  $\mu\text{m}$ , was observed as the thickness of the top layer increased. As the thickness of the top layer approached the value at which Ta is considered optically thick, less light is transmitted through the top layer until all of the light is reflected or absorbed. Therefore, a target thickness of 6 to 10 nm was chosen for the top Ta layer in order to optimize the transmission of incident light into the cavity.

This analysis was also performed for W structures, see Figure 20. The same trend was observed for these structures with a first-order peak centered at 6.9  $\mu\text{m}$ . The optimal target thickness chosen for W was also 6 to 10 nm.

Another analysis was done for the thickness of the transparent layer. Given a top Ta layer of 6 nm for the Ta-HfO<sub>2</sub>-Ta structure, theoretical simulations were performed

for HfO<sub>2</sub> layers in the range of 150 nm to 2.5  $\mu\text{m}$ . Figure 21 shows the inferred emittance results for designs for HfO<sub>2</sub> layers of 150 nm to 1  $\mu\text{m}$ .

As the transparent layer becomes thicker, the optical path length in the resonator increases causing the wavelength of the first-order mode in the resonator to increase. This pushes the first-order emittance peak out to longer wavelengths. As it can be seen in Figure 21, for the 300-nm case, the first-order emittance peak occurs at approximately 1.8  $\mu\text{m}$ , whereas for the 1- $\mu\text{m}$  structure, the first-order peak occurs at 4.41  $\mu\text{m}$ . The peak for the 300-nm design, at 1.8  $\mu\text{m}$ , lies within an atmospheric transmittance band. The design with 700 nm of HfO<sub>2</sub> shows an emittance peak centered at 3.31  $\mu\text{m}$  which is in the wavelength band, 3.22-3.41  $\mu\text{m}$ , at which the atmosphere transmits; and the model for a HfO<sub>2</sub> layer of 1  $\mu\text{m}$  displays an emittance peak at 4.42  $\mu\text{m}$  which also lies in an transmittance absorption band. Due to time constraints, only the Ta-HfO<sub>2</sub>-Ta 6-300-160 nm sample was able to be fabricated.

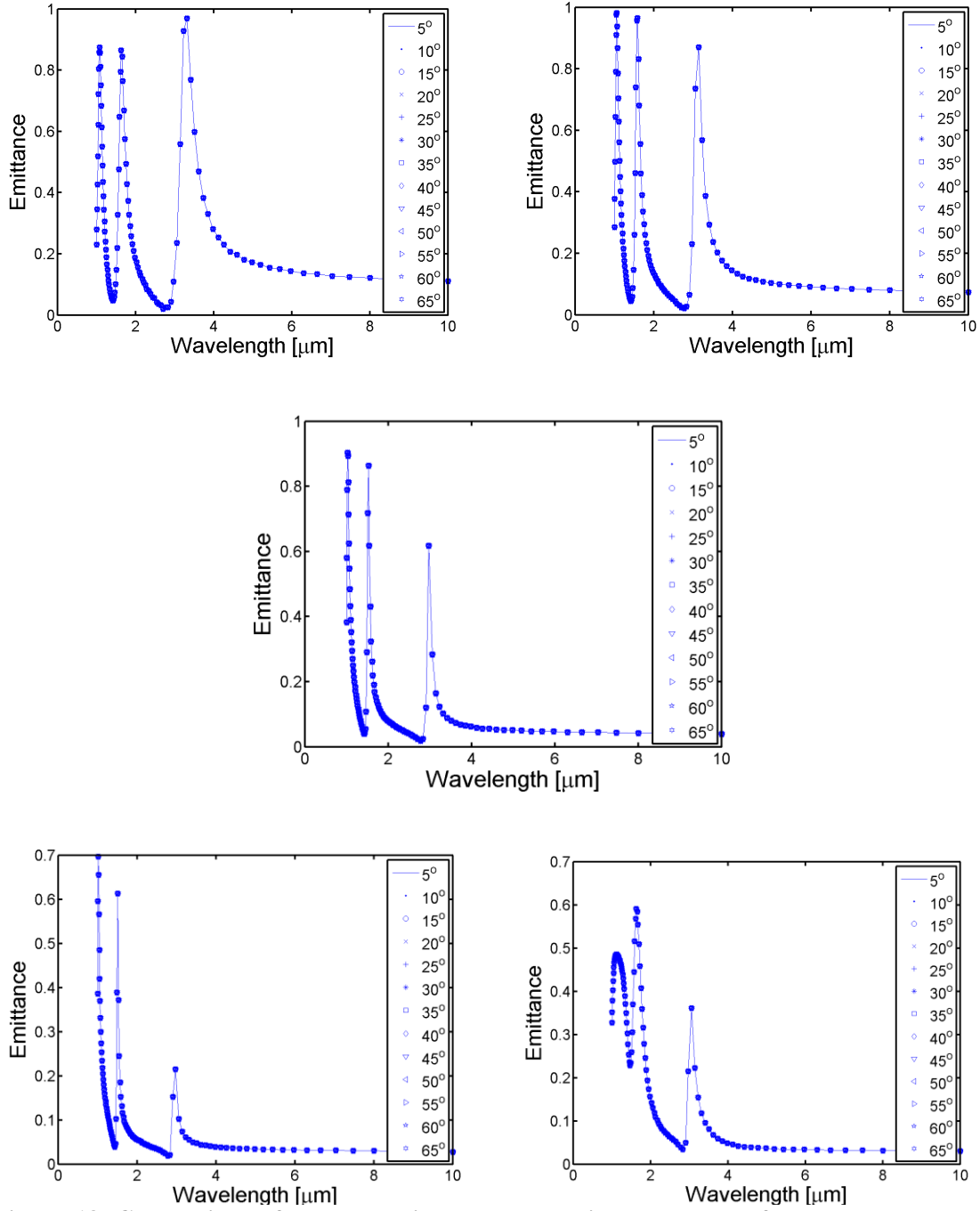


**Figure 18.** Comparison of the theoretical angular emittance spectra for a p-pol source on a Ta-HfO<sub>2</sub>-Ta truncated resonator with varying thicknesses of 6nm (top left), 10nm (top right), 20nm (middle), 30nm (bottom left), and 40nm (bottom right) for the top, optically thin Ta layer

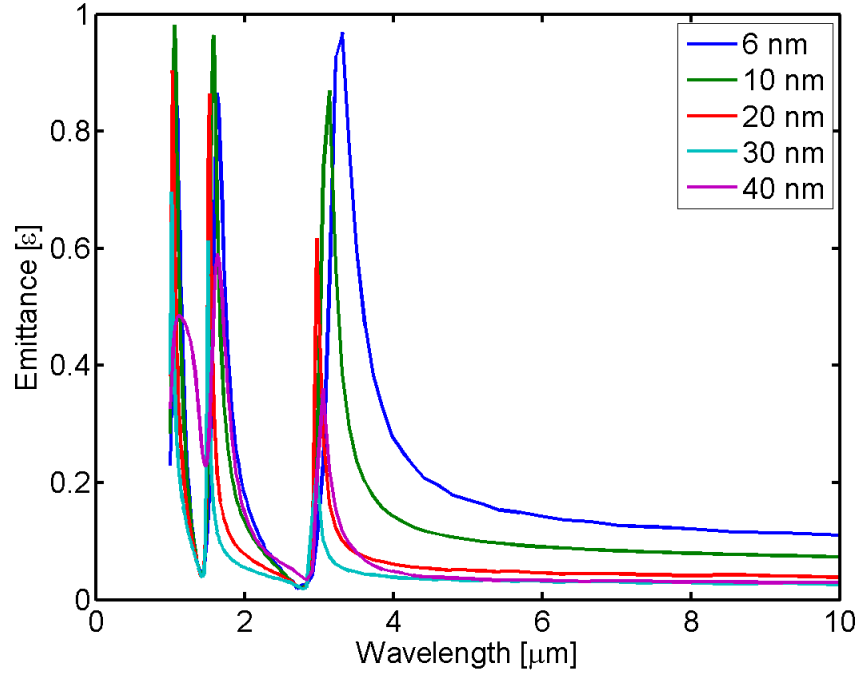


**Figure 19.** Comparison of the angle-independent theoretical emittance spectra for a p-pol source on a Ta-HfO<sub>2</sub>-Ta truncated resonator with varying thicknesses of 6 nm, 10 nm, 20 nm, 30 nm, and 40 nm for the top, optically thin Ta layer

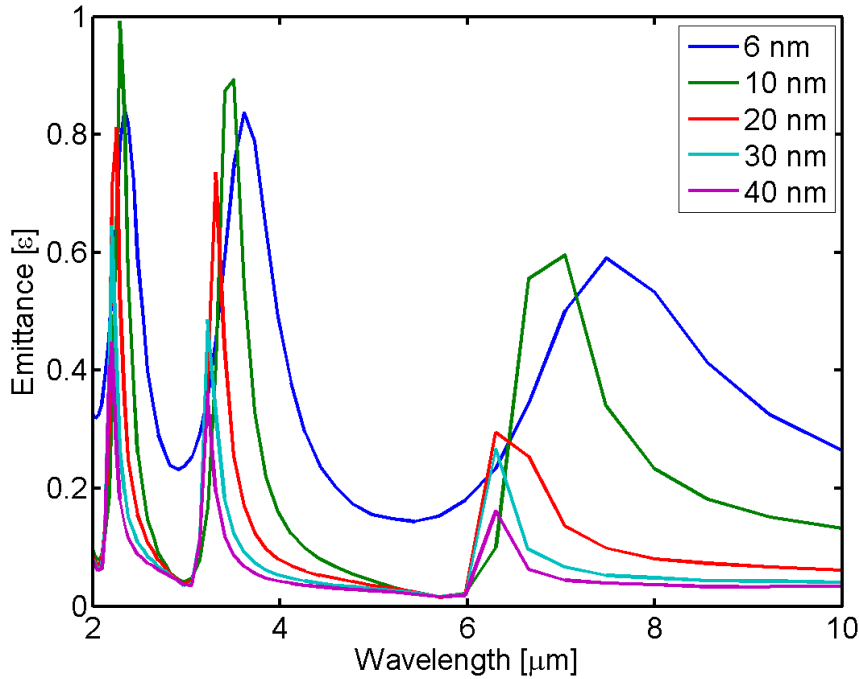


**Figure 20.** Comparison of the angle-independent theoretical emittance spectra for a p-pol source on a Ta-HfO<sub>2</sub>-Ta truncated resonator with varying thicknesses of 6 nm, 10 nm, 20 nm, 30 nm, and 40 nm for the top, optically thin W layer

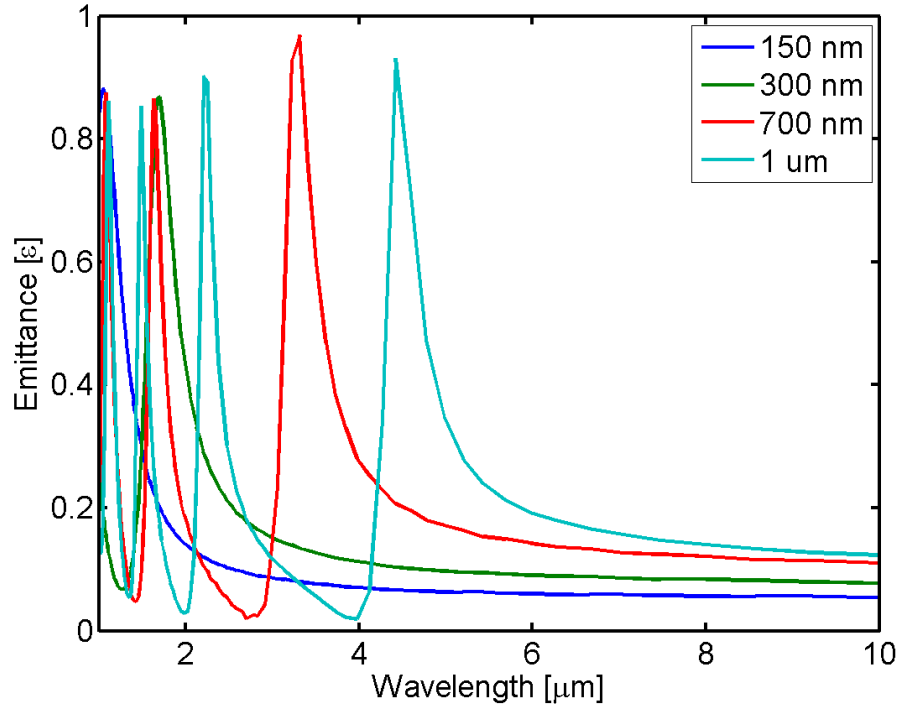


**Figure 21. Comparison of the angle-independent theoretical emittance spectra for a p-pol source on a Ta-HfO<sub>2</sub>-Ta truncated resonator with varying thicknesses of 150 nm, 300 nm, 700 nm, and 1  $\mu$ m for the middle, transparent HfO<sub>2</sub> layer**

This analysis was repeated for the Ta-Ge-Ta, W-Ge-W, and W-HfO<sub>2</sub>-W structures. The optimal thicknesses for Ge layers in both of the Ta-Ge-Ta and W-Ge-W structures were found to be 700 nm for absorption peaks at 6.9  $\mu$ m and 7.5  $\mu$ m, respectively. See Figures 71-77 and 78, 83-87, respectively, in the Appendix A. The target optimal thickness for the HfO<sub>2</sub> layer in the W-HfO<sub>2</sub>-W structure was also estimated to be 700 nm in order to achieve absorption at 3.8  $\mu$ m. See Figures 88-94 in the Appendix A. Also, every structure showed angle-independence. The emittance values were the exactly the same for incidence angles of 5°-65°. This is not a correct depiction of the behavior of these structures. For, as the incident angle increases, the surface will appear to be smoother and less emittance will be observed because reflection will increase.

These incorrect values are attributed to the extraction code that was used to correct the propagation vectors for the broadband source pulse used in Lumerical's FDTD Solutions.

### **Spectroscopic Ellipsometry.**

Ellipsometric measurements were taken of thin layers of tungsten (W), tantalum (Ta), germanium (Ge), and hafnium oxide ( $\text{HfO}_2$ ). Measurements were taken using J. A. Woollam's IR-VASE over the wavelengths of 2-12  $\mu\text{m}$  and 2-20  $\mu\text{m}$ . Using J. A. Woolam's VASE32 software, models were fit to the ellipsometric measurements in order to extract the optical constants of the DCMS-deposited metals.

The VASE32 software comes with a default library of models for common dielectrics, metals, and semiconductors in the IR wavelengths. Unfortunately, this library does not contain models for Ta, W, and  $\text{HfO}_2$ . Therefore, general oscillator models were used to characterize their properties. Also, because default models for W and Ta do not exist in the IR library, optically thick samples, between 145 and 200 nm, of W and Ta were fabricated and characterized using the general oscillator model in order to provide a baseline for building a final model for the thin samples.

Determining the thickness of any material using ellipsometry requires that a portion of the IR radiation travel through the entire film and return back through the structure to the detector. Due to the absorption of the optically thick samples of W and Ta, the thickness of the fit model will not always be exact. Also, the layers are assumed to be homogenous and this is not true. Actually, a small amount of the surface metal has oxidized at room temperature and has certain unique absorption features which the pure metal does not have. Since this was not accounted for in the model, the software tried to



fit the model to these features as best as possible by changing all the parameters until a best fit was achieved. Further study and more work with W and tungsten oxides and their optical properties would need to be conducted in order to fully understand and observe these effects.

Also, it was previously mentioned that any deposited material is amorphous to some extent. Therefore, it should be expected that the material properties will vary due to changes in the microstructure and purity. The accuracy of the derived optical constants depends on fit of the model to the ellipsometric measurements, which in turn depends on the ability of the user to characterize each aspect of the structure adequately. The accuracy of the model to the fabricated structure depends on the user's knowledge of the structure, such as surface roughness and oxidation. The model does not inherently account for these characteristics but does provide the necessary tools so the user can properly model their effects.

The thickness of the thick W was not allowed to fit and was set to 140 nm. This is done because this layer of W is optically opaque, and the optical properties do not depend on the thickness. The ellipsometric measurements, amplitude ratio  $\psi$  and phase difference  $\Delta$ , made using the IR-VASE for the optically thick W sample are shown with the associated fitted model in Figure 22. Making measurements over multiple angles produces multiple data sets of  $\psi$  and  $\Delta$ . Multiple data sets increases the uniqueness of the curves, confidence of the fit, and confidence in the resulting optical constants.

Seventeen parameters were used to fit the model to the measured data. The VASE32 software reports the error in each of these parameters as they are adjusted in order to fit the measured values, and propagates this error forward into the modeled  $\psi, \Delta$

values. This software also reports the error determined for the measured values, and Figure 22 displays the error for the measured and model values as error-bars. It can be seen that the error-bars for all of the angles for the measured and models overlap. This indicates that the optical properties of the thick ( $\sim 145$  nm) W are angle-independent at large angles close to the Brewster angle.

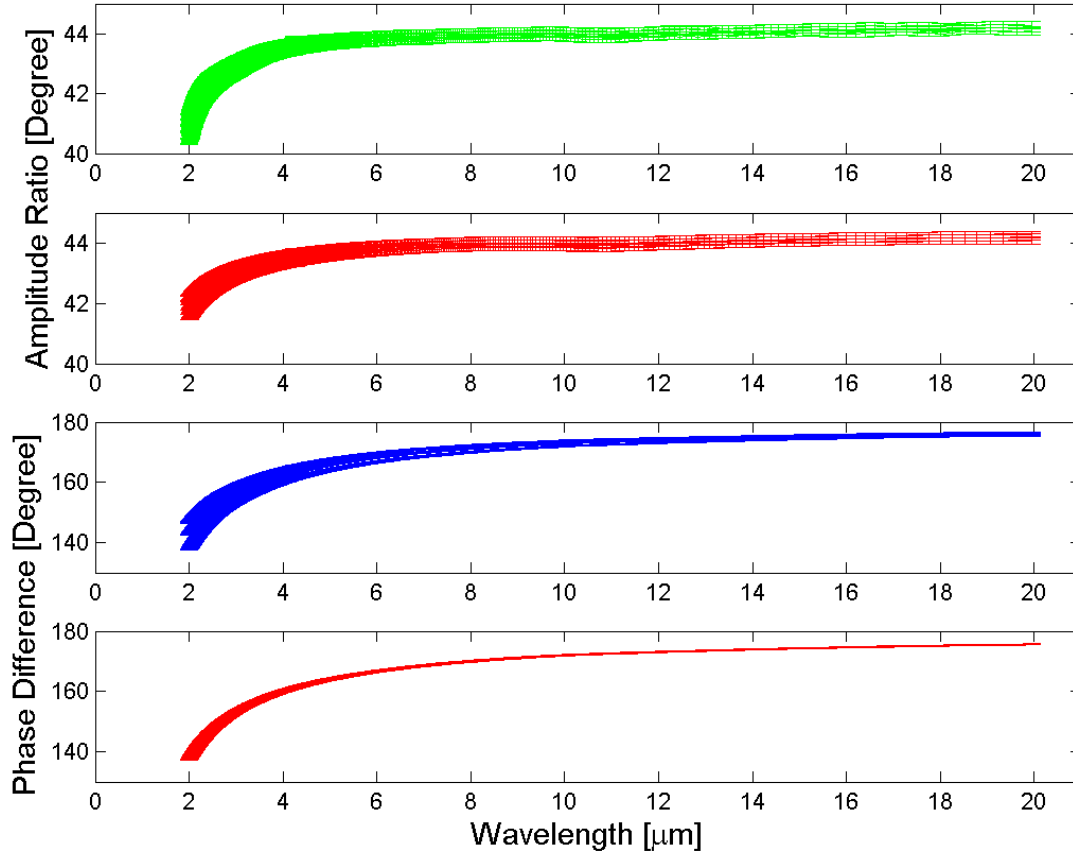


**Figure 22.** Amplitude ratio  $\psi$  (green) and phase difference  $\Delta$  (blue) of ellipsometric measurements made using the J. A. Woollam Infrared Variable Angle Spectroscopic Ellipsometer (IR-VASE) for incident angles of  $69^\circ$ ,  $71^\circ$ , and  $73^\circ$  on an optically thick layer of W (145 nm) with associated model fits (red). Error in the measured and modeled values are plotted as error-bars.

This model was used as a basis to characterize the measured data for the thin layer of W ( $\sim 10$  nm). Unfortunately, the measured data for the thin layer of W was not accurately modeled thick W model that was created. A new oscillator model had to be

created with ten parameters used to fit the measured data. Figure 23 shows the ellipsometric measurements made for the optically thin layer of W ( $\sim 10$  nm) and the associated fitted model along with the respective error-bars. Since there is no overlap of the error in the amplitude ratio values for incident angles of  $69^\circ$ ,  $71^\circ$  and  $73^\circ$ , then the amplitude ratio for the thin W layer ( $\sim 10$  nm) is angle-dependent. However, the opposite is true for the phase difference.

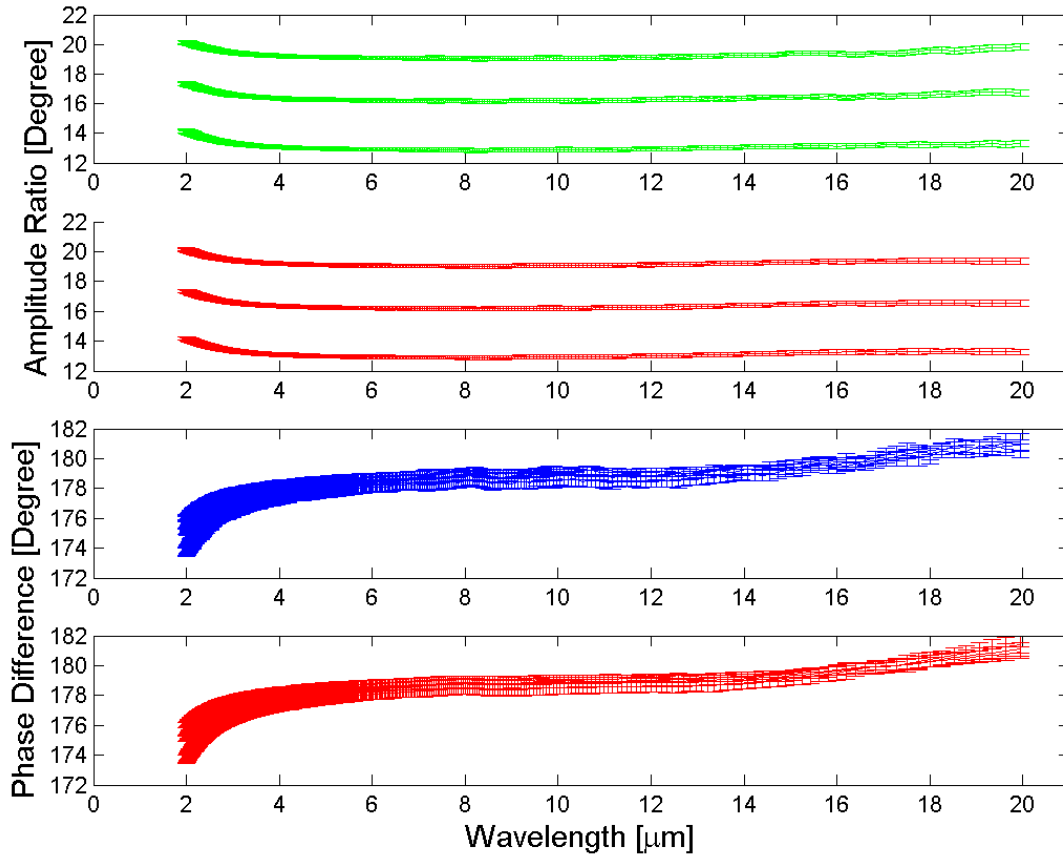


**Figure 23.** Amplitude ratio  $\psi$  (green) and phase difference  $\Delta$  (blue) of ellipsometric measurements made using the J. A. Woollam Infrared Variable Angle Spectroscopic Ellipsometer (IR-VASE) for incident angles of  $69^\circ$ ,  $71^\circ$ , and  $73^\circ$  on an optically thin layer of W ( $\sim 10$  nm) with associated model fits (red). Error in the measured and modeled values are plotted as error-bars.

From the model, wavelength-dependent optical constants can be derived, and the error from the  $\psi$ ,  $\Delta$  measurements was propagated through to the  $n$ ,  $k$  values. The

constants for the thick and thin layers are compared against those used in the Lumerical FDTD Solutions software which was used to make theoretical computations of the reflectance values of the various resonator designs, see Figure 24 for comparison. FDTD Solutions uses the optical properties reported for bulk W from Palik [45] and those reported by CRC [46] for Ta.

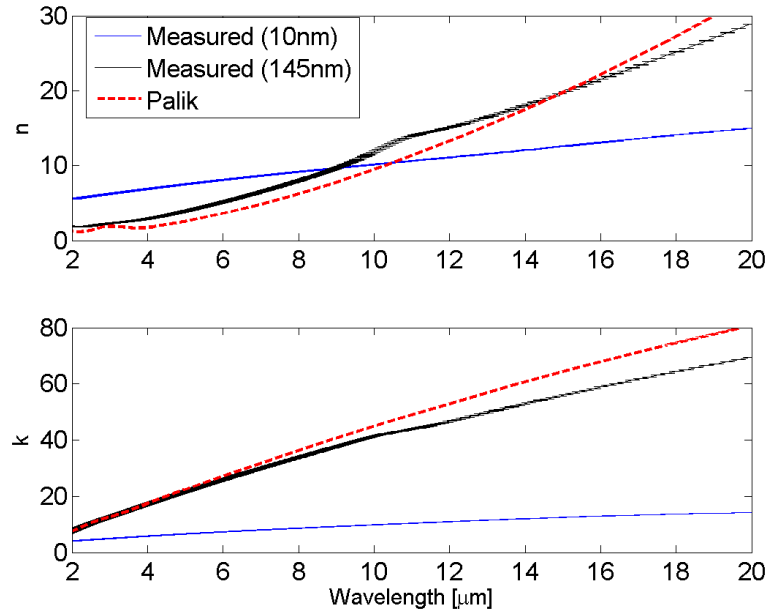


**Figure 24. Measured real ( $n$ ) and imaginary ( $k$ ) parts of index of refraction for DCMS-deposited optically thin, 10 nm, (blue) and thick, 145 nm, (black) W compared with error-bars plotted against bulk optical constants reported in Palik [45] (red) and used in the Lumerical FDTD Solutions software.**

The measured index of refraction values from the DCMS-deposited thin W layer, 10 nm, deviated significantly from the literature/FDTD Solutions values while the values for the thick layer, 145 nm, followed the same trend as the literature. The small error indicates high-confidence in the model values for the parameters used. The Palik values for  $n$  and  $k$  rose quickly with increasing wavelength while the derived  $n$  and  $k$  values for the thin W layer increased at a smaller rate and leveled off to values of 12 and 11. The

values for the thick W layer started deviating from the bulk, literature values around 16  $\mu\text{m}$ .

This process was repeated for Ta. The model was fit to the measurements using 9 and 11 parameters for the thick ( $\sim 170$  nm) and thin ( $\sim 10$  nm) layers of Ta, respectively. The measured optical properties of the DCMS-deposited layers of Ta are compared to the bulk CRC values in Figure 25.

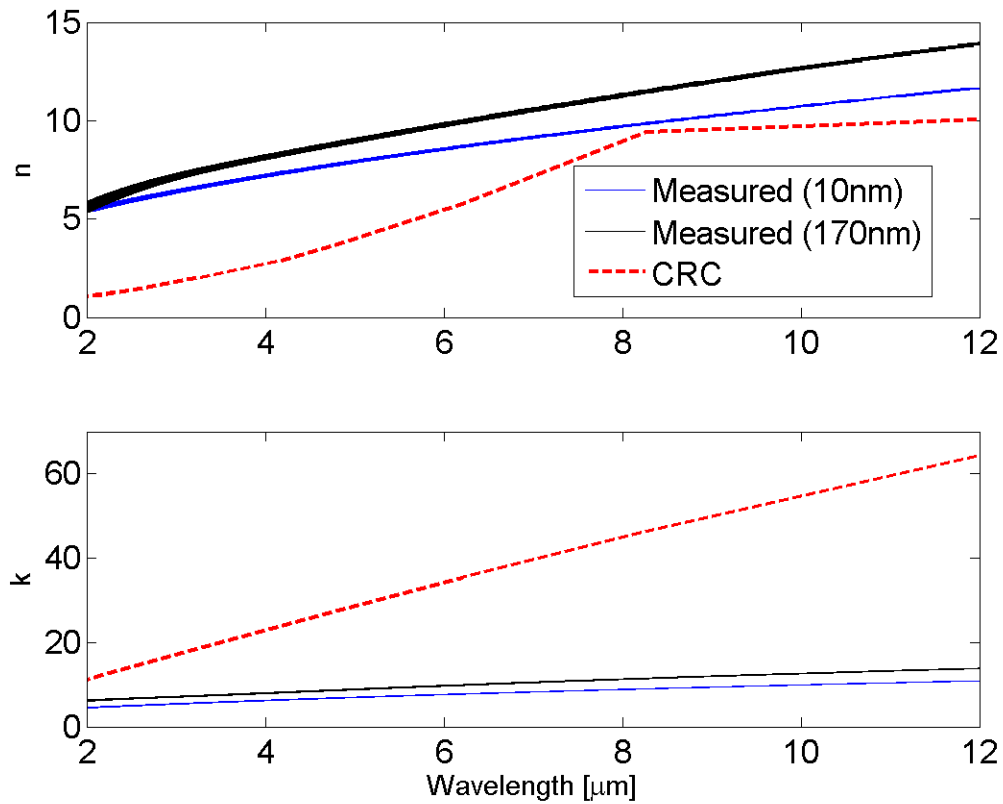


**Figure 25. Measured real ( $n$ ) and imaginary ( $k$ ) parts of index of refraction for DCMS-deposited optically thin (10 nm) and opaque (170 nm) Ta layers with error-bars compared against bulk optical constants reported in CRC [46] (red) and used in Lumerical FDTD Solutions solutions.**

The measured values for the real part of the refractive index,  $n$ , for both the optically thin and opaque layers deviated significantly from the bulk values reported by CRC [46] at lower wavelengths. At wavelengths above 8  $\mu\text{m}$ , the measured values for the

optically thin layer tended towards the literature values while the values for the optically opaque layer increased and diverged from the literature values. The measured values for the imaginary component,  $k$ , of the refractive index deviated significantly from the CRC values over all observed wavelengths, 2-12  $\mu\text{m}$ . The CRC values rose quickly with increasing wavelength while the derived values leveled off to values of 11 and 15 for the thin and opaque layers, respectively.

Next, Germanium (Ge) and hafnium oxide ( $\text{HfO}_2$ ) layers of about 300 nm were fabricated on thick W and Ta layers, and the measuring and modeling process was repeated. Twelve and ten parameters were used to fit the Ge and  $\text{HfO}_2$  models, respectively. Figures 26 and 27 display the derived complex refractive index values from the models for Ge and  $\text{HfO}_2$ , respectively, and compare them to values found in literature. The extracted Ge values for the refractive index show close agreement with the literature values up to 10  $\mu\text{m}$ . After 10  $\mu\text{m}$ , Palik reports an oscillatory nature to the refractive index while the extracted values stay constant until roll-off at 16  $\mu\text{m}$ . Also, the extracted values show absorption features in Ge between 8-20  $\mu\text{m}$ .

The Lts Research Lab [63] reported values for  $\text{HfO}_2$  out to 8  $\mu\text{m}$ . The extracted values for  $\text{HfO}_2$  from the model agreed with the values reported in [63]. The absorption coefficient values show that  $\text{HfO}_2$  transmits well out to 9  $\mu\text{m}$ .

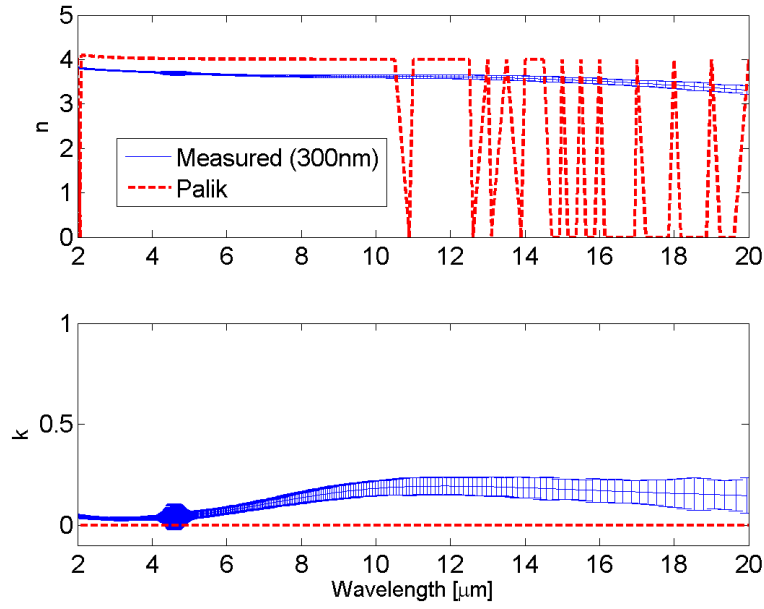


**Figure 26.** Measured (blue) real ( $n$ ) and imaginary ( $k$ ) parts of index of refraction for DCMS-deposited Ge layer (300 nm) with error-bars compared against bulk optical constants reported in Palik [50] (red) and used in Lumerical FDTD Solutions solutions.

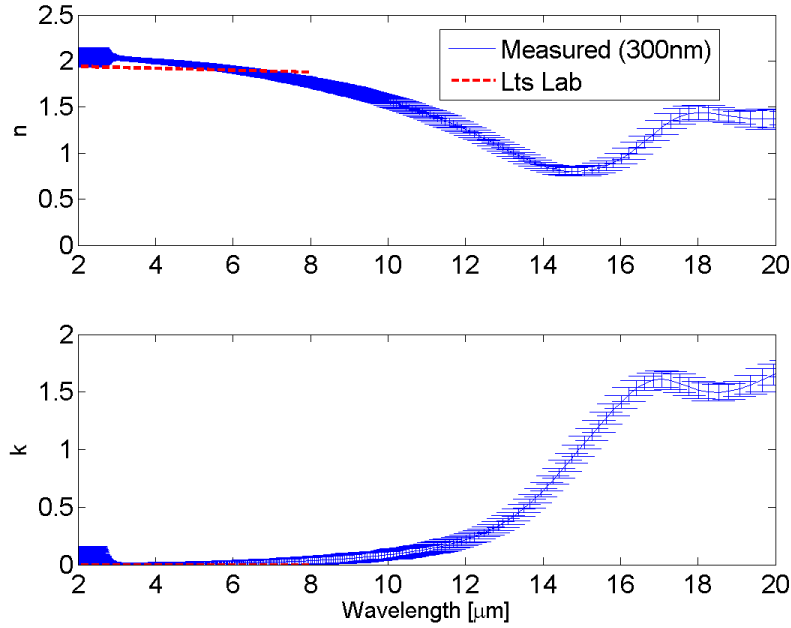


**Figure 27.** Measured (blue) real ( $n$ ) and imaginary ( $k$ ) parts of index of refraction for DCMS-deposited  $\text{HfO}_2$  layers with error-bars compared against bulk optical constants reported by Lts Research Lab [63] (red).

Lastly, these extracted optical properties were fed back into the theoretical modeling process. To conserve time, a different numerical method was used to compute the updated theoretical values. The method implemented here was the enhanced transmission matrix approach based on Moharam *et al.* [82]. Figures 28-31 show the updated emittance values for each of the chosen designs, W-HfO<sub>2</sub>-W (6-700-200 nm), Ta-HfO<sub>2</sub>-Ta (6-300-700 nm), W-Ge-W (6-700-200 nm), Ta-Ge-Ta (6-700-200 nm). Comparing the updated values to those that used only bulk material parameters, the emittance peaks are broader and centered at longer wavelengths than the bulk material models, and this is true for all the models. These updated values also show the angle-dependence that was lacking in the Lumerical FDTD Solutions simulations.

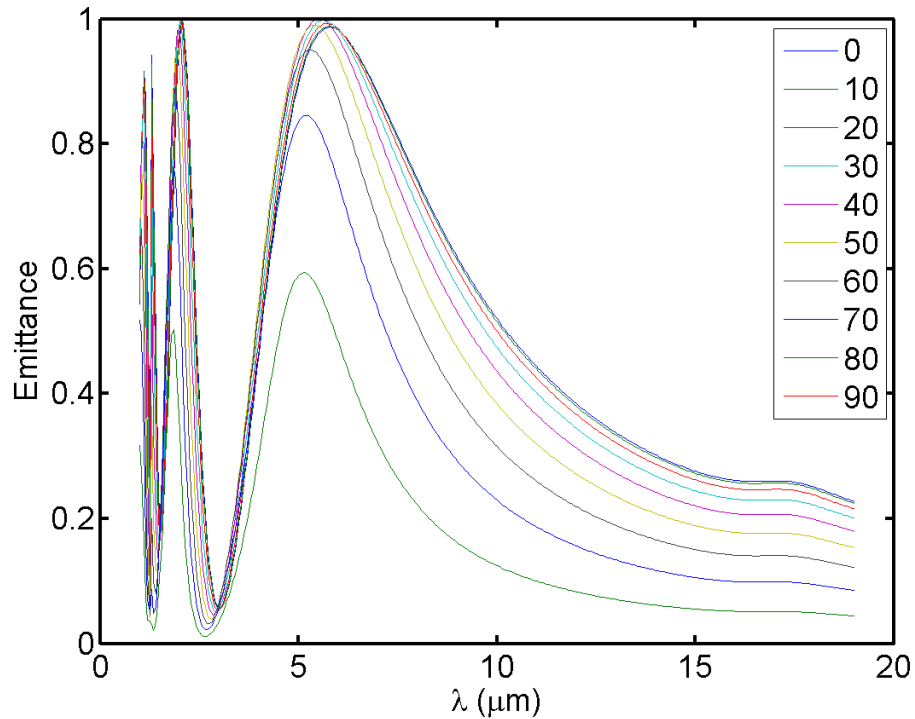


**Figure 28. Theoretical emittance values for W-HfO<sub>2</sub>-W 6-700-200 nm obtained using the enhanced transmission matrix approach with extracted optical constants from ellipsometric models for W (10nm) and HfO<sub>2</sub> (300nm) layers.**



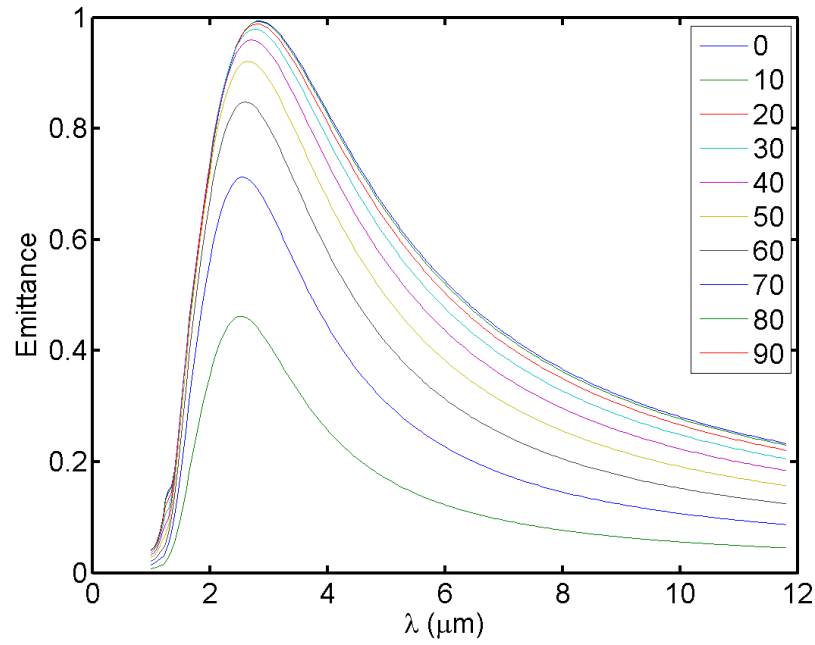


**Figure 29.** Theoretical emittance values for Ta-HfO<sub>2</sub>-Ta 6-700-200 nm obtained using the enhanced transmission matrix approach with extracted optical constants from ellipsometric models for Ta (10nm) and HfO<sub>2</sub> (300nm) layers.

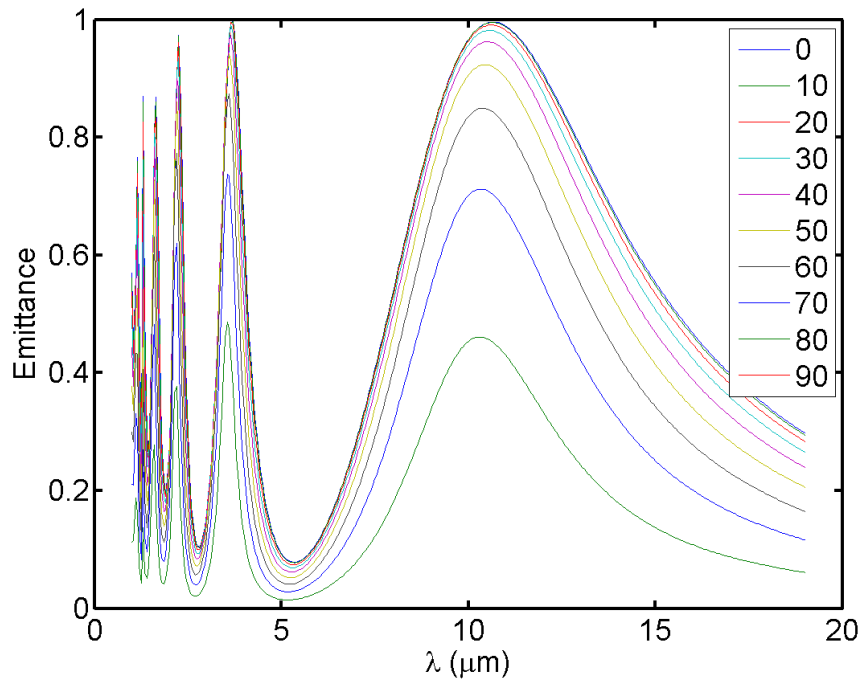


**Figure 30.** Theoretical emittance values for W-Ge-W 6-700-200 nm obtained using the enhanced transmission matrix approach with extracted optical constants from ellipsometric models for W (10nm) and Ge (300nm) layers.

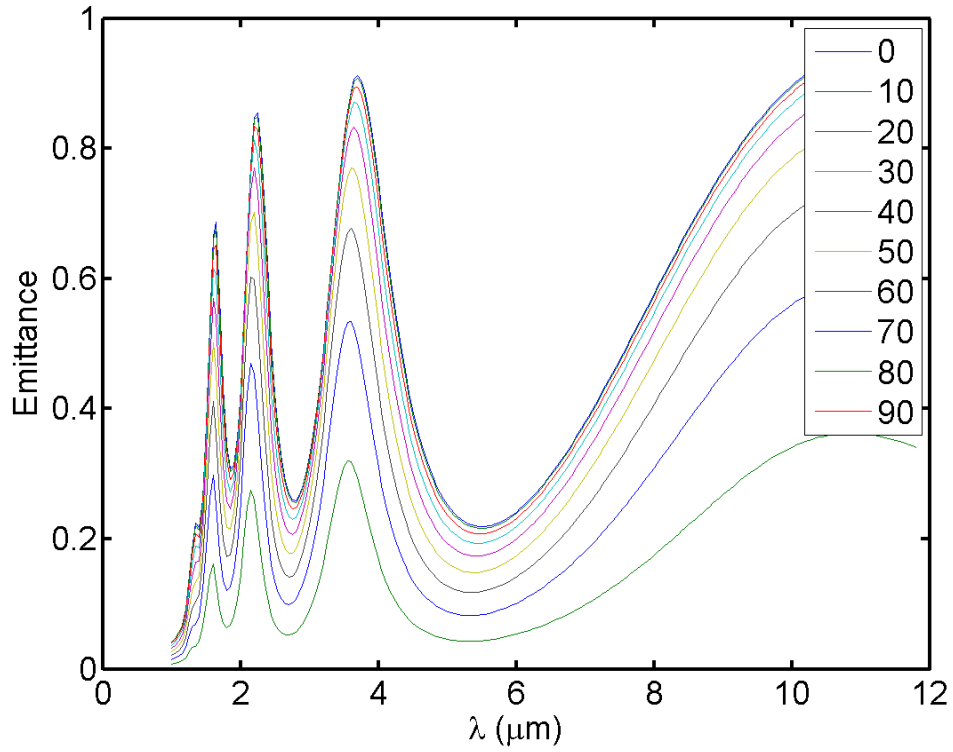


**Figure 31. Theoretical emittance values for Ta-Ge-Ta 6-700-200 nm obtained using the enhanced transmission matrix approach with extracted optical constants from ellipsometric models for Ta (10nm) and Ge (300nm) layers.**

#### **Sample 1 (W-HfO<sub>2</sub>-W 10-701-145nm)**

##### **Fabrication Results.**

The skin depth of W and Ta was previously observed (Figure 16), and in the range of 2-20  $\mu\text{m}$ , W and Ta become optically opaque at about 37 nm and 27 nm, respectively. It was also observed that the skin depth becomes thicker at higher temperatures. Therefore, a thickness of 130-200 nm for the bottom W layer was targeted to ensure that this layer was opaque. The thickness of the transparent HfO<sub>2</sub> layer was estimated to be 701 nm and the top Ta layer came to be about 10 nm which was well

under the 27 nm at which it becomes opaque. These layers were deposited using a DCMS deposition technique, and the thicknesses are close to those which were determined from the theoretical analysis. The estimated dimensions of this resonator are 10-701-145 nm.

An SEM of Sample 1 looking down at 45° from surface normal at 20,000x magnification is shown in Figure 32. Unfortunately, SEM's of the same edge of the pre- and post-heat samples were not obtained. The pre-heat test SEM was taken from a piece of the fabricated structure which was cut down from a 2-inch diameter to a 1-inch square piece in order to perform heat testing. This is the case for all SEM's in this study.

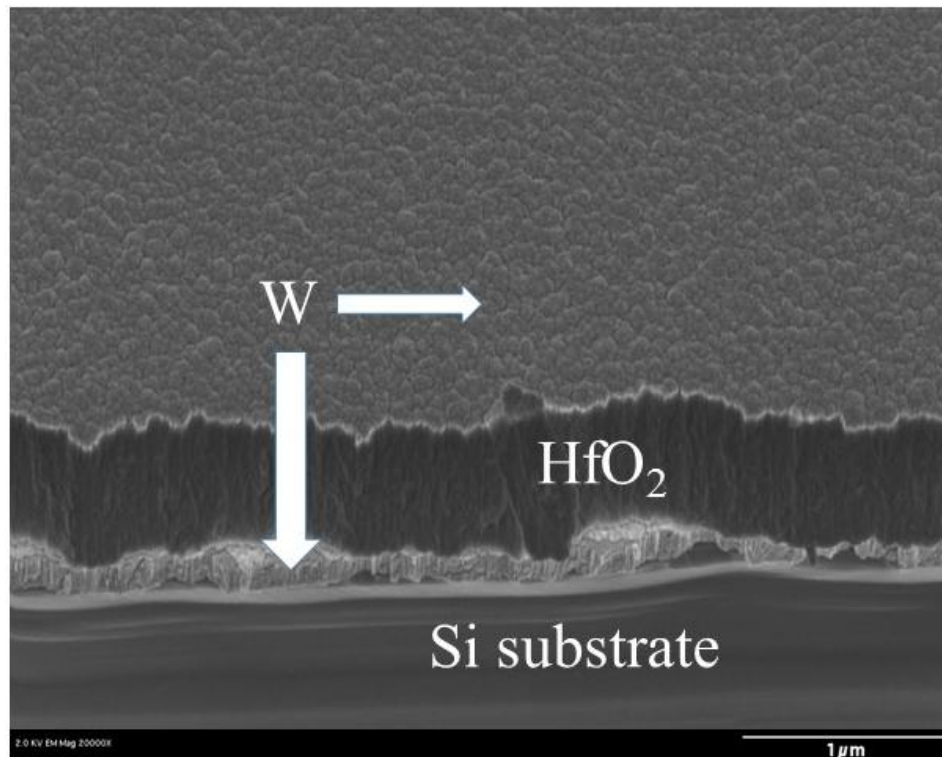


**Figure 32. SEM of a pre-heated W-HfO<sub>2</sub>-W truncated resonator of dimensions 10-701-145 nm on a silicon substrate. The W and HfO<sub>2</sub> layers were deposited using the Direct Current Magnetron Sputtering (DCMS) technique. The micrograph was taken at 20,000x magnification with 2 kV at 45° from surface normal.**

The surface W layer displays bumps that are due to the granular structure of HfO<sub>2</sub>. Also, there is some variation in the thicknesses of all the layers. However, these

small changes in thickness will not make a significant impact for the wavelength range, 2-20  $\mu\text{m}$ , of interest for this study.

### **Reflectance Measurements.**

Reflectance measurements were taken using AFIT's SOC-100 HDR reflectometer at incident angles of 15°, 25°, 35°, 45°, 55°, 65°, and 75°. Observing the inferred emittance data from the collected reflectance data at room temperature for this structure, Figure 33 (top left), three absorption peaks centered at 2.008, 5.53, and 14  $\mu\text{m}$  can be identified. The absorption peaks centered at 2.008 and 5.53  $\mu\text{m}$  do not diminish until the angle of incidence starts to approach the grazing angle, angles greater than 55°. The absorption feature at 14  $\mu\text{m}$  shows significant angular dependence, where at angles smaller than 45°, this peak is barely noticeable. The theoretical values are shown in Figure 28 and repeated here in Figure 33 (top right) in order to make a comparison with the measured values. Since, the estimated fabricated thicknesses are different than those for the designed structures, theoretical emittance values were computed for those estimated thicknesses using the matrix approach. These values can also be seen in Figure 33 (bottom right). It will be shown, that the estimated thicknesses after fabrication for all of the structures are different from the designs, and theoretical emittance values are re-calculated using these thicknesses.

The theoretical values were accurate in predicting the location and width of the measured emittance peaks at 2.008 and 5.53  $\mu\text{m}$ . However, the measured emittance of the first-order peak is 10% lower than the theoretical values. This points to a thicker top

metal layer than what was estimated. A closer look at the ellipsometric measurements taken during fabrication should be taken.

Comparing the theoretical values obtained using the designed thicknesses (6-700-200 nm) to the measured data, the measurements show less emittance as incident angle increases, about 0.4 at  $75^\circ$  for the  $5.53\ \mu\text{m}$  peak compared to 0.6 at  $80^\circ$  of the same peak for the theoretical values. This is due to the increased thickness of the top metal layer. Also, the theoretical values failed to predict the emittance feature at  $14\ \mu\text{m}$ . Therefore, this feature is likely not a result of the resonator design. In order to verify this, a  $\text{HfO}_2$ -W 300-150 nm structure was fabricated and the reflectance of the structure was measured. The emittance results, Figure 34, show the same absorptance/emittance feature at  $14\ \mu\text{m}$ . Therefore, this feature is due to the absorptance of the  $\text{HfO}_2$  layer. The absorptance increases with increasing incident angle due to the increased path length the light must travel through the  $\text{HfO}_2$  layer.

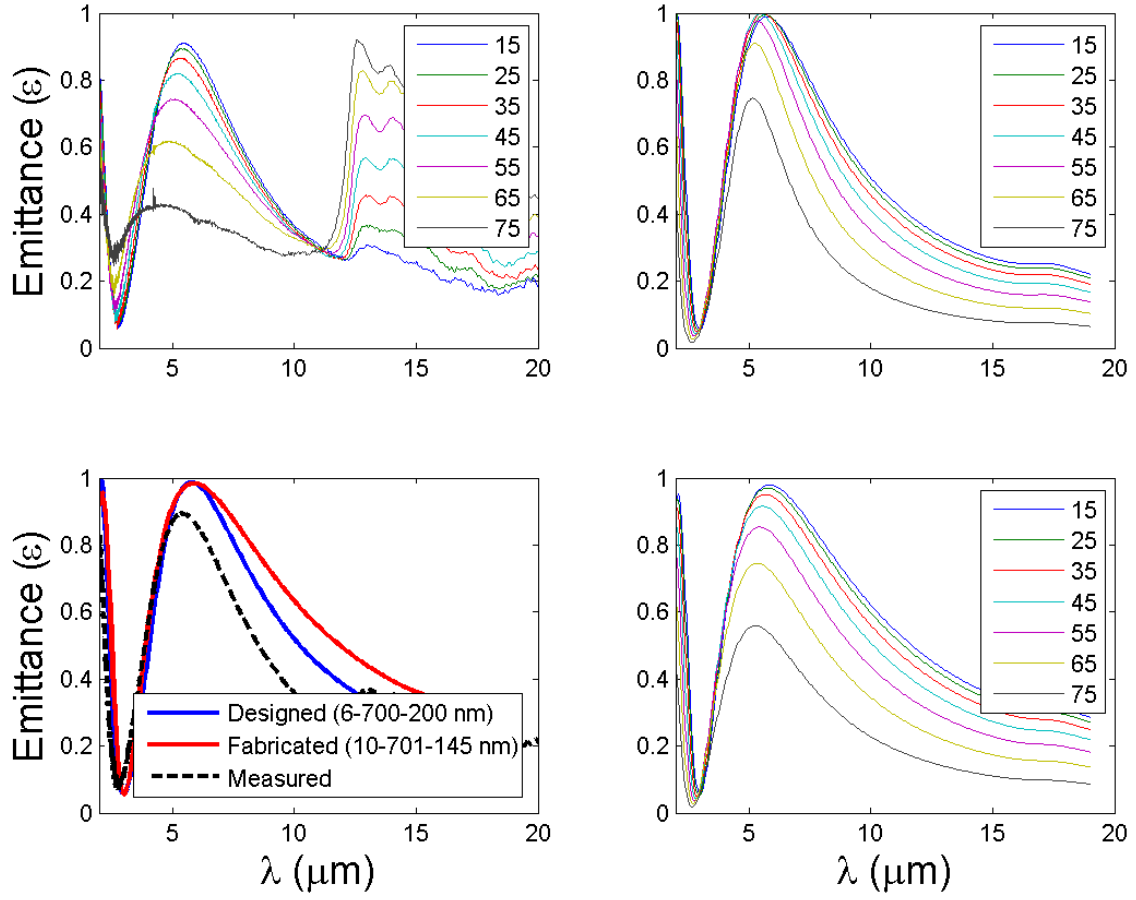


**Figure 33.** Measured (top left) and theoretical emittance values for W-HfO<sub>2</sub>-W structure with designed thicknesses (6-700-200 nm, top right) and estimated thicknesses after fabrication (10-701-145 nm, bottom right) obtained using the enhanced transmission matrix approach with extracted optical constants from ellipsometric models for W (10nm) and HfO<sub>2</sub> (300nm). Emittance values for an incidence angle of 25° for both theoretical models and what was measured are plotted together (bottom left)

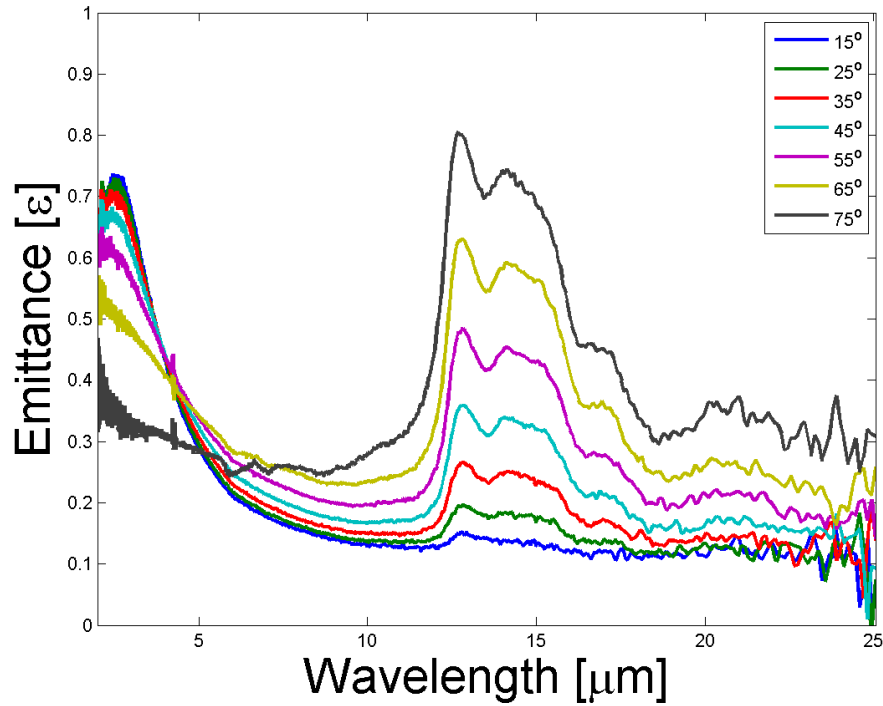


**Figure 34. Inferred angular HDR emittance (color bar) for p-pol source on a  $\text{HfO}_2\text{-W}$  structure of dimensions 303-145 nm at room temperature.**

A heat test was also conducted for this structure, and measurements were made at temperatures from approximately 300 K (30 °C) to 550 K (280 °C) in 50-K increments. Figure 35 displays five emittance plots for temperatures of about 350 K, 400 K, 450 K, 500 K, and 550 K. Figure 36 displays the same information, except now each plot is for a different incident angle and each line represents a different temperature at that respective angle.

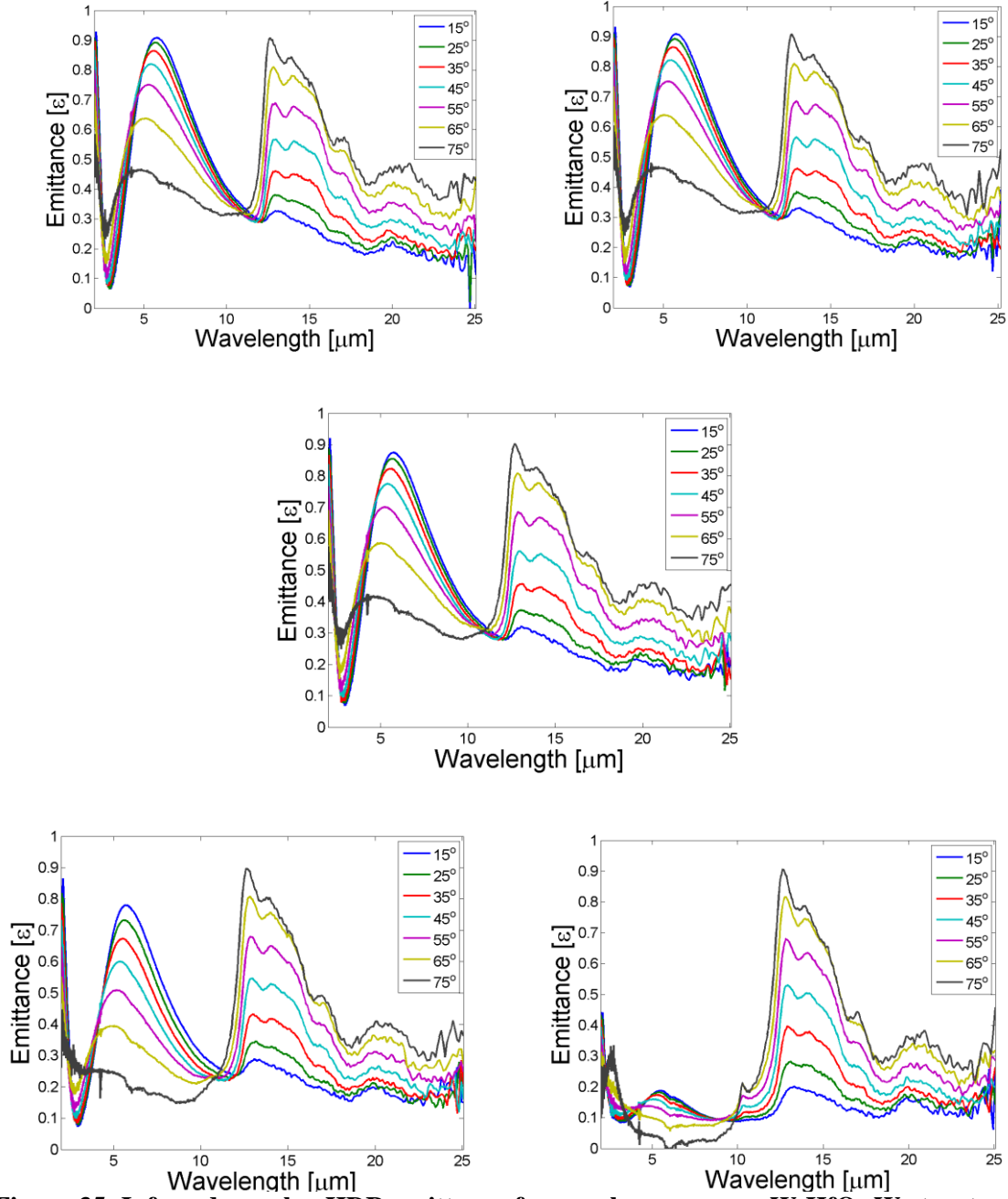


**Figure 35. Inferred angular HDR emittance for p-pol source on a W-HfO<sub>2</sub>-W structure of dimensions 10-701-145 nm at 80°C (top left), 130°C (top right), 180°C (middle), 230°C (bottom left), and 280°C (bottom right).**



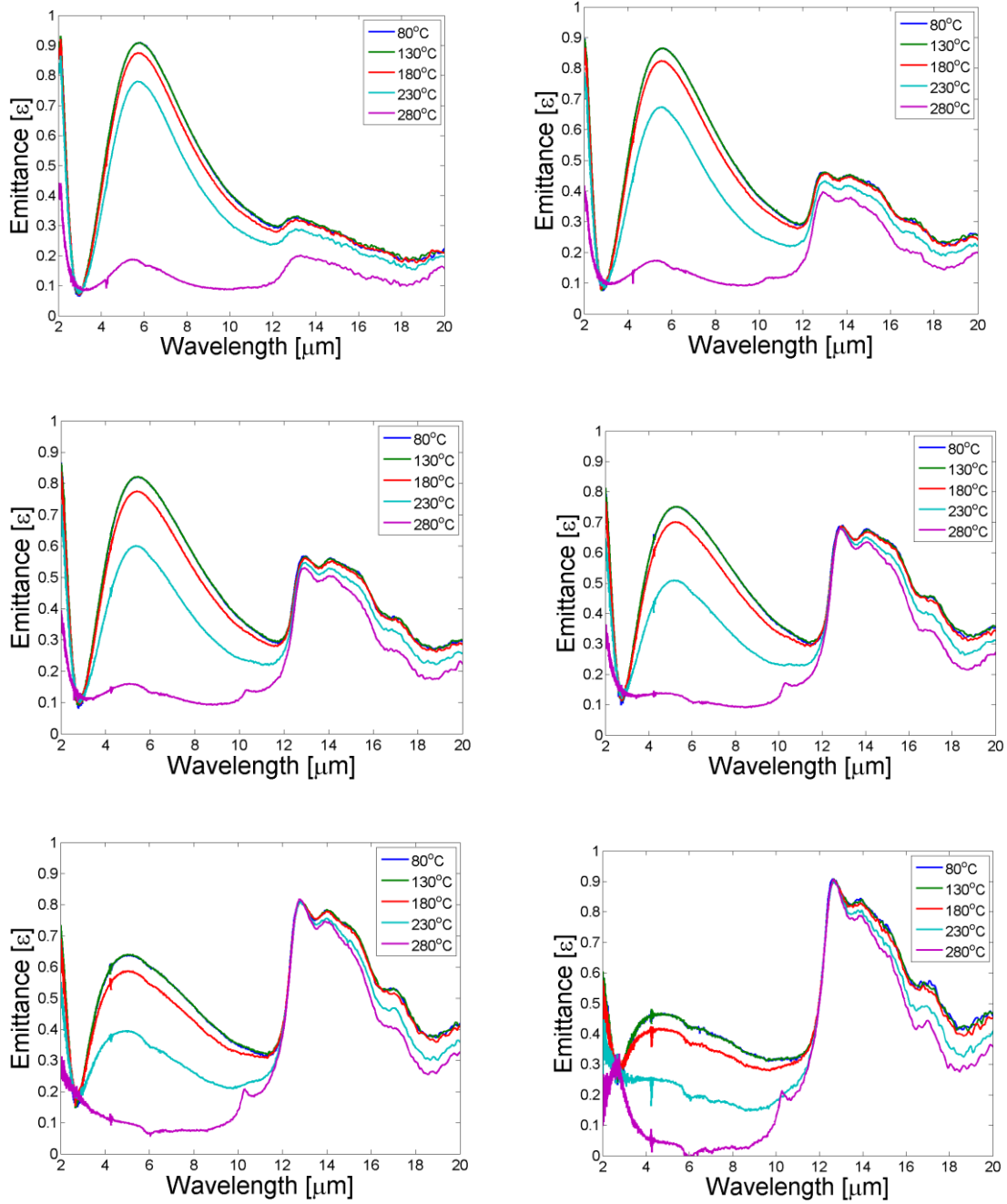


**Figure 36. Inferred angular HDR emittance for p-pol source on a W-HfO<sub>2</sub>-W structure of dimensions 10-701-145 nm for incident angles 15° (top left), 35° (top right), 45° (middle left), 55° (middle right), 65° (bottom left), 75° (bottom right) at temperatures 80°C, 130°C, 180°C, 230°C, 280°C, and 330°C.**

A significant change can be noticed in the measurement at 280 °C from that taken at 230 °C. Specifically, a 70% drop in absorption centered at 5.53  $\mu\text{m}$  can be seen from

the measurement at 230 °C to that performed at 280 °C. Another SEM was taken to help identify any changes in the structure, see Figure 37.

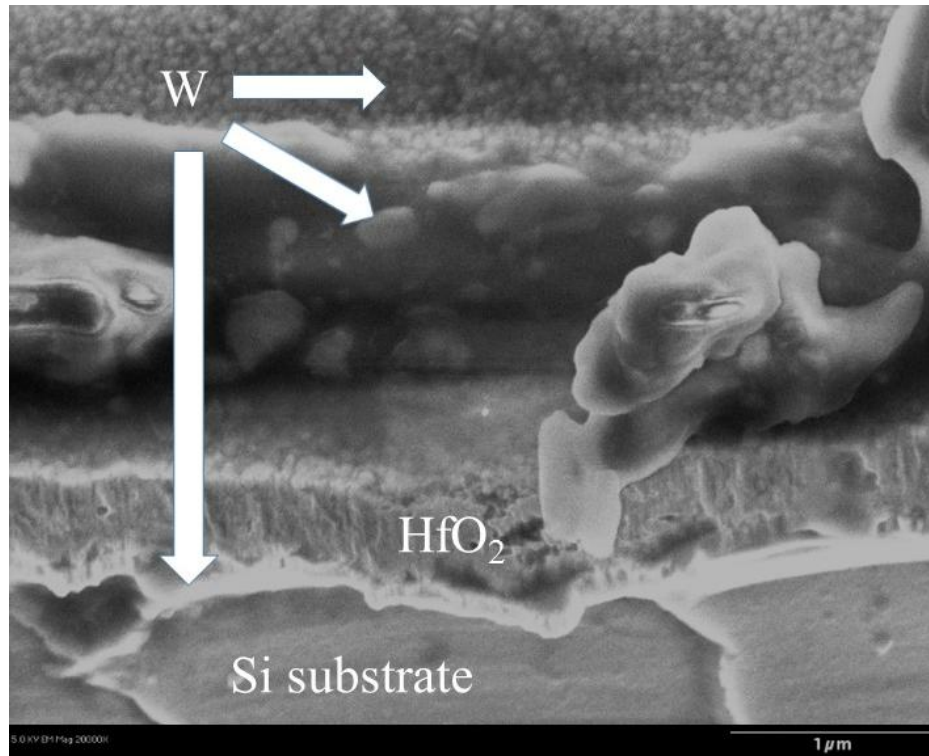


**Figure 37. SEM of a W-HfO<sub>2</sub>-W truncated resonator of dimensions 10-701-145 nm on a silicon substrate after heating to temperatures up to about 550 K. The W and HfO<sub>2</sub> layers were deposited using the Direct Current Magnetron Sputtering (DCMS) technique. The micrograph was taken at 20,000x magnification with 5 kV at 45° from surface normal.**

The surface layer of Sample 1 showed signs of variable thickness of the HfO<sub>2</sub> layer. The change in contrast and texture of the top layer in the SEM and the color rings that are visible are proof of this. It is likely that the breakdown of this structure was due to a combination of the grain structure of HfO<sub>2</sub>, causing the bumps in the surface, and a partial melting of the thin W layer. The W would settle in the crevices between the bumps causing a breakdown of the resonator cavity structure. However, more testing with HfO<sub>2</sub> and thin metal films at elevated temperatures is needed in order to confirm this hypothesis.

## **Sample 2 (Ta-HfO<sub>2</sub>-Ta 9.6-301-169nm)**

### **Fabrication Results.**

The second resonator design was Ta-HfO<sub>2</sub>-Ta and had estimated thicknesses of 9.6-301-169 nm. These thicknesses are close to those which were chosen for this design through the simulation process. These layers were deposited using a DCMS deposition technique. Figure 38 is a scanning electron micrograph (SEM) of the structure at 20,000x magnification. The surface Ta layer displays bumps that are due to the granular structure of HfO<sub>2</sub>. Also, just as in Sample 1, the HfO<sub>2</sub> layer showed signs of non-uniform thickness across the sample. Characteristics such as the color rings moving from the center of the wafer to the edge and the variable thickness seen in Figure 38 are proof of this. However, due to the wavelength range under consideration, 2-20  $\mu\text{m}$ , the grain structure and variable thickness of the middle HfO<sub>2</sub> layer are not going to have a significant impact on the reflectance measurements.

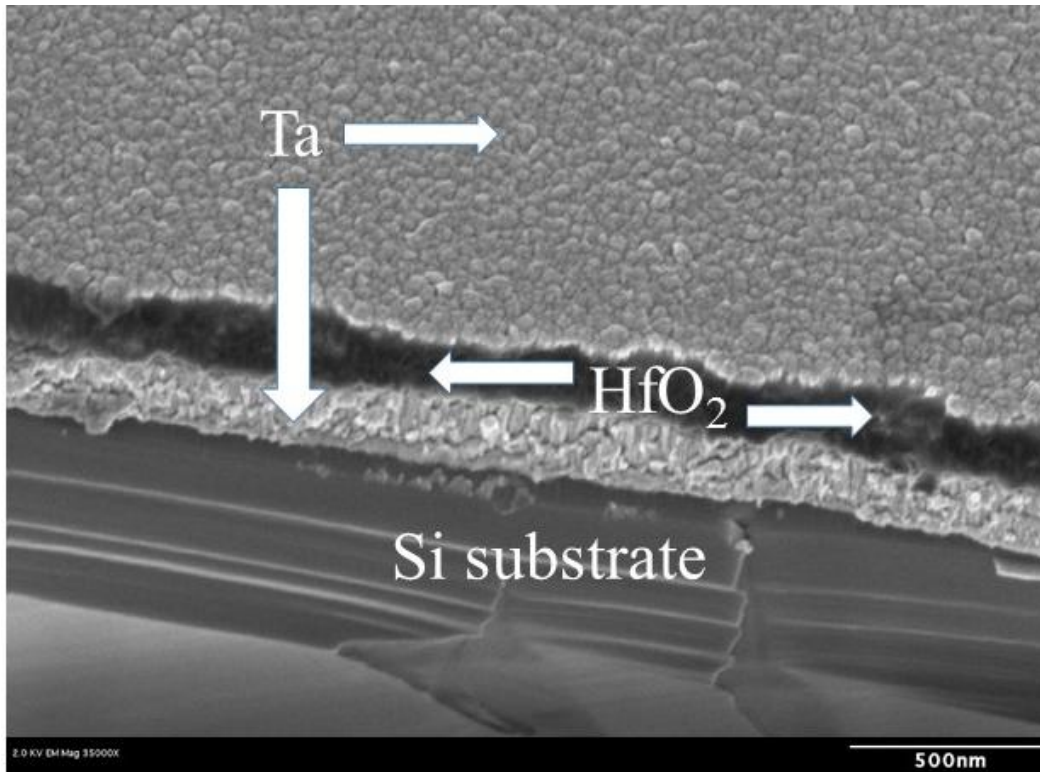


**Figure 38. SEM of a pre-heated Ta-HfO<sub>2</sub>-Ta truncated resonator of dimensions 9.6-301-169 nm on a silicon substrate. The Ta and Ge layers were deposited using the Direct Current Magnetron Sputtering (DCMS) technique. The micrograph was taken at 20,000x magnification with 2 kV at 45° from surface normal.**

### **Reflectance Measurements.**

The emittance data found from the reflectance measurements taken at room temperature using the SOC-100 HDR reflectometer over incident angles of 15°, 25°, 35°, 45°, 55°, 65°, and 75° can be seen in Figure 39. Two absorption peaks centered at 2.91 and 14  $\mu\text{m}$  can be observed. Figure 39 also shows the theoretical emittance values for the designed and fabricated thicknesses in order to make comparisons with the measured values.

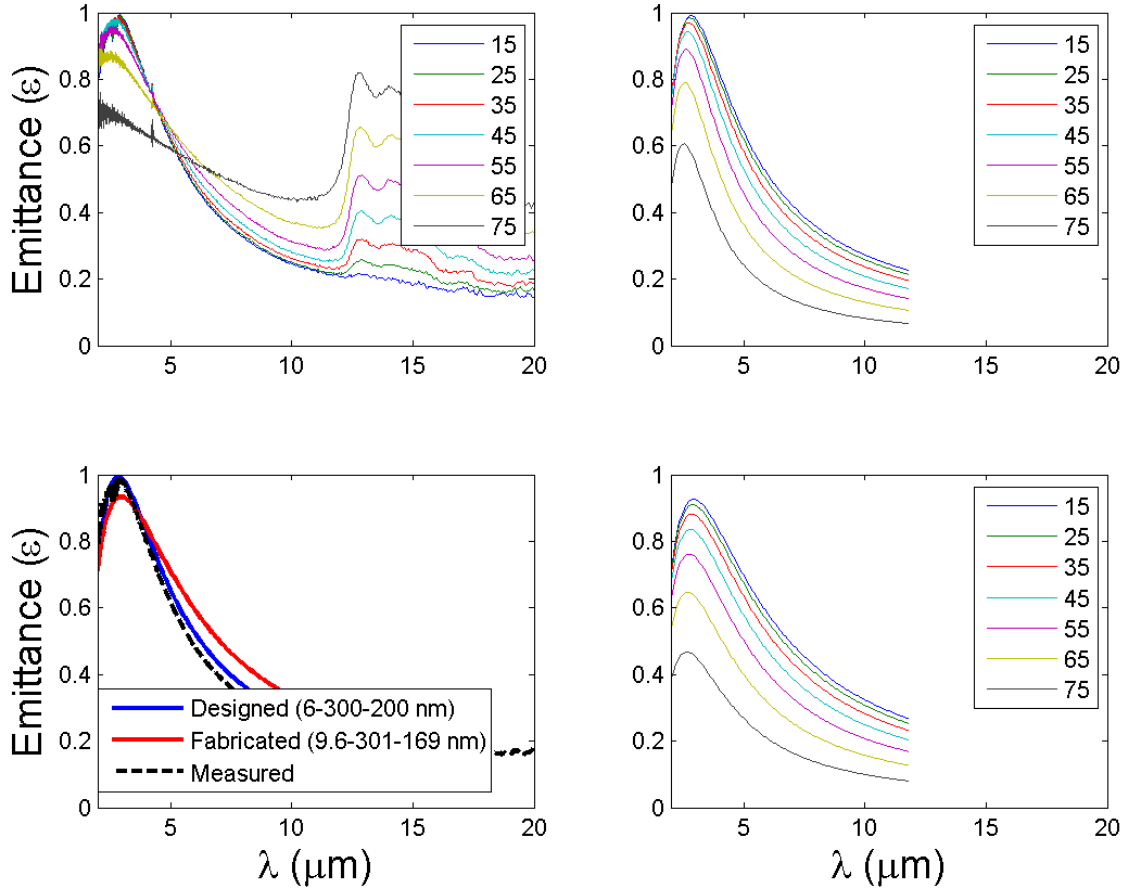


**Figure 39.** Measured (top left) and theoretical emittance values for Ta-HfO<sub>2</sub>-Ta structure with designed thicknesses (6-300-200 nm, top right) and estimated thicknesses after fabrication (9.6-301-169 nm, bottom right) obtained using the enhanced transmission matrix approach with extracted optical constants from ellipsometric models for W (10nm) and HfO<sub>2</sub> (300nm). Emittance values for an incidence angle of 25° for both theoretical models and what was measured are plotted together (bottom left).

The measurements show an absorption feature at 14  $\mu\text{m}$  that shows significant angular dependence, where at angles smaller than 45°, this peak is barely noticeable. This absorption feature is not a result of the truncated resonator but a feature of HfO<sub>2</sub> which was analyzed in Sample 1, Figure 34. Therefore, the only other peak observed for this structure is the first-order peak of the resonator. The spectral location of the measured first-order peak agrees with both of the theoretical emittance plots. However, the

emittance was more accurately characterized in the theoretical emittance values for the designed thicknesses. It can be seen in Figure 39 (bottom left) that the theoretical values from the estimated thicknesses show less emittance. This behavior also points to a thinner top Ta layer than what was estimated, or a top Ta layer closer to 6 nm than 10 nm. Also, it can be seen that the first-order peak does not diminish significantly until the incident angle reaches  $75^\circ$ . This behavior is also seen in the Figure 39 for both cases.

See Figure 40 for six inferred emittance plots for temperatures of 350 K, 400 K, 450 K, 500 K, 550 K, and 600 K. Figure 41 displays the same information, except now each plot is for a different incident angle and each line represents a different temperature at that respective angle.

A 30% to 40% decrease at  $15^\circ$  to  $75^\circ$ , respectively, in the first-order absorption peak can be seen as temperature increases from  $180^\circ\text{C}$  to  $230^\circ\text{C}$ . There were visible signs of change of the surface as the color changed from a silver-white metallic to pink. A post-heat micrograph was taken in order to determine any changes in the resonator, see Figure 42. The contrast from the surface Ta layer to the middle  $\text{HfO}_2$  layer has significantly faded, which indicates that the top layer has changed. Again, more work is needed with  $\text{HfO}_2$  and thin metal layers in order to determine the extent of melting and oxidation of the surface layer, how much of the  $\text{HfO}_2$  layer is visible through the top layer, and any reactions of  $\text{HfO}_2$  with the atmosphere at elevated temperatures.

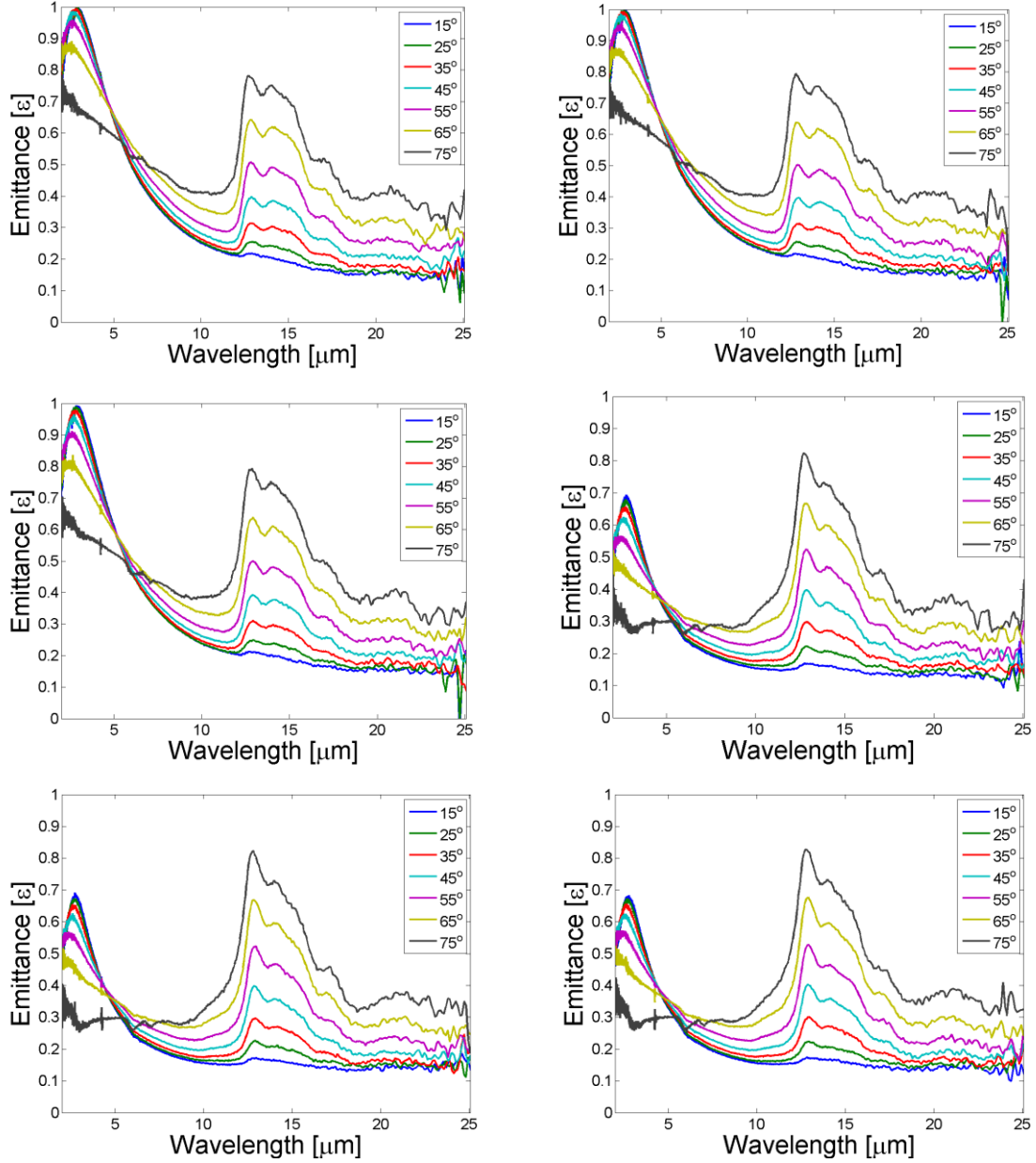


**Figure 40. Inferred angular HDR emittance for p-pol source on a Ta-HfO<sub>2</sub>-Ta structure of dimensions 9.6-301-169 nm at 80°C (top left), 130°C (top right), 180°C (middle left), 230°C (middle right), 280°C (bottom left), and 330°C (bottom right).**

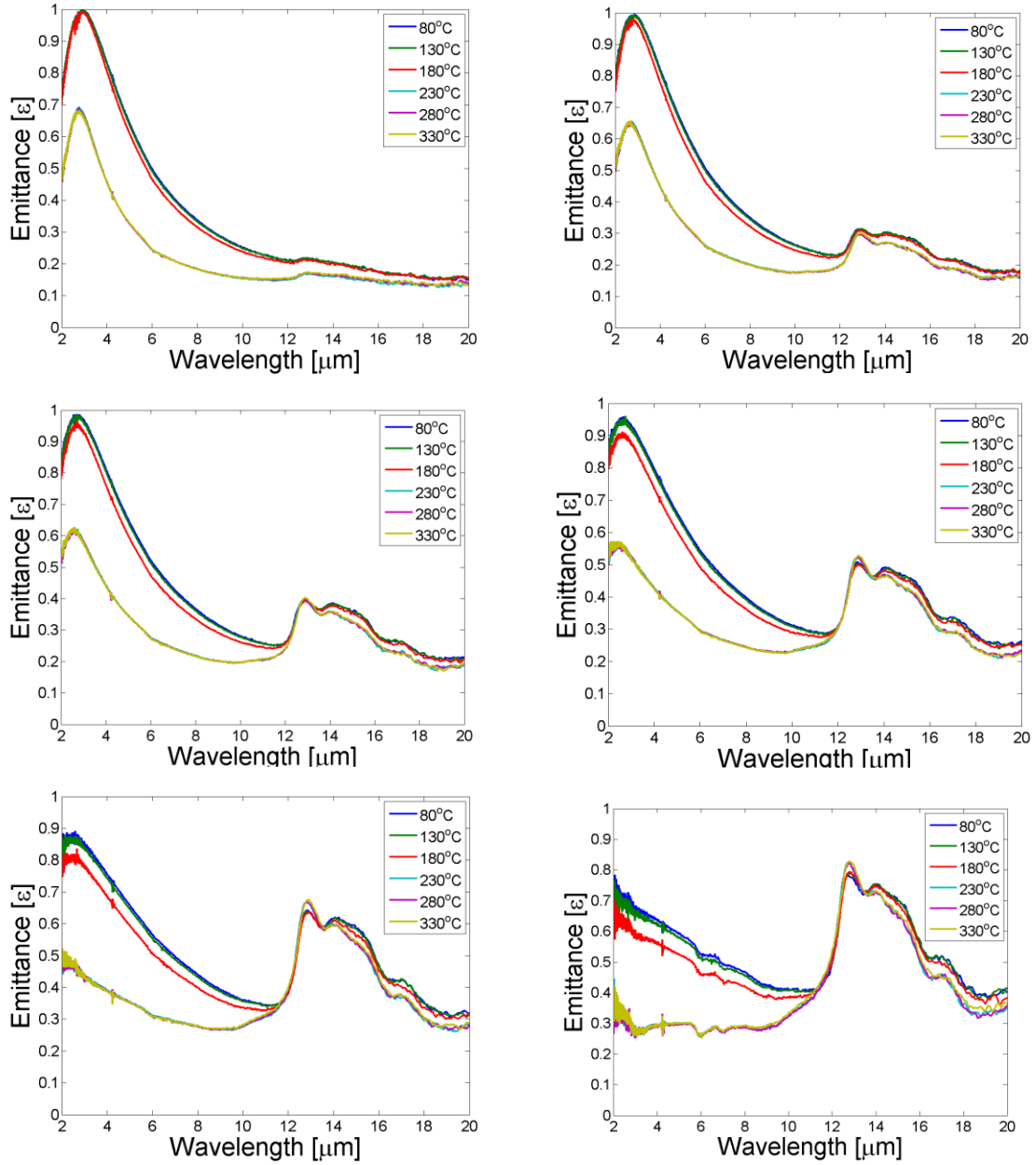


**Figure 41.** Inferred angular HDR emittance for p-pol source on a Ta-HfO<sub>2</sub>-Ta structure of dimensions 9.6-301-169 nm for incident angles 15° (top left), 35° (top right), 45° (middle left), 55° (middle right), 65° (bottom left), 75° (bottom right) at temperatures 80°C, 130°C, 180°C, 230°C, 280°C, and 330°C.



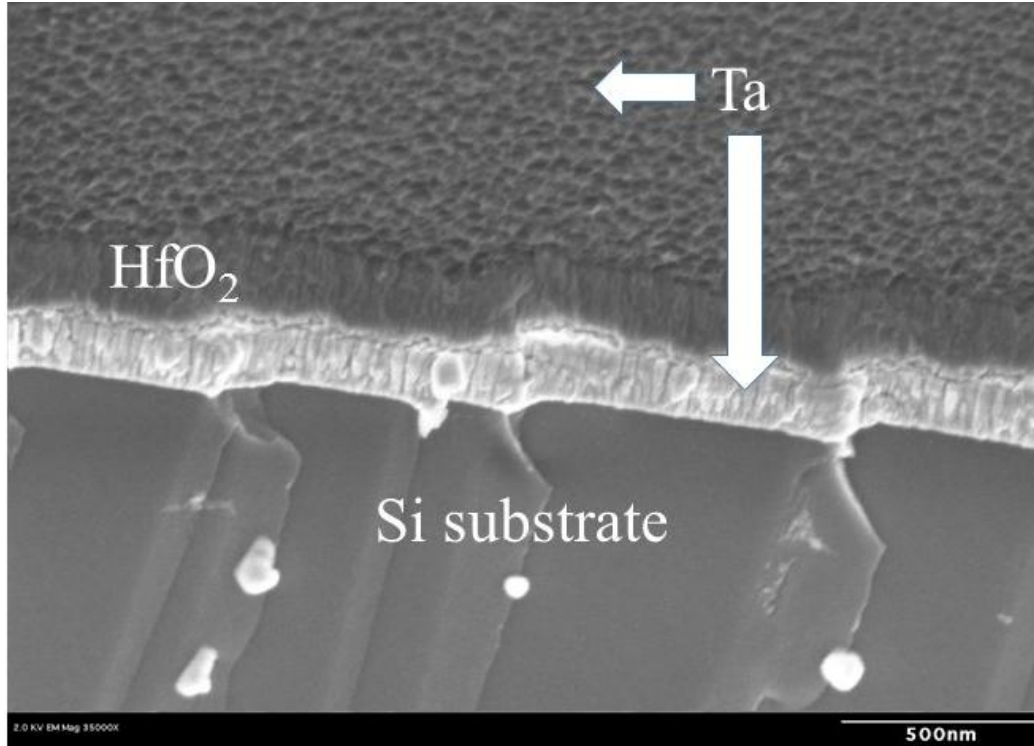


**Figure 42.** SEM of a Ta-HfO<sub>2</sub>-Ta truncated resonator of dimensions 9.6-301-169 nm on a silicon substrate after heating to temperatures up to about 600 K. The Ta and Ge layers were deposited using the Direct Current Magnetron Sputtering (DCMS) technique. The micrograph was taken at 35,000x magnification with 2 kV at 45° from surface normal.

### **Sample 3 (W-Ge-W 10-760-145nm)**

#### **Fabrication Results.**

The third and fourth resonator designs moved away from using HfO<sub>2</sub> to a more well-known dielectric, Ge. The estimated thicknesses for the W-Ge-W design were 10-760-145 nm. The deposited Ge layer is further from the theoretical design than the HfO<sub>2</sub> layers. Therefore, it should be expected that the emissive peaks for the Ge structures will be at longer wavelengths than the simulated design for W-Ge-W 10-700-160 nm.

Figure 43 is an SEM of the structure at 20,000x magnification. It can be seen from this micrograph that the top W layer is much smoother than for the HfO<sub>2</sub> structures.

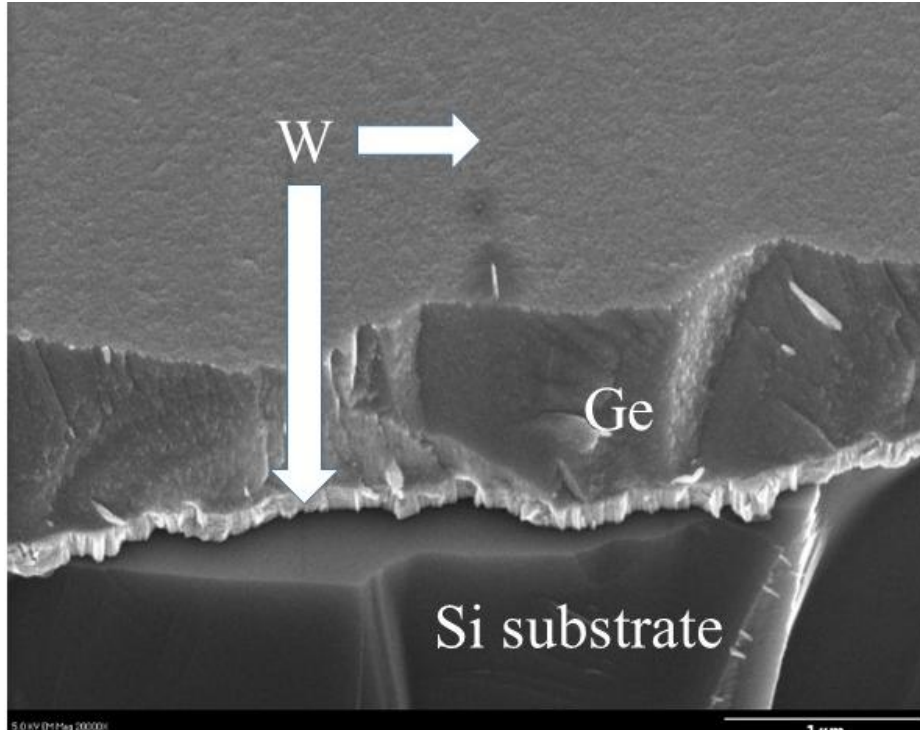


**Figure 43. SEM of a pre-heated W-Ge-W truncated resonator of dimensions 10-760-145 nm on a silicon substrate. The W and Ge layers were deposited using the Direct Current Magnetron Sputtering (DCMS) technique. The micrograph was taken at 20,000x magnification with 5 kV at 45° from surface normal.**

#### **Reflectance Measurements.**

Again, reflectance measurements were taken using AFIT's SOC-100 HDR reflectometer. These reflectance measurements were taken for incident angles of 15°, 25°, 35°, 45°, 55°, 65°, and 75°. Figure 44 (top left) shows the inferred emittance from the measured HDR reflectance made with the SOC-100 for wavelengths of 2-20  $\mu\text{m}$  at room temperature. Again, the theoretical emittance plot, Figure 44 (top right), is displayed below in order to make comparisons to the measurements.

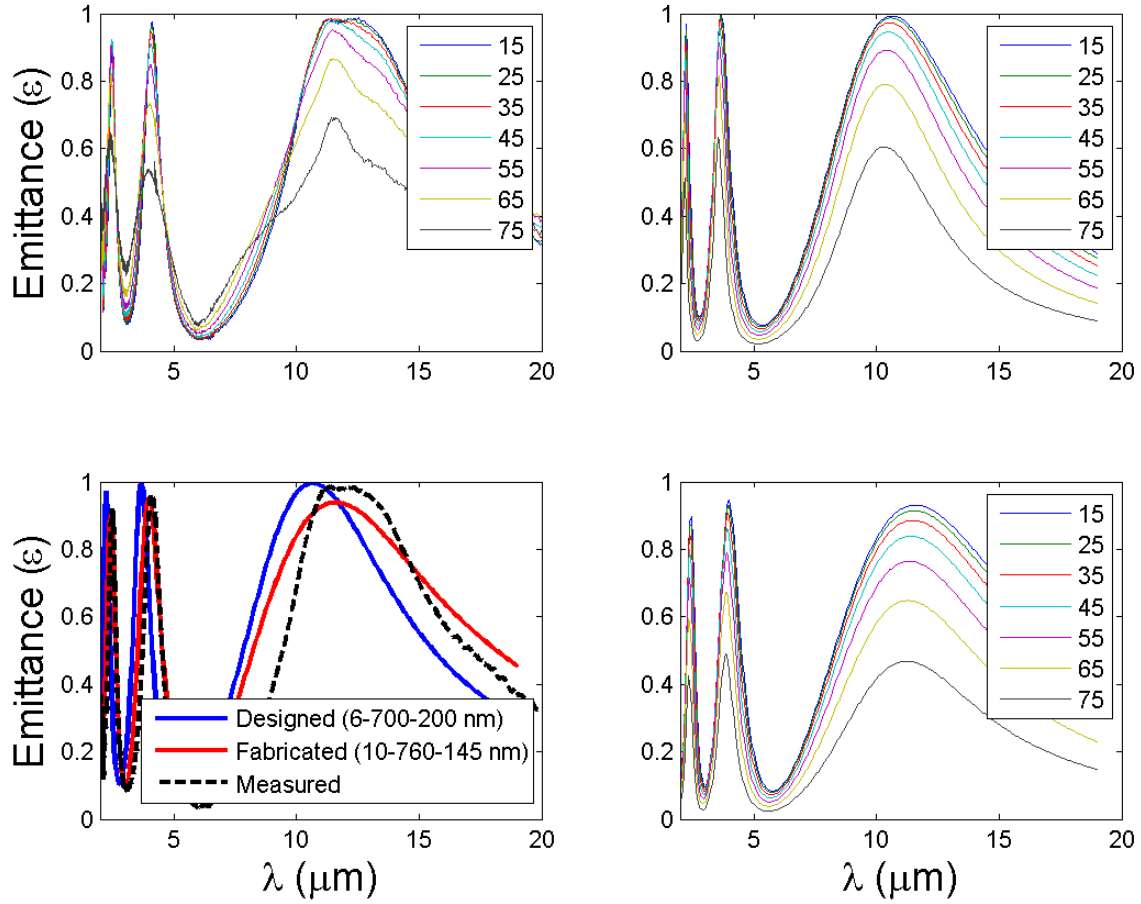


**Figure 44.** Measured (top left) and theoretical emittance values for W-Ge-W structure with designed thicknesses (6-700-200 nm, top right) and estimated thicknesses after fabrication (10-760-145 nm, bottom right) obtained using the enhanced transmission matrix approach with extracted optical constants from ellipsometric models for W (10nm) and Ge (300nm). Emittance values for an incidence angle of  $25^\circ$  for both theoretical models and what was measured are plotted together (bottom left).

Three emittance bands centered at approximately  $2.51 \mu\text{m}$ ,  $4.12 \mu\text{m}$ , and  $12.53 \mu\text{m}$  are clearly visible in the measurements. It can be seen that the emittance peaks from the measurements do not diminish until the angle of incidence becomes greater than  $55^\circ$ .

There is a difference in emittance and spectral location of the peaks for the two theoretical plots for the different thickness (designed, fabricated) of the resonator. The

theoretical values for the estimated thicknesses (10-760-200 nm) were more accurate in predicting the spectral location of the emittance peaks at 2.51  $\mu\text{m}$ , 4.12  $\mu\text{m}$ , and 12.53  $\mu\text{m}$ , but the first-order peak was 10% less than what was measured. This indicates that the actual fabricated thickness for the top W layer is closer to 6 nm than the estimated 10 nm.

Next, a heat test was performed on this structure. Reflectance measurements were taken at temperatures from approximately 300 K (30 °C) to 600 K (330 °C) in 50-K increments. Figure 45 displays six emittance plots for temperatures of about 350 K, 400 K, 450 K, 500 K, 550 K, and 600 K. Figure 46 displays the same information in a different form in order to make any trends easier to see.

Two observations can be made from this data. First, there are no significant changes in the spectral location in the absorption peaks, but there is some angular dependence as temperature increases. Second, a 10% to 15% drop of the first order emittance peak, located at 12.53  $\mu\text{m}$ , from 15° to 75° can be seen from the measurement at 180 °C to that performed at 230 °C, which is more clearly seen in Figure 46. Even though the first-order peak is of more interest, a 45% and 30% decrease in emittance at the second- and third-order peaks, at 4.12  $\mu\text{m}$  and 2.51  $\mu\text{m}$ , can be seen from 180 °C to 230 °C.

After heat testing, the top W layer showed a noticeable change in color from a silver-white metallic color before heat testing began to yellow color after heat testing. The most common oxidation state of W is  $\text{WO}_3$  which has a yellow coloring [83]. Therefore, this color change points to significant oxidation of the W layer. Another SEM was taken to help identify any changes in the structure, see Figure 47.

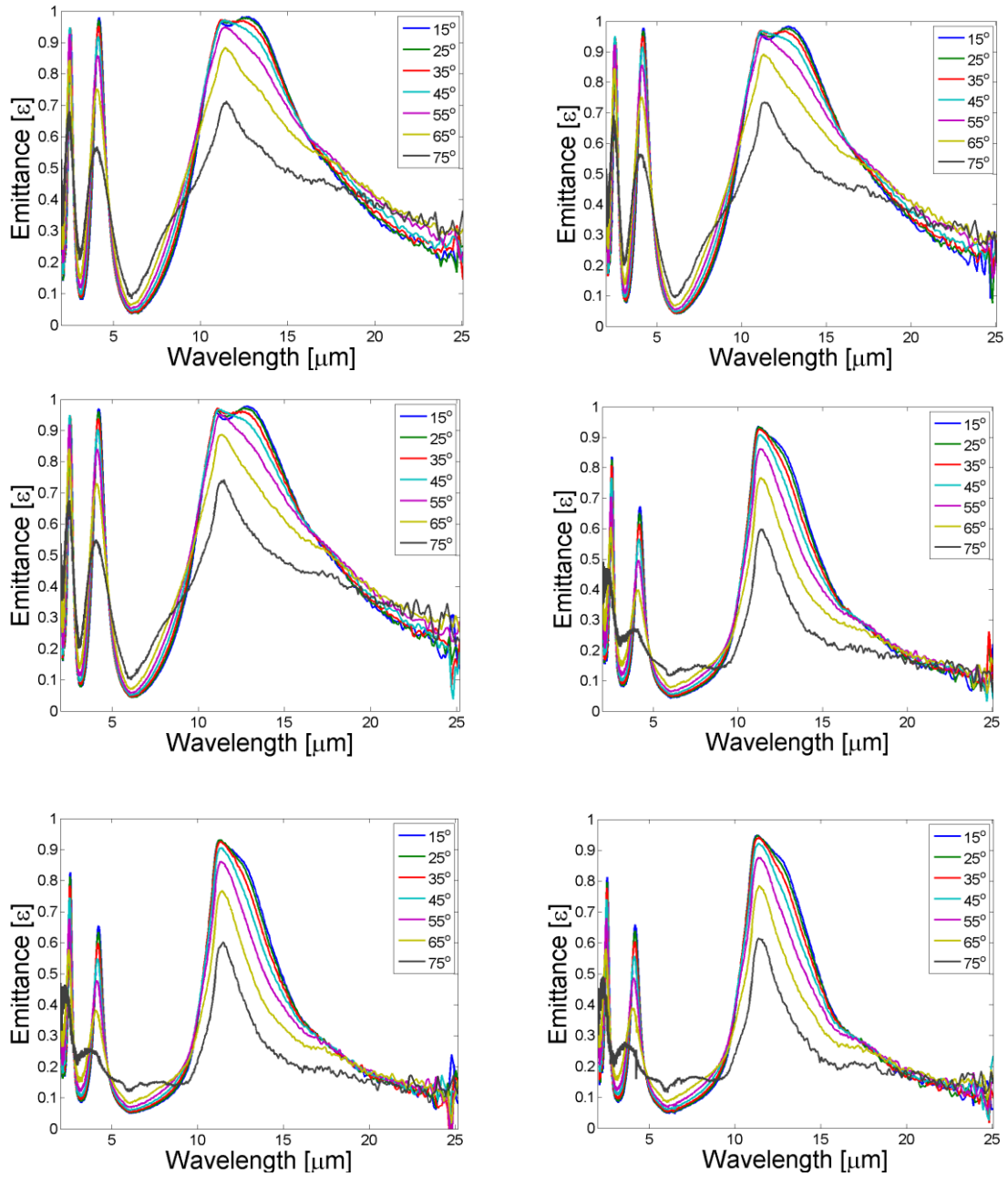


**Figure 45. Inferred angular HDR emittance for p-pol source on a W-Ge-W structure of dimensions 10-760-145 nm at 80°C (top left), 130°C (top right), 180°C (middle left), 230°C (middle right), 280°C (bottom left), and 330°C (bottom right).**

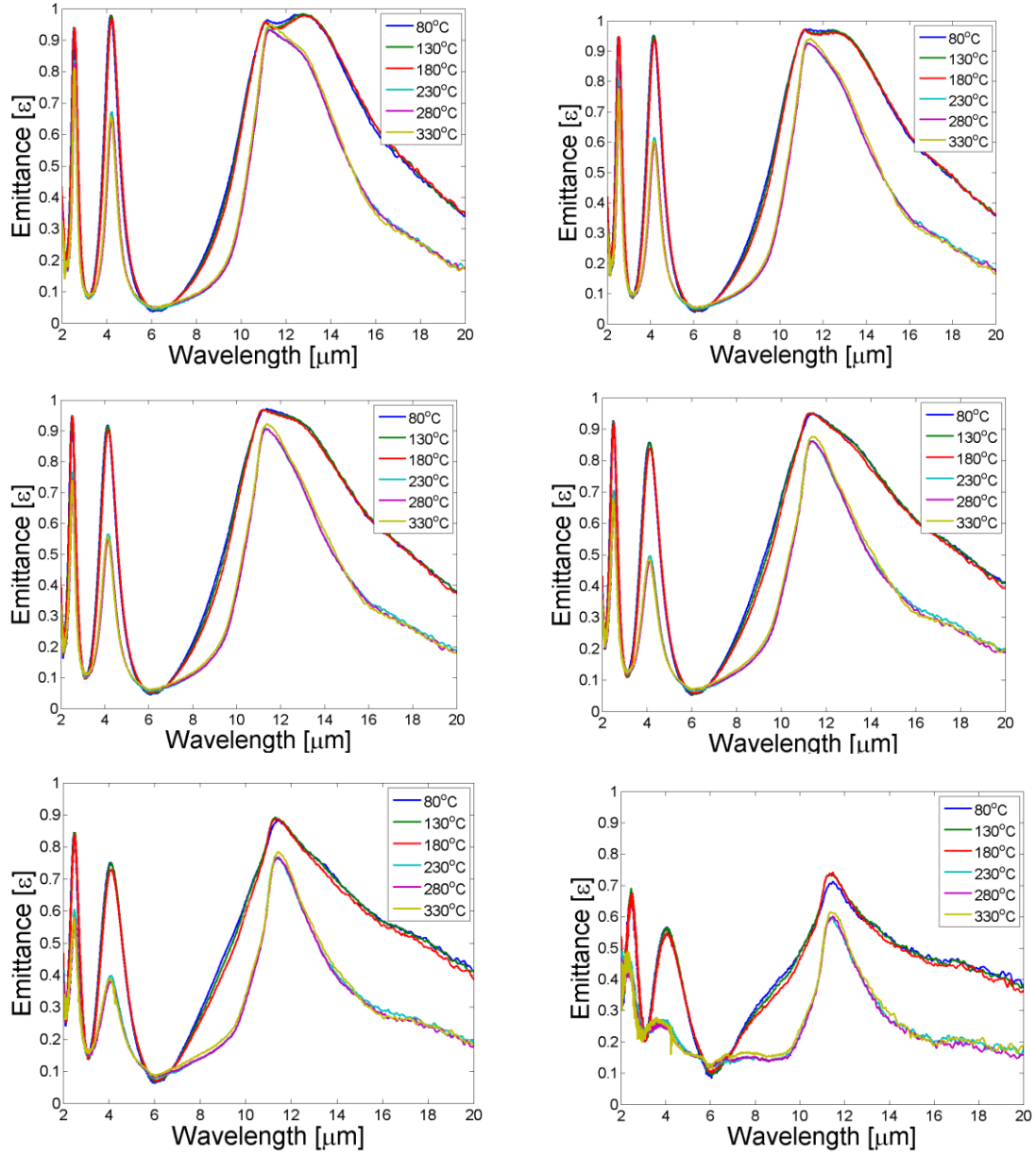


**Figure 46. Inferred angular HDR emittance for p-pol source on a W-Ge-W structure of dimensions 10-760-145 nm for incident angles 15° (top left), 35° (top right), 45° (middle left), 55° (middle right), 65° (bottom left), 75° (bottom right) at temperatures 80°C, 130°C, 180°C, 230°C, 280°C, and 330°C.**

Making a comparison of Figure 47 to Figure 43, the SEM taken before heat testing began, the surface layer of W and the Ge layer show some significant differences. These pictures point to a change in the surface layer as evidenced by the contrast between the W layer and the Ge layer in Figure 47 which was not present in Figure 43. Also, there are particles in the Ge layer which can be seen in the post-heat testing SEM (Figure 47) which were not observed in Figure 43. This is a sign of grain growth in the Ge layer.

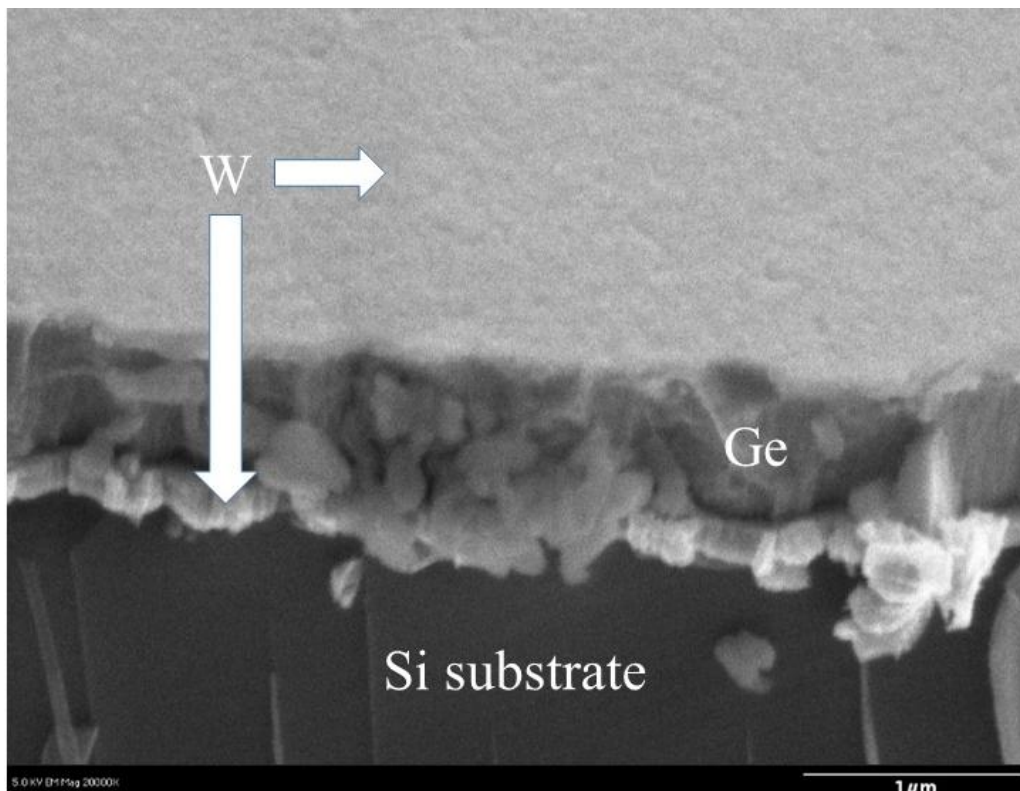


**Figure 47.** SEM of a W-Ge-W truncated resonator of dimensions 10-760-145 nm on a silicon substrate after heating to temperatures up to about 600 K. The W and Ge layers were deposited using the Direct Current Magnetron Sputtering (DCMS) technique. The micrograph was taken at 20,000x magnification with 5 kV at 45° from surface normal.



#### Sample 4 (Ta-Ge-Ta 9.6-728-169nm)

##### Fabrication Results.

The last resonator design had a structure of Ta-Ge-Ta and estimated thicknesses of 9.6-728-169 nm. A thickness of 130-200 nm for the bottom Ta layer was targeted to ensure that this layer was opaque. These thicknesses are close to those which were determined from the theoretical simulations which were 6-700-160 nm, respectively. These layers were deposited using a DCMS deposition technique. An SEM of Sample 4 looking down at 45° from surface normal at 35,000x magnification is shown in Figure 48.

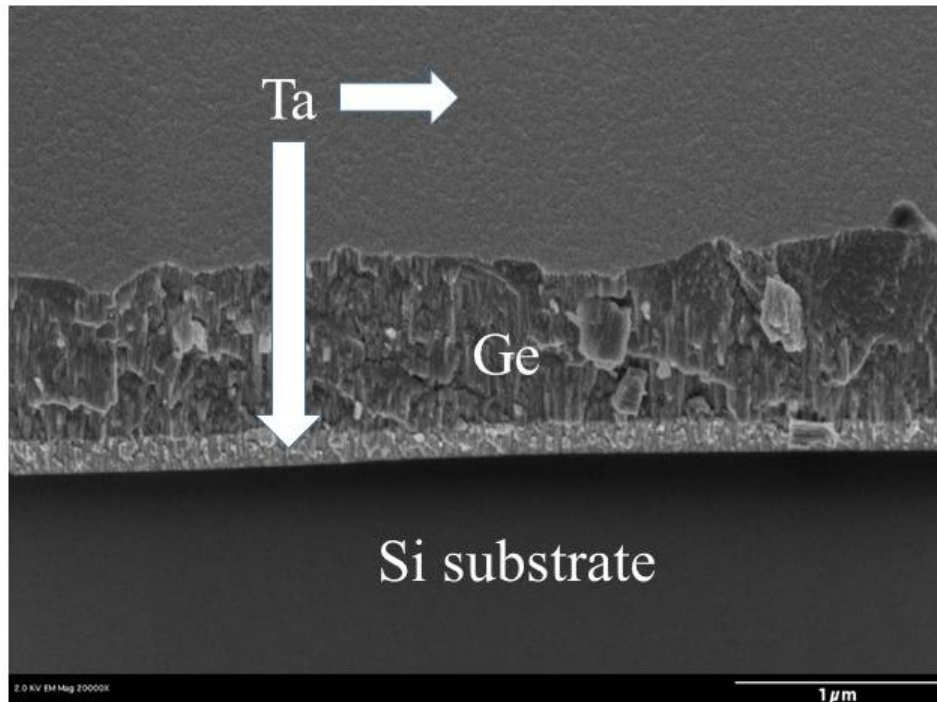


**Figure 48.** SEM of a pre-heated Ta-Ge-Ta truncated resonator of dimensions 9.6-728-169 nm on a silicon substrate. The Ta and Ge layers were deposited using the Direct Current Magnetron Sputtering (DCMS) technique. The micrograph was taken at 35,000x magnification with 2 kV at 45° from surface normal.



From Figure 48, it can be seen that the surface is smooth and the thicknesses of the middle Ge layer and bottom Ta layer are uniform. Also, the middle Ge layer shows signs of fracturing due to inherent compressive stress.

### **Reflectance Measurements.**

The emittance data found from the reflectance measurements taken at room temperature using the SOC-100 HDR reflectometer over incident angles of 15°, 25°, 35°, 45°, 55°, 65°, and 75° can be seen in Figure 49 (top left). Three absorption peaks centered at 2.51, 4.23, and 14  $\mu\text{m}$  can be identified. The theoretical emittance plot was shown in Figure 31 and repeated here in Figure 49 (top right) along with the theoretical values found for the estimated thicknesses after fabrication.

The absorption features of this structure are angle-independent, that is, these absorption peaks do not diminish as the incident angle increases, at least not as much as what the theoretical values predicted. From the measurements, the first-order peak centered at 14  $\mu\text{m}$  is broad, 10-18  $\mu\text{m}$ , and the second order peak, at 4.23  $\mu\text{m}$ , is much narrower. The emittance peaks in both of the theoretical plots are located at shorter wavelengths than what is seen from the measurements. This indicates that the fabricated thickness is slightly larger than the estimated 728 nm. Again, this structure's reflectance properties were measured at temperatures greater than room temperature from 350 K (80 °C) to 600 K (330 °C). See Figure 54 for six inferred emittance plots for temperatures of 350 K, 400 K, 450 K, 500 K, 550 K, and 600 K.

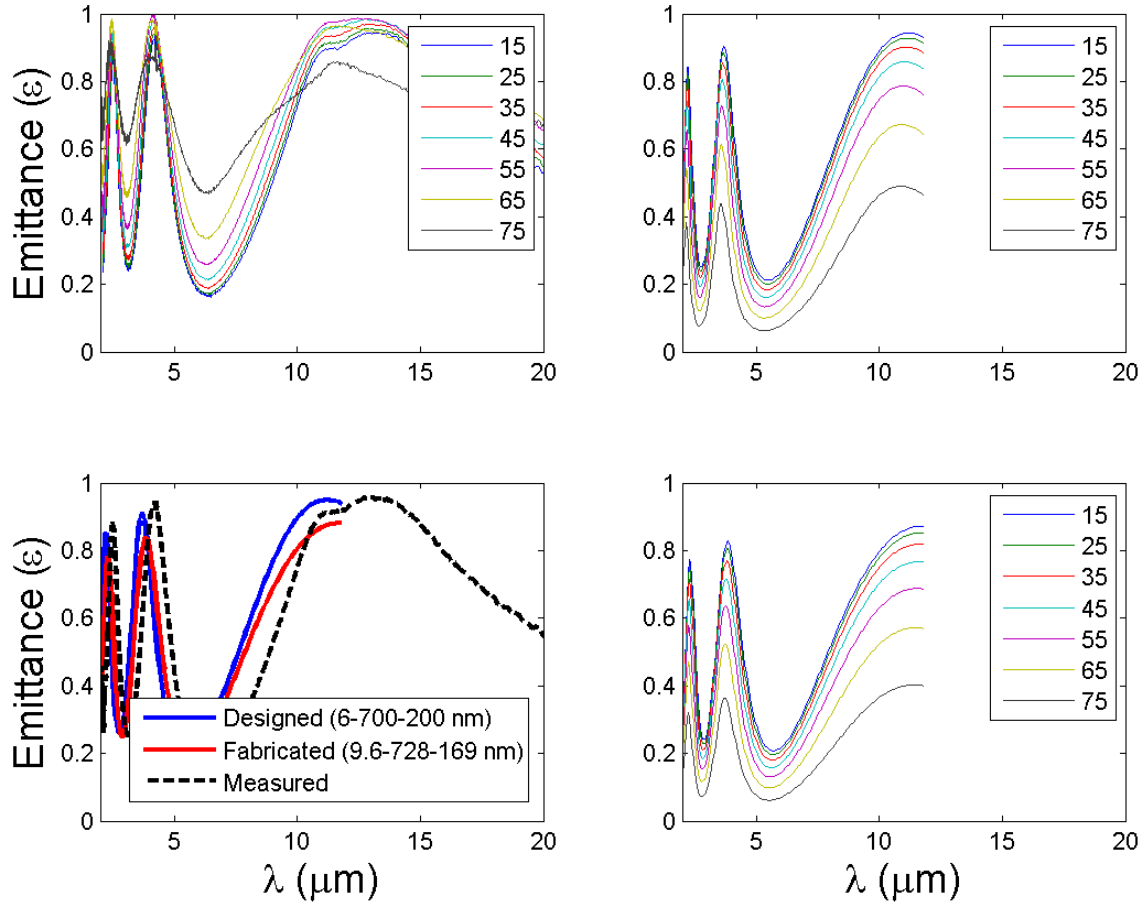


**Figure 49.** Measured (top left) and theoretical emittance values for Ta-Ge-Ta structure with designed thicknesses (6-700-200 nm, top right) and estimated thicknesses after fabrication (9.6-728-16 nm, bottom right) obtained using the enhanced transmission matrix approach with extracted optical constants from ellipsometric models for Ta (10nm) and Ge (300nm). Emittance values for an incidence angle of  $25^\circ$  for both theoretical models and what was measured are plotted together (bottom left).

A 10% decrease in emittance is noticeable for incident angles smaller than  $55^\circ$ . At higher incident angles, a 20% decrease in all three absorption peaks can be seen as temperature increases. This is more noticeable for the broadest peak centered at  $14 \mu\text{m}$ , See Figure 50. Therefore, at higher temperatures, the absorption features of Sample 4 do experience angular dependence. Between the temperatures of  $230^\circ\text{C}$  and  $280^\circ\text{C}$ , a 5% to

10% decrease in the first order emittance peak, located at  $14\text{ }\mu\text{m}$ , can be seen for incident angles of  $15^\circ$  to  $55^\circ$ . For incident angles of  $65^\circ$  to  $75^\circ$ , a 20% decrease is seen. These trends are easier to see in Figure 51.

As temperature increases, the absorption of the structure increases. The lowest absorption feature at  $6.5\text{ }\mu\text{m}$  is approximately 0.2 at  $80^\circ\text{C}$  and increases to approximately 0.4 at  $330^\circ\text{C}$ . As temperature increases, Ge experiences thermal run-away and its absorption increases [56]. However, a deeper study of the effects of temperature on Ta and Ge will need to be conducted in order to pin-point the cause.

A post-heat micrograph was taken in order to determine if any changes in the resonator have occurred, see Figure 52. No significant deterioration is evident. Some grain growth is evident in the Ge layer. The top Ta layer remained intact which is proof of the resonator retaining its absorption peaks at the higher temperatures.

## Summary

This chapter discussed the design, fabrication, and measurement of four multilayer resonators and the characterization of thin metal films. A theoretical dimensional analysis was conducted in order to observe the effects which the top metal and middle dielectric layers of the resonator had on the absorption features of the structure. The resonators were fabricated using a DCMS system and measured using the SOC-100 HDR reflectometer. Spectroscopic ellipsometry was used to gain insight of the optical properties of thin metal films, how they differ from bulk material properties, and how they affect the design of the resonators.

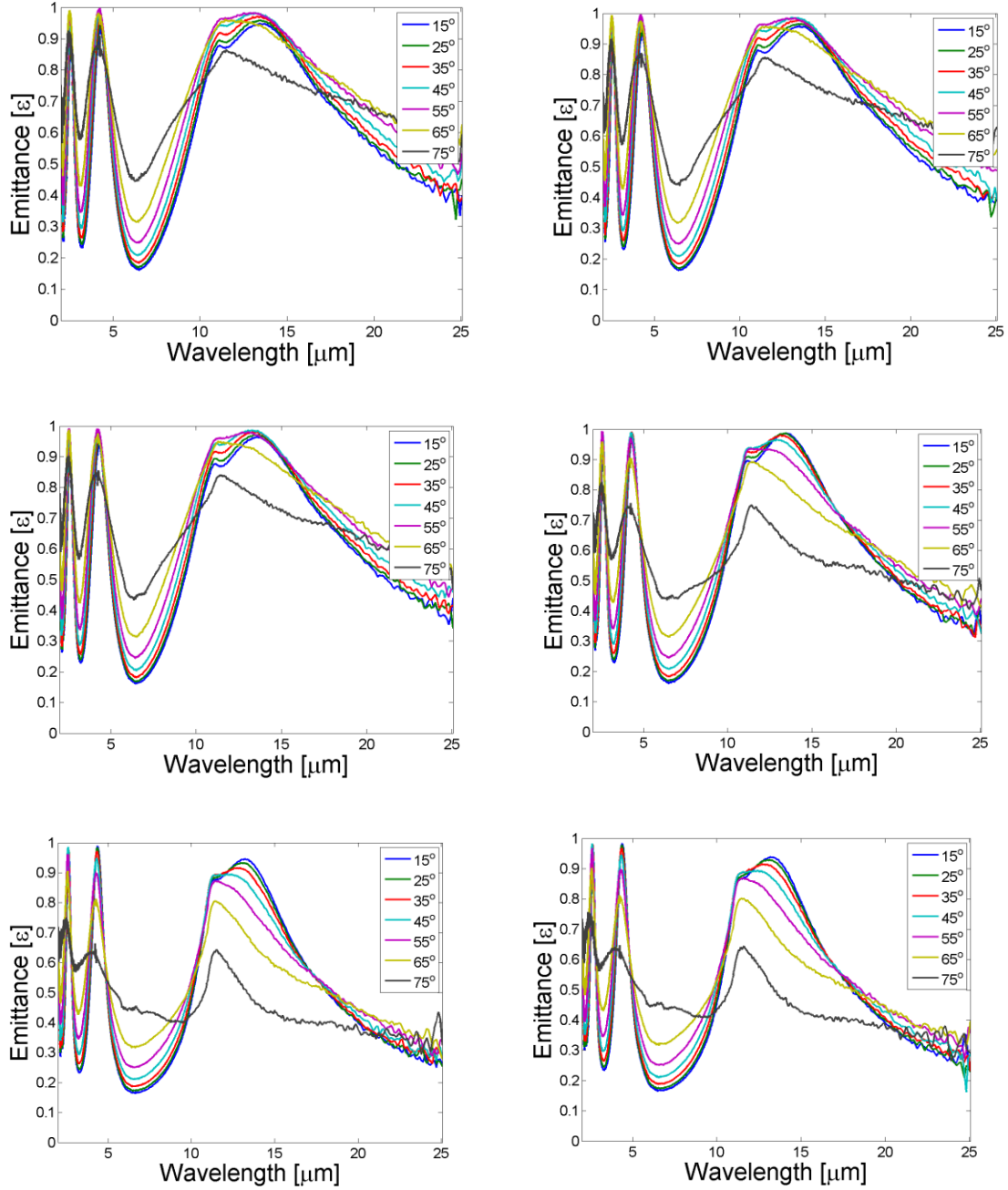


**Figure 50. Inferred angular HDR emittance for p-pol source on a Ta-Ge-Ta structure of dimensions 9.6-728-169 nm at 80°C (top left), 130°C (top right), 180°C (middle left), 230°C (middle right), 280°C (bottom left), and 330°C (bottom right).**

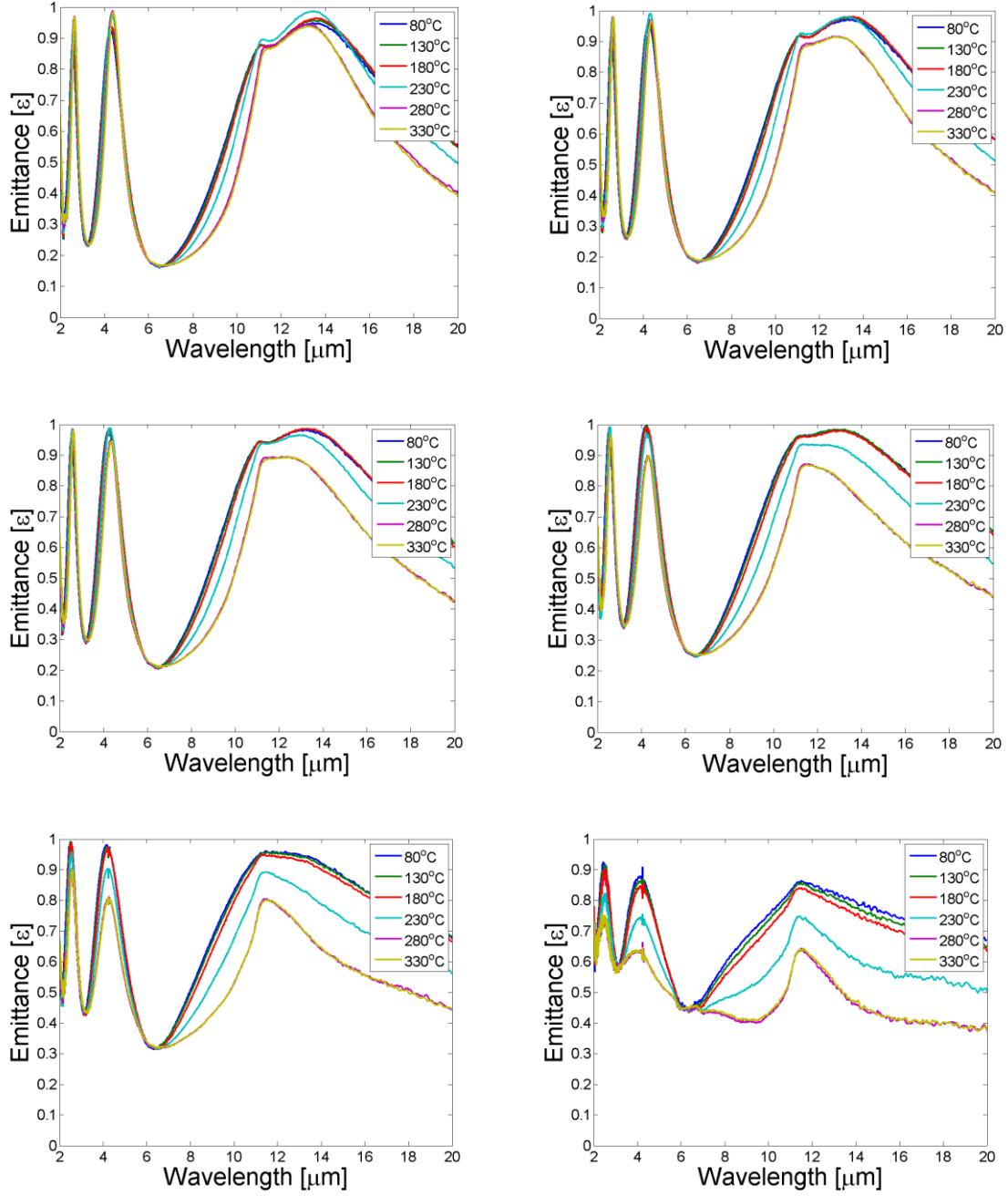


**Figure 51. Inferred angular HDR emittance for p-pol source on a Ta-Ge-Ta structure of dimensions 9.6-728-169 nm for incident angles 15° (top left), 35° (top right), 45° (middle left), 55° (middle right), 65° (bottom left), 75° (bottom right) at temperatures 80°C, 130°C, 180°C, 230°C, 280°C, and 330°C.**

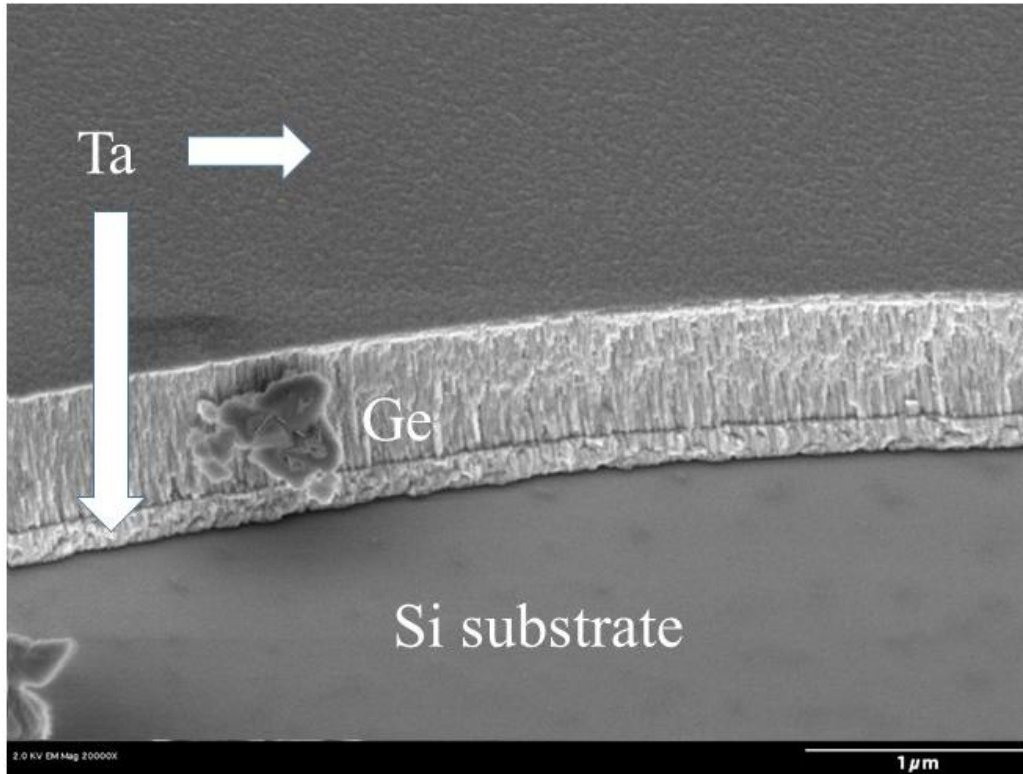


**Figure 52.** SEM of a Ta-Ge-Ta truncated resonator of dimensions 9.6-728-169 nm on a silicon substrate after heating to temperatures up to about 600 K. The Ta and Ge layers were deposited using the Direct Current Magnetron Sputtering (DCMS) technique. The micrograph was taken at 20,000x magnification with 2 kV at 45° from surface normal.

## **V. Conclusions**

### **Conclusions of Research**

In this thesis, four variations of a thermal emitter design were proposed using Lumerical's FDTD Solutions software package. Spectroscopic ellipsometry was used to derive optical constants of the DCMS-deposited thin material layers. These constants were compared to bulk material values from literature, and using the enhanced transmittance matrix approach, they were used to re-calculate the reflectance values for each design. The DCMS technique was also used to deposit nano-layers of Ge, HfO<sub>2</sub>, W, and Ta to build various tri-layer structures. Angular sensitivities to incident p-pol IR radiation were investigated for each structure. Emittance was derived from the reflectance measurements made using the SOC-100 HDR reflectometer and taken from 2-20  $\mu\text{m}$  at various temperatures up to 600 K.

The original intent of this research was to investigate and design a thermally stable structure that could coherently affect the thermal radiative properties of a surface, both spectrally and directionally, through the use of nano-structured materials. However, as the research effort progressed, it became apparent that the design and fabrication of engineered structures is not as clear-cut as the designer may expect it to be. Surface quality, purity, overlayers, and microstructure will all affect the optical properties of deposited materials. The DCMS deposition technique was chosen to deposit the conductive materials in order to minimize the effects of an amorphous microstructure and

surface roughness. While these parameters were reduced, flaws in the microstructure and surface still occurred. The material properties used in the design phase were found through the process of ellipsometry and modeling using the IR-VASE. These constants were used in order to produce more accurate theoretical predictions than what bulk material parameters had yielded. Ultimately, to accurately predict the performance of a thermal emitter, bulk optical properties cannot be assumed for thin layers of material and the deposition method will have an effect on the microstructure and optical properties of the material. Also, the accuracy of the theoretical values using the extracted optical constants from the thin layers depends of the accuracy of the ellipsometric model. More information that is known about the material allows the user to better fit oscillator models to the ellipsometric measurements. Therefore, the ellipsometric modeling is more challenging for materials like  $\text{HfO}_2$ , where little information was found about its optical properties in literature. The optical properties of the thin layer of  $\text{HfO}_2$  (300 nm) were extracted via ellipsometry and plotted, see Figure 27.

All of the designs achieved spectral coherence and demonstrated angle-dependence, but when thermal testing was conducted, two designs held up much better than the rest. The W- $\text{HfO}_2$ -W (10-701-145 nm) and Ta- $\text{HfO}_2$ -Ta (9.6-301-169 nm) experienced a 70% and 30% decrease, respectively, in emittance at temperatures greater than 280 °C, while W-Ge-W (10-760-145 nm) and Ta-Ge-Ta (9.6-728-169 nm) showed 10% and 5% decrease, respectively. The Ta-Ge-Ta structure was the most promising, showing the smallest drop in emittance at elevated temperatures and the least amount of property/structural changes. This design, Ta-Ge-Ta (9.6-728-169 nm) also emits almost all of its radiation in the atmospheric passbands of 1-5  $\mu\text{m}$  and 8-14  $\mu\text{m}$ , see Figure 53. It



is because of the broad nature of these peaks that not all radiation was emitted in the passbands. If all radiation emitted from a structure is desired to be in a transmission or absorption band, than narrower peaks are necessary. For this case, other nano-structure designs, possibly a 2-D or 3-D PC, should be considered in order to achieve narrower spectral bands and/or greater angle-dependence of the emitted radiation.

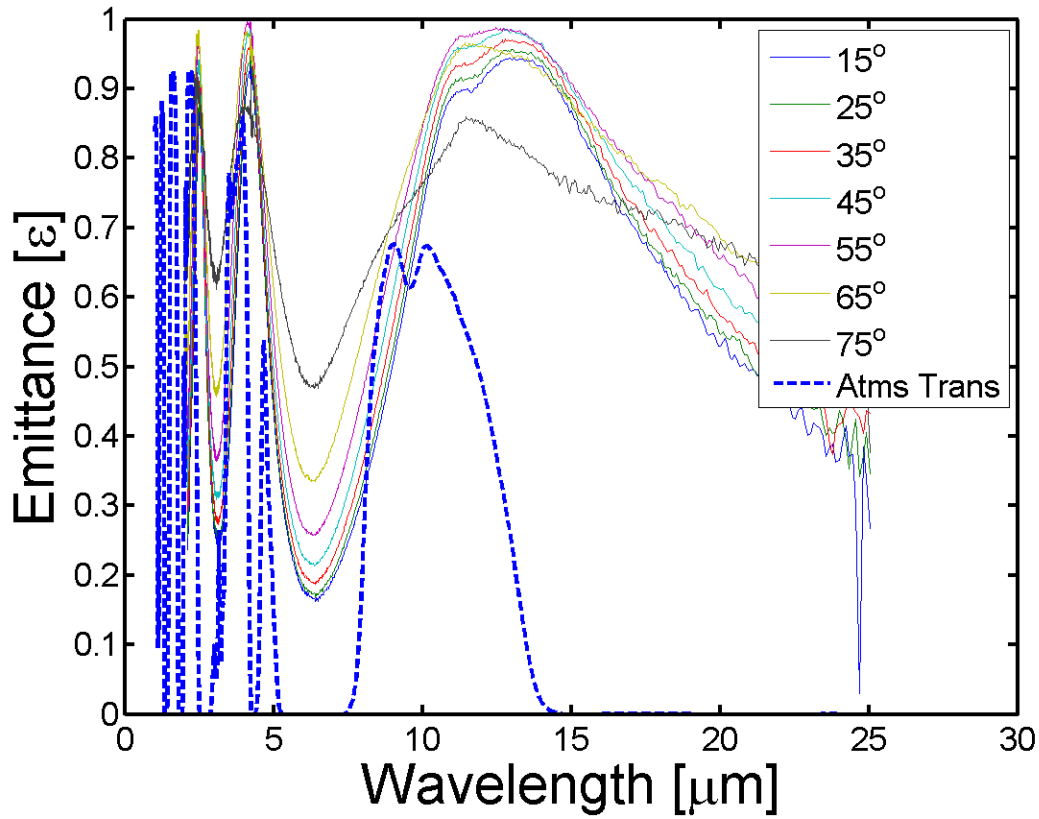


**Figure 53. Inferred angular HDR emittance for p-pol source on a Ta-Ge-Ta structure of dimensions 9.6-728-169 nm at room temperature plotted with atmospheric transmittance (dotted line).**

## Recommendations for Future Research

For structures that are expected to operate in environments at elevated temperatures or when dealing with thin layers ( $\sim 10$  nm) of various deposition techniques, it is recommended that their optical constants be determined at the expected operating temperature(s) first. This is especially useful when the optical properties of the material(s) are not well defined in literature at room temperature or expected elevated operating temperature(s). This can be accomplished by using the IR-VASE with an optional heating sample stage attachment called HTC-100 Heated Sample Stage. Using this attachment, it is possible to make measurements at temperatures ranging from room temperature up to 573 K. Prioritizing finding the actual material properties of the deposited materials will make the theoretical designs more accurate compared to the measured values. Also, extracting optical properties at elevated temperatures will allow for theoretical predictions and designs for thermally stable structures.

This work focused on the use of materials whose properties were not well known or not well defined at higher temperatures (*e.g.*,  $\text{HfO}_2$ , Ta). From a material analysis perspective, the next step should be to make ellipsometric measurements and extract the complex refractive index values for each material at increment temperatures. The recommended step on the design of the structure is to try a tri-layer resonator which utilizes an extra-ordinary transmission layer as the surface layer. This design would have the same structure as the multilayer resonators, namely a dielectric layer sandwiched between two metal layers, but the top metal layer would be optically thick with a hole-

pattern array designed to allow a certain wavelength to extraordinarily transmit into the resonator, See Figure 54. Determining the wavelength that is able to transmit through the structure comes from the following conservation of momentum equation:

$$\vec{k}_{spp} = \vec{k}_x \pm i\vec{G}_x \pm j\vec{G}_y, \quad (46)$$

where  $\vec{k}_{spp}$  is the surface-plasmon polariton (SPP) wave vector,  $\vec{k}_x = |\vec{k}_0|\sin(\theta)$  is the component wave vector of the incident radiation in-plane with the surface,  $|\vec{k}_0| = 2\pi/\lambda$  is the propagation constant,  $\theta$  is the incident angle,  $\vec{G}_x$  and  $\vec{G}_y$  are grating lattice vectors,  $|\vec{G}_x| = |\vec{G}_y| = 2\pi/\Lambda$ , and  $i, j$  are integers. Therefore, the transmitted wavelength is a function of the incident angle ( $\theta$ ) and the periodicity of the holes ( $\Lambda$ ).

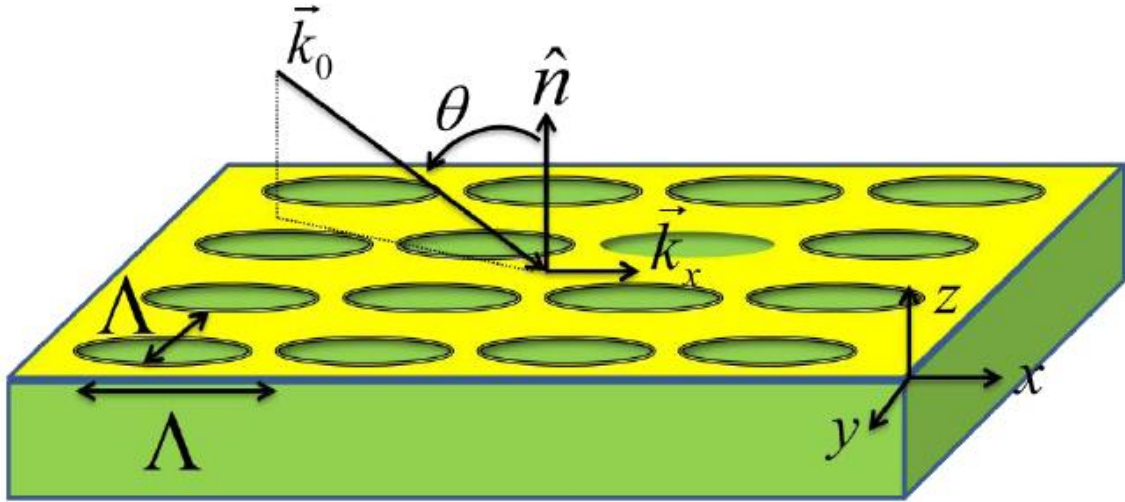


**Figure 54. Graphical representation of a metal slab with a periodic lattice of holes with period  $\Lambda$  for the excitation of SPPs.  $\vec{k}_0$  is the wave vector of the incident light,  $\vec{k}_x$  and  $\vec{k}_y$  are the components of the incident radiation parallel to the surface interface. Taken from [84]**

From Sellers' AFIT thesis [84], the solutions to Eq (46) for the angle and spectral transmission from this type of structure over the ranges of 0-90° and 1-10  $\mu\text{m}$ , respectively, one shown in Figure 55. It can be observed that this design gives greater

control over what wavelengths are allowed to transmit through the surface and which modes propagate within the resonator. The aim is to improve the efficiency of the resonator by narrowing the emittance at the designed wavelength and preventing second-, third-, *ect.*, order peaks that are a characteristic of the Fabry-Perot design. Further theoretical modeling will need to be conducted in order to investigate the effects of integrating this extraordinary transmission filter onto the surface of the resonator.

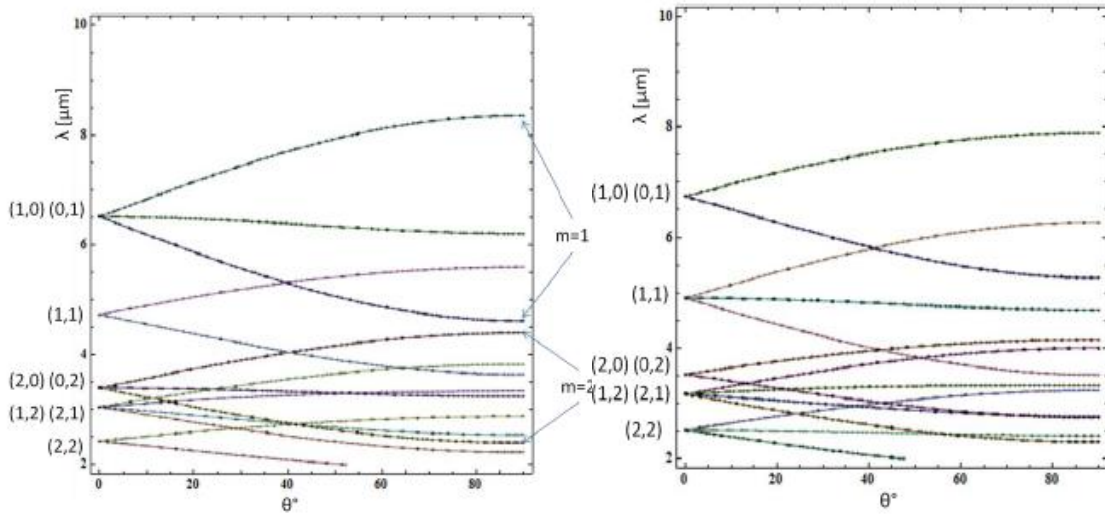


**Figure 55.** Calculated SPP modes for the extraordinary transmission filter with  $\Lambda = 2.08 \mu\text{m}$  where  $\phi_{inc} = 0^\circ$  (right) and  $\phi_{inc} = 45^\circ$  (left). In parentheses are the mode order  $(i, j)$  and  $m$  is the Wood's anomaly modes. Taken from and see [84] for more information.

## Appendix A. Linear Plots of Theoretical Emittance of Ta & W Structures

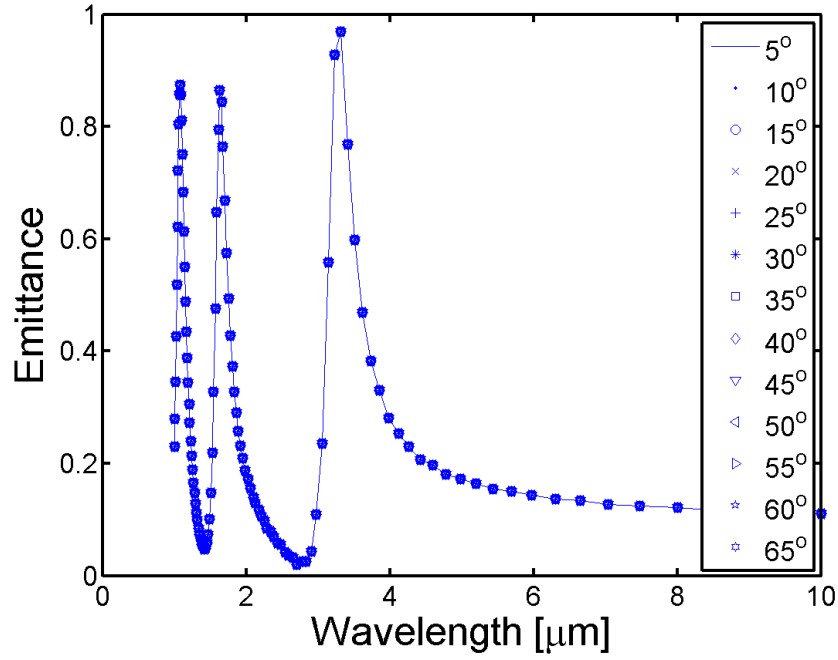


Figure 56. Theoretically inferred total emittance for p-pol source on a Ta-HfO<sub>2</sub>-Ta 6-700-160nm structure simulated using Lumerical FDTD Solutions.

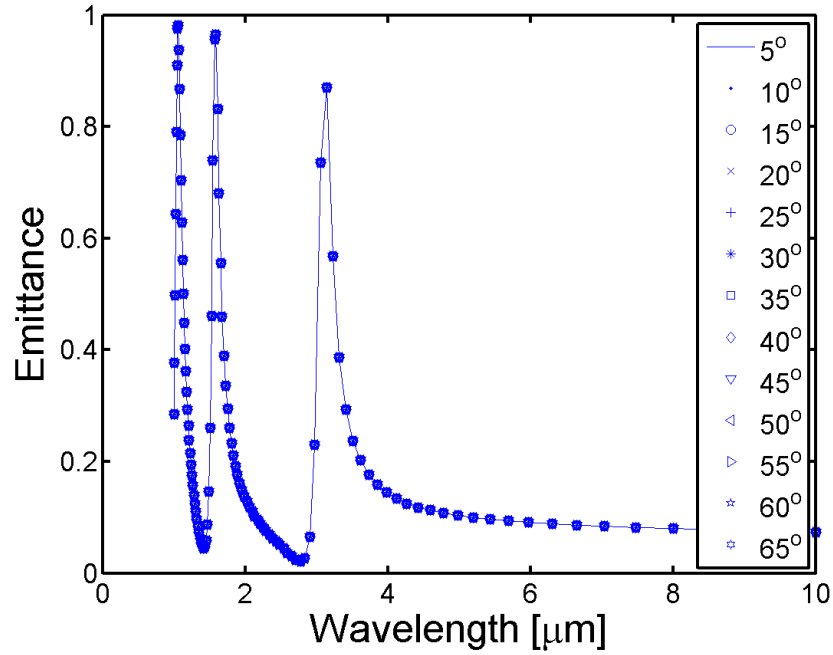
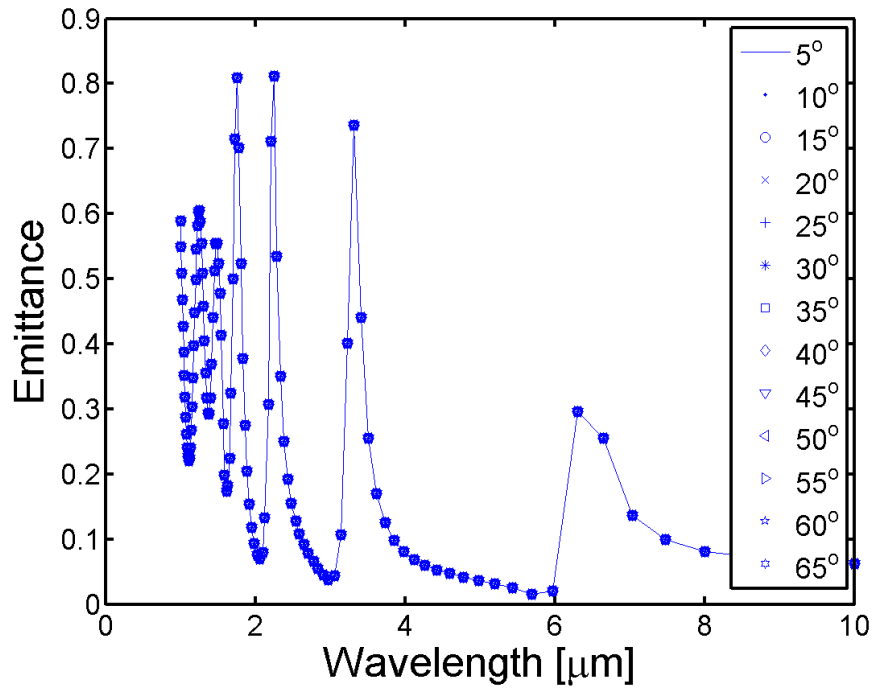
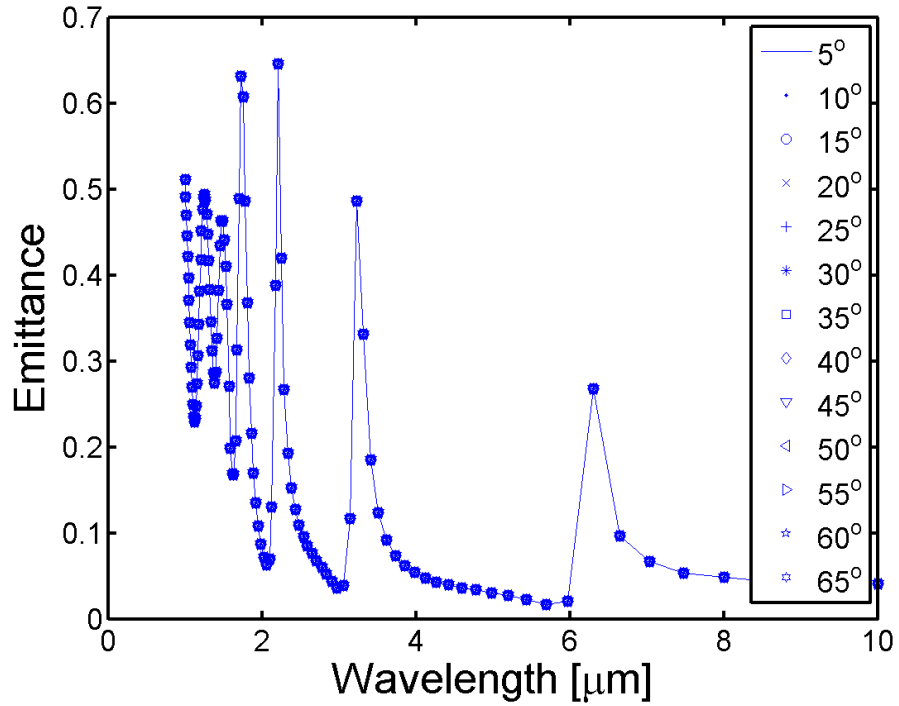


Figure 57. Theoretically inferred total emittance for p-pol source on a Ta-HfO<sub>2</sub>-Ta 10-700-160nm structure simulated using Lumerical FDTD Solutions.



**Figure 58. Theoretically inferred total emittance for p-pol source on a Ta-HfO<sub>2</sub>-Ta 20-700-160nm structure simulated using Lumerical FDTD Solutions.**



**Figure 59. Theoretically inferred total emittance for p-pol source on a Ta-HfO<sub>2</sub>-Ta 30-700-160nm structure simulated using Lumerical FDTD Solutions.**

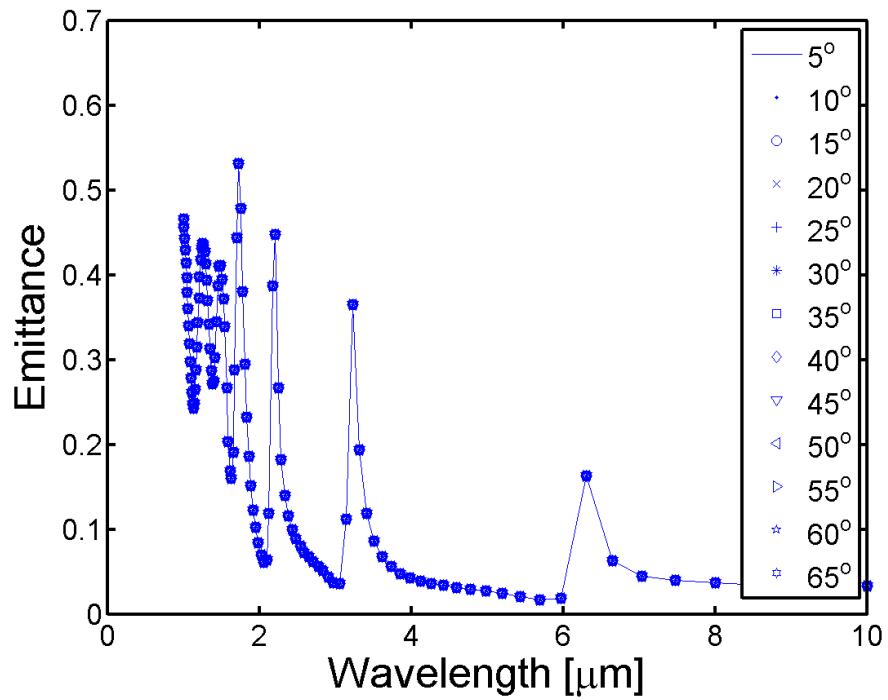


**Figure 60.** Theoretically inferred total emittance for p-pol source on a Ta-HfO<sub>2</sub>-Ta 40-700-160nm structure simulated using Lumerical FDTD Solutions.

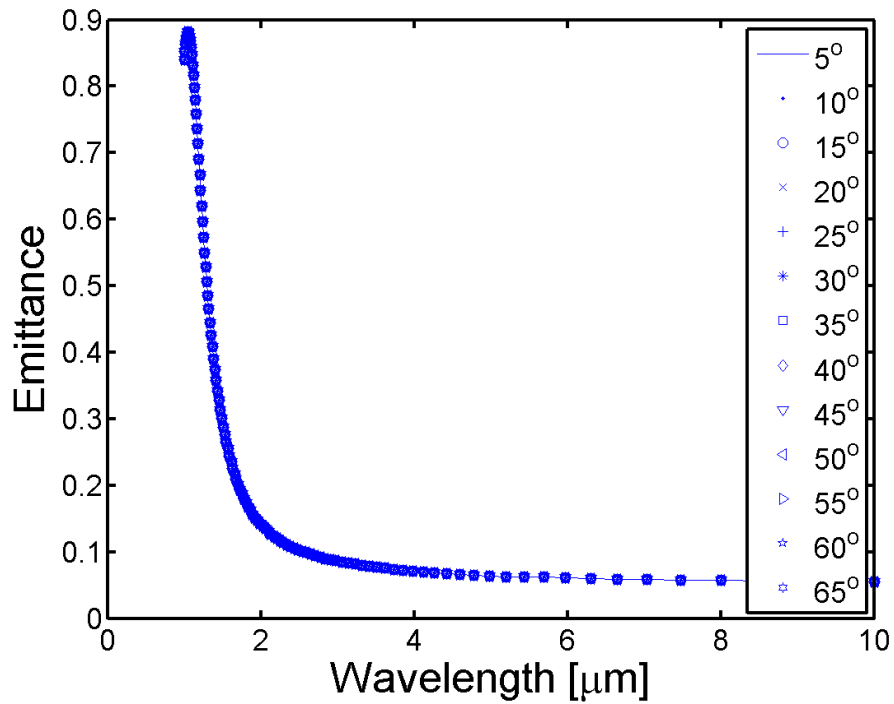


**Figure 61.** Theoretically inferred total emittance for p-pol source on a Ta-HfO<sub>2</sub>-Ta 6-150-160nm structure simulated using Lumerical FDTD Solutions.

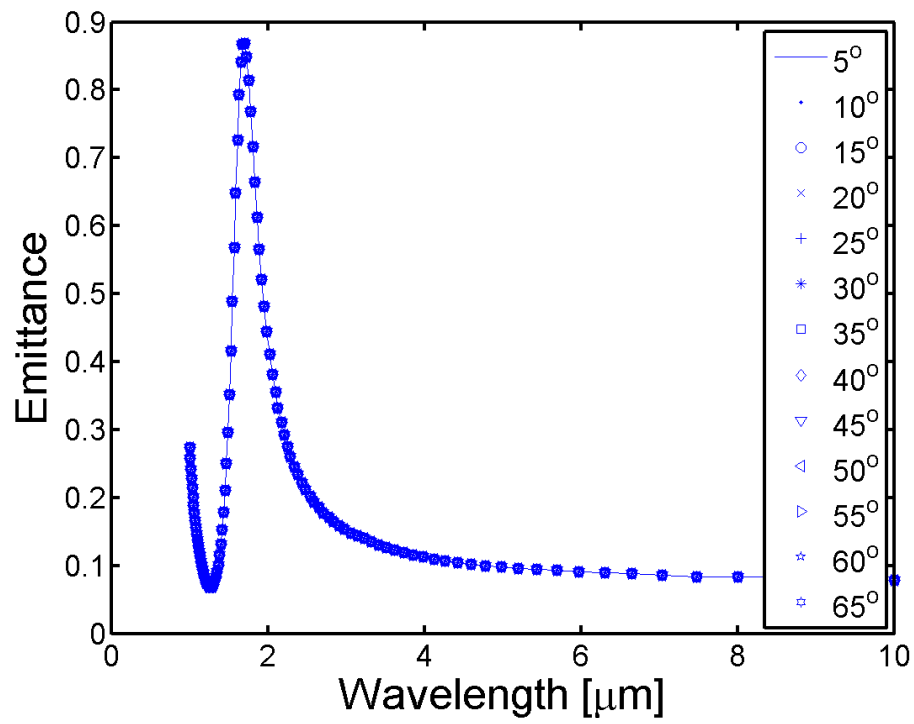


Figure 62. Theoretically inferred total emittance for p-pol source on a Ta-HfO<sub>2</sub>-Ta 6-300-160nm structure simulated using Lumerical FDTD Solutions.

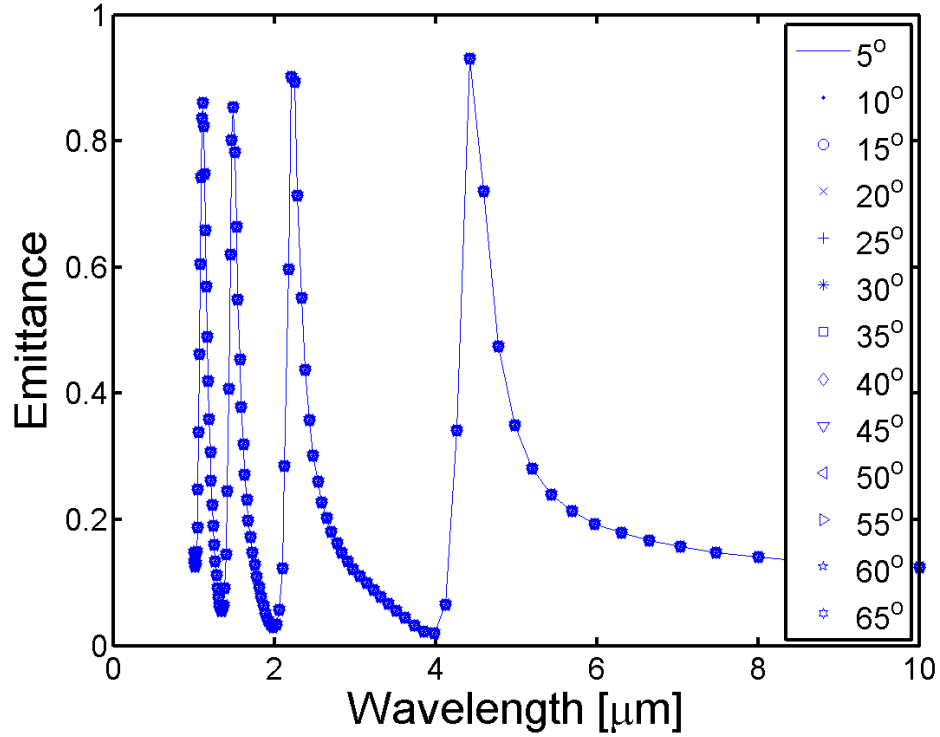


Figure 63. Theoretically inferred total emittance for p-pol source on a Ta-HfO<sub>2</sub>-Ta 6-1um-160nm structure simulated using Lumerical FDTD Solutions.



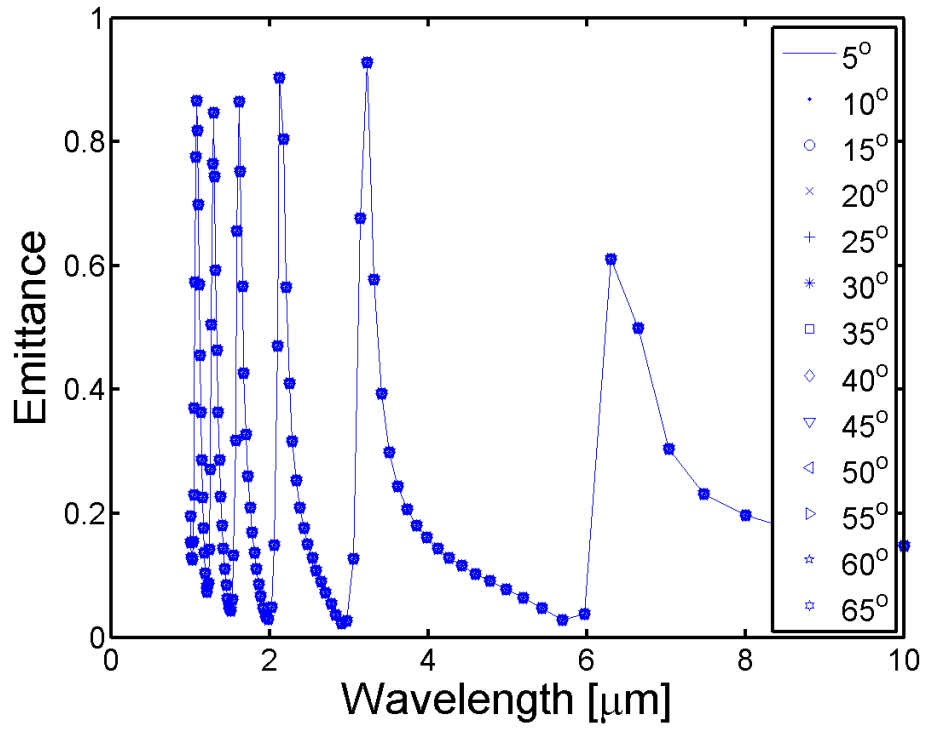


Figure 64. Theoretically inferred total emittance for p-pol source on a Ta-HfO<sub>2</sub>-Ta 6-1.5um-160nm structure simulated using Lumerical FDTD Solutions.

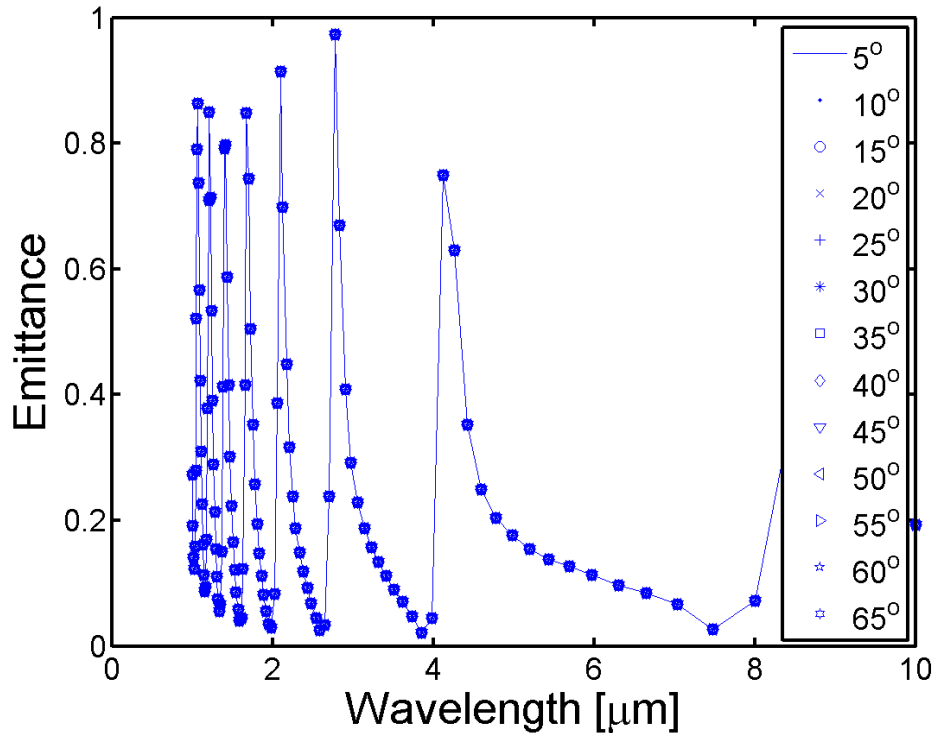


Figure 65. Theoretically inferred total emittance for p-pol source on a Ta-HfO<sub>2</sub>-Ta 6-2um-160nm structure simulated using Lumerical FDTD Solutions.

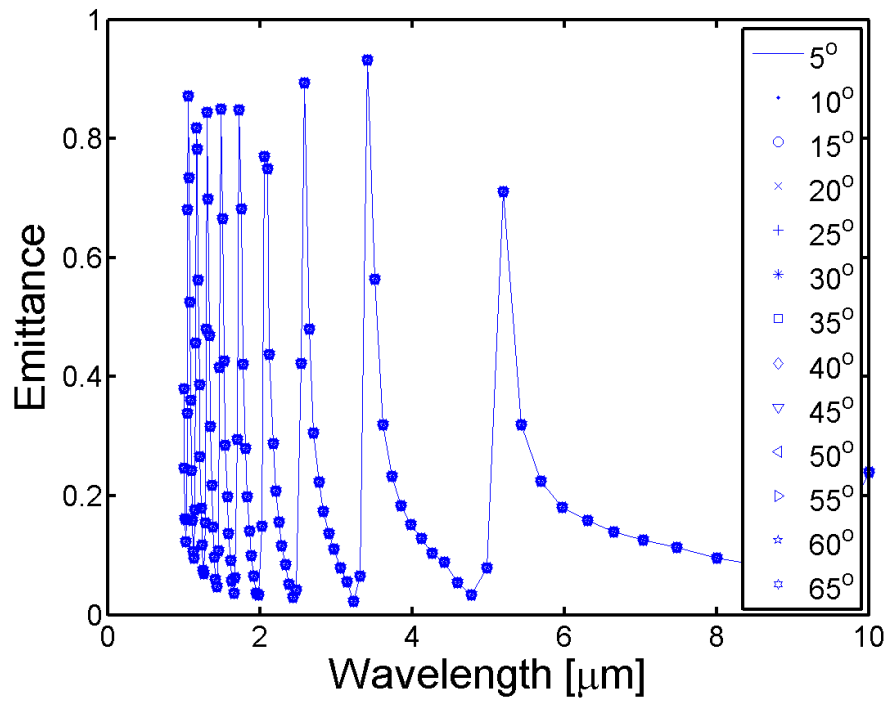


Figure 66. Theoretically inferred total emittance for p-pol source on a Ta-HfO<sub>2</sub>-Ta 6-2.5um-160nm structure simulated using Lumerical FDTD Solutions.

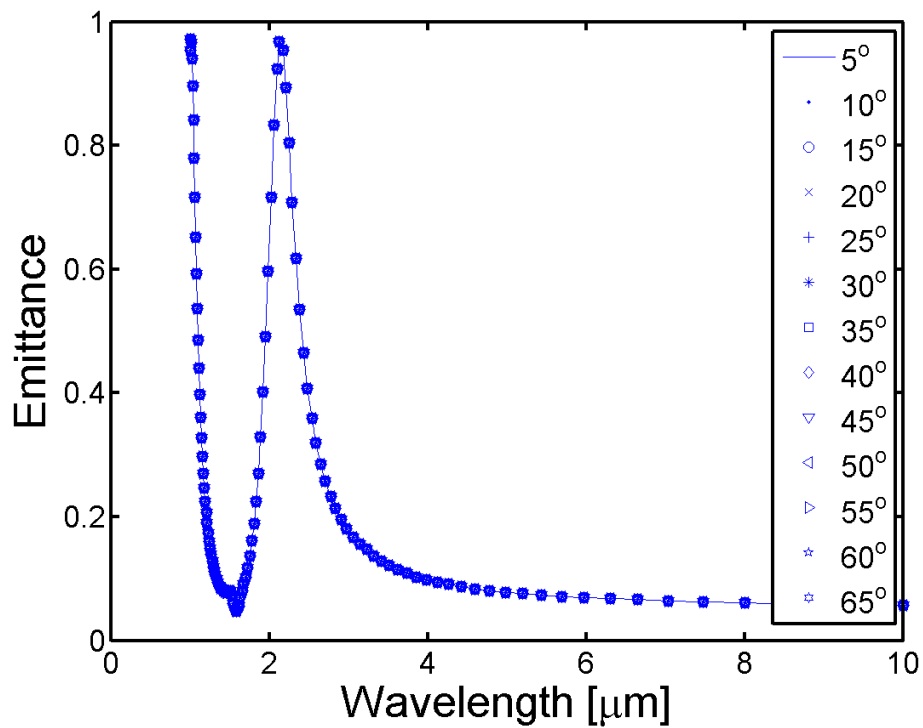


Figure 67. Theoretically inferred total emittance for p-pol source on a Ta-Ge-Ta 6-150-160nm structure simulated using Lumerical FDTD Solutions.

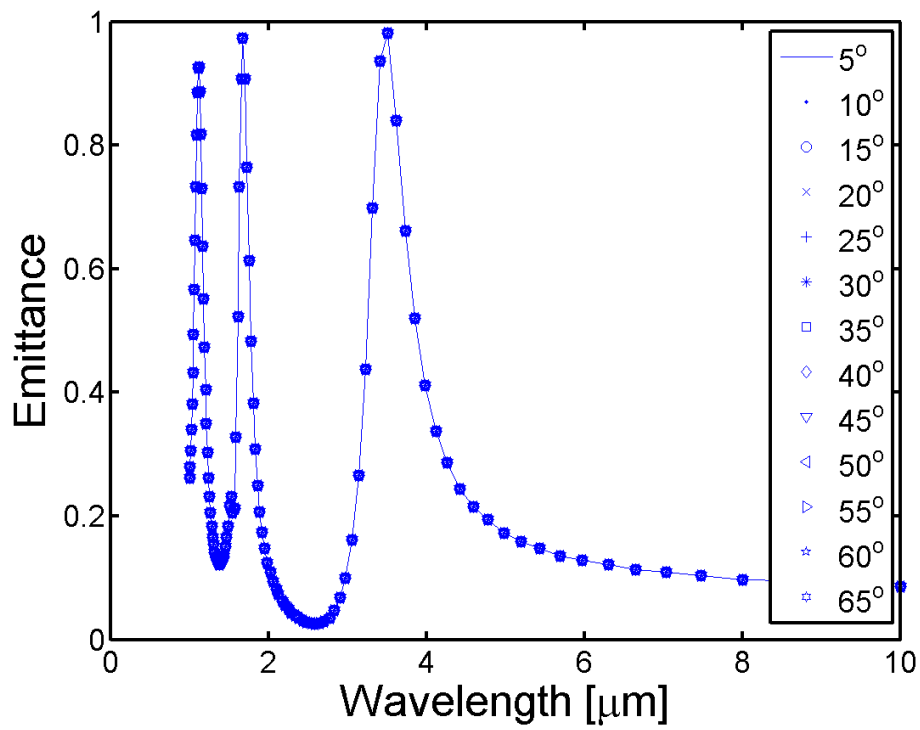


Figure 68. Theoretically inferred total emittance for p-pol source on a Ta-Ge-Ta 6-300-160nm structure simulated using Lumerical FDTD Solutions.

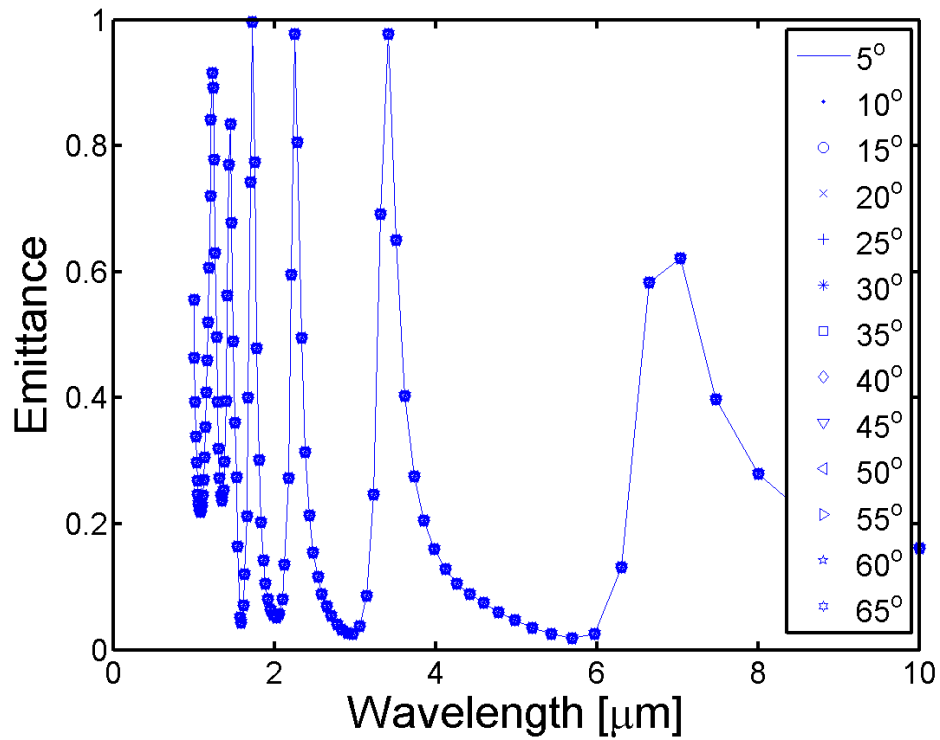


Figure 69. Theoretically inferred total emittance for p-pol source on a Ta-Ge-Ta 6-700-160nm structure simulated using Lumerical FDTD Solutions.

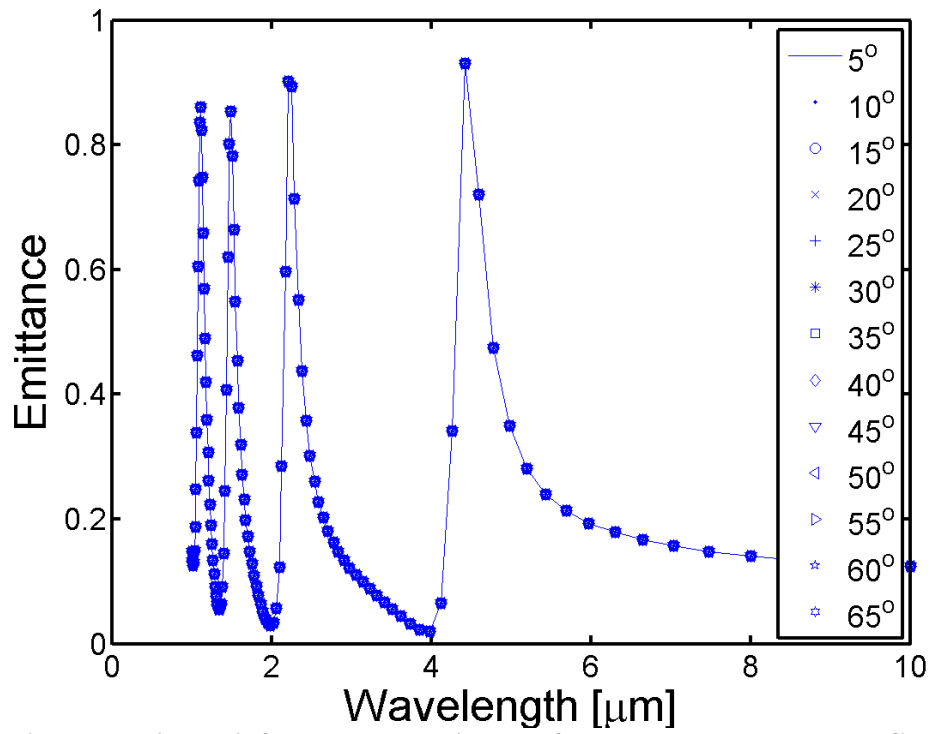


Figure 70. Theoretically inferred total emittance for p-pol source on a Ta-Ge-Ta 6-1μm-160nm structure simulated using Lumerical FDTD Solutions.

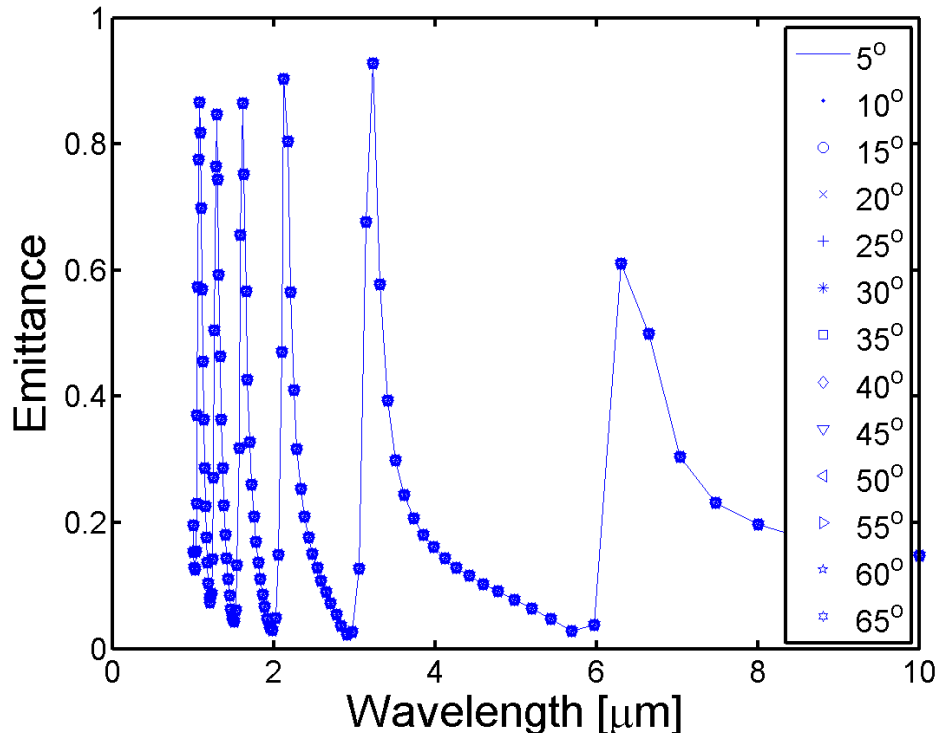


Figure 71. Theoretically inferred total emittance for p-pol source on a Ta-Ge-Ta 6-1.5μm-160nm structure simulated using Lumerical FDTD Solutions.

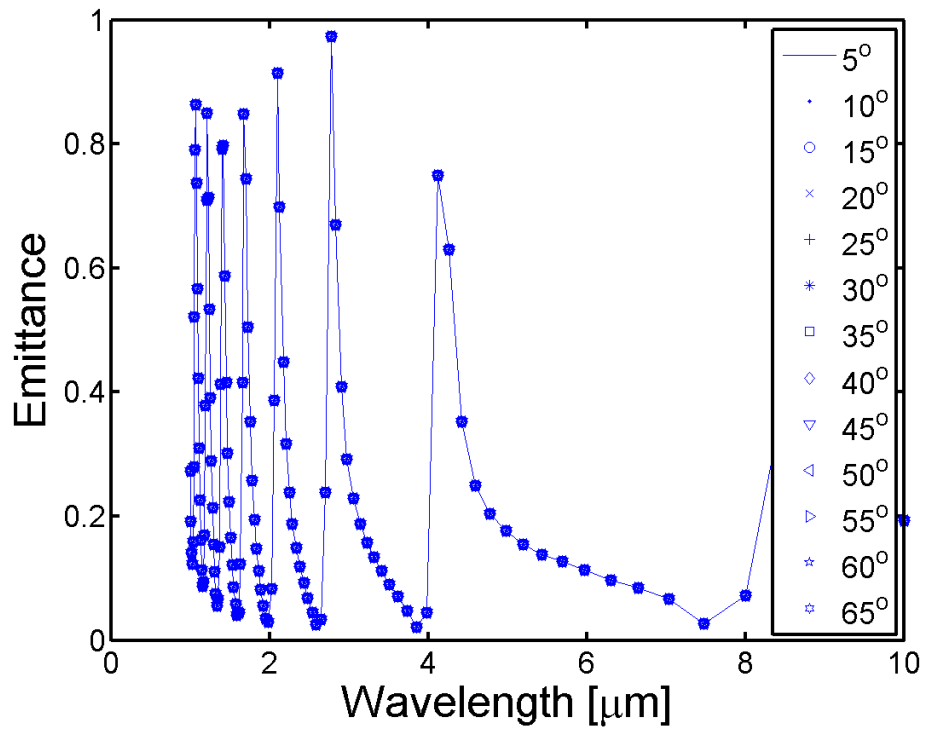


Figure 72. Theoretically inferred total emittance for p-pol source on a Ta-Ge-Ta 6-2um-160nm structure simulated using Lumerical FDTD Solutions.

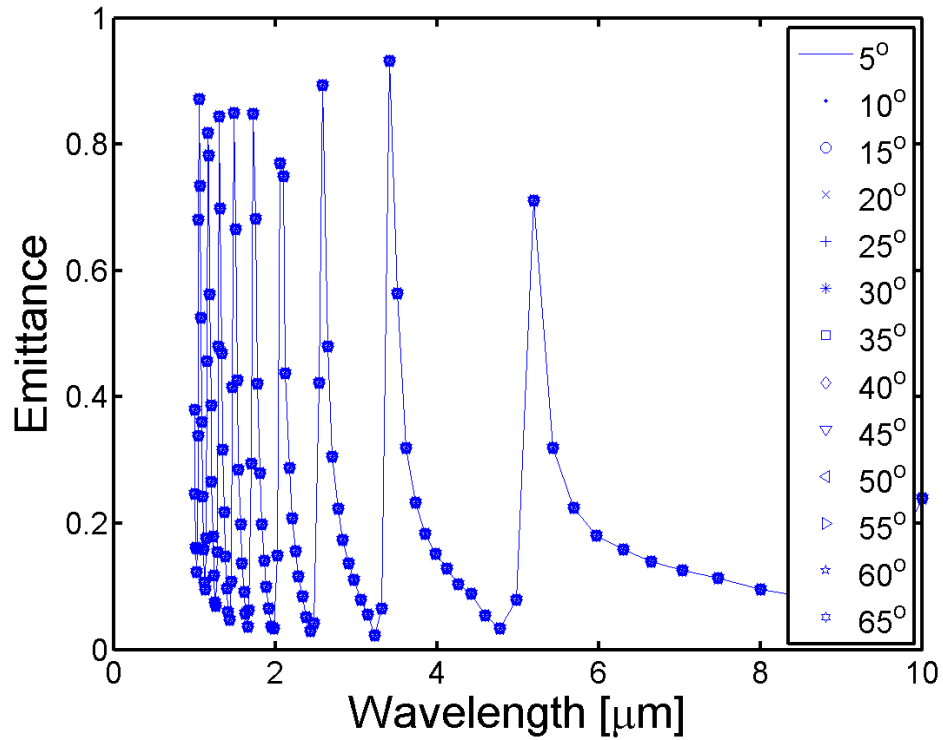


Figure 73. Theoretically inferred total emittance for p-pol source on a Ta-Ge-Ta 6-2.5um-160nm structure simulated using Lumerical FDTD Solutions.

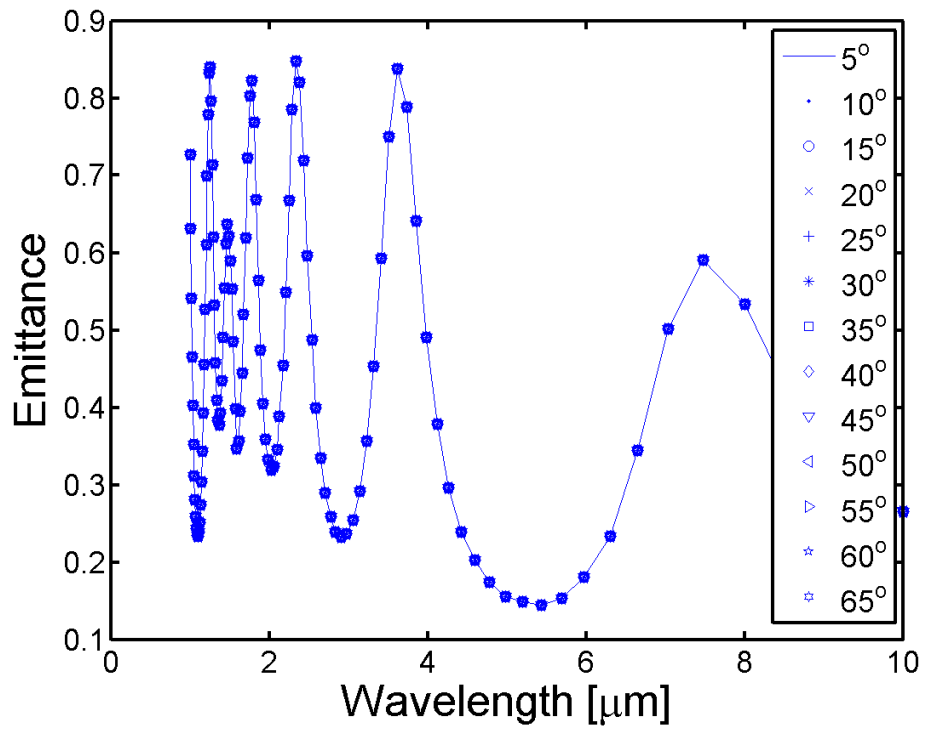


Figure 74. Theoretically inferred total emittance for p-pol source on a W-Ge-W 6-700-160nm structure simulated using Lumerical FDTD Solutions.

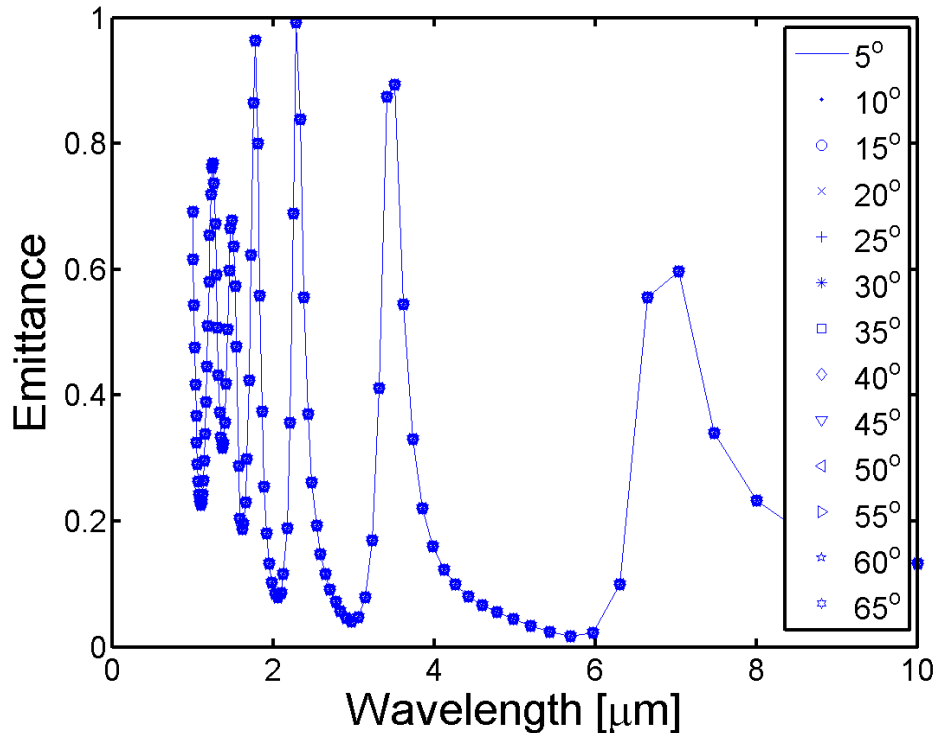


Figure 75. Theoretically inferred total emittance for p-pol source on a W-Ge-W 10-700-160nm structure simulated using Lumerical FDTD Solutions.

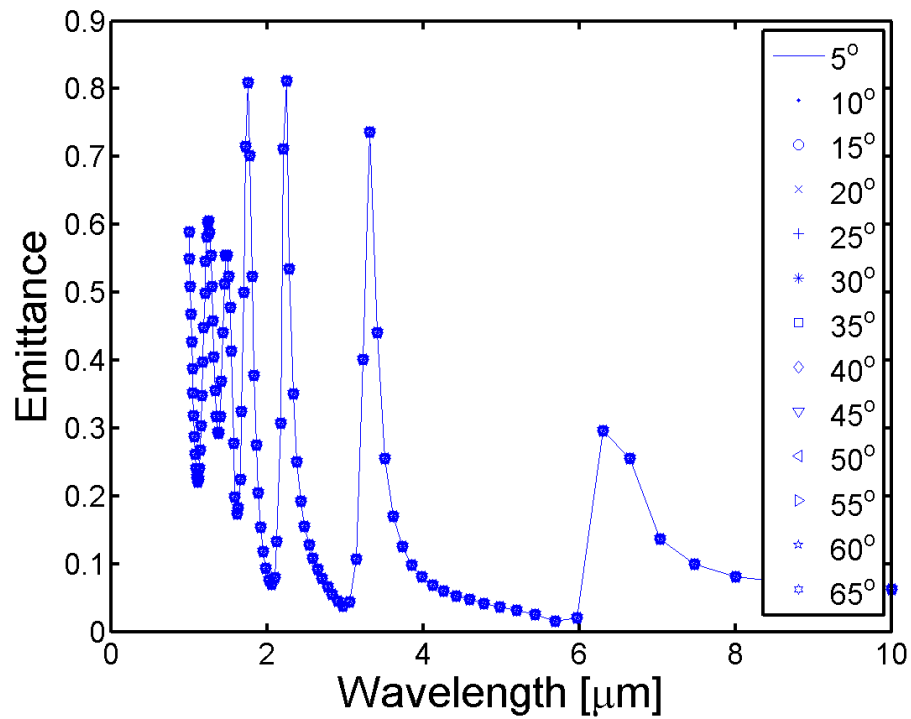


Figure 76. Theoretically inferred total emittance for p-pol source on a W-Ge-W 20-700-160nm structure simulated using Lumerical FDTD Solutions.

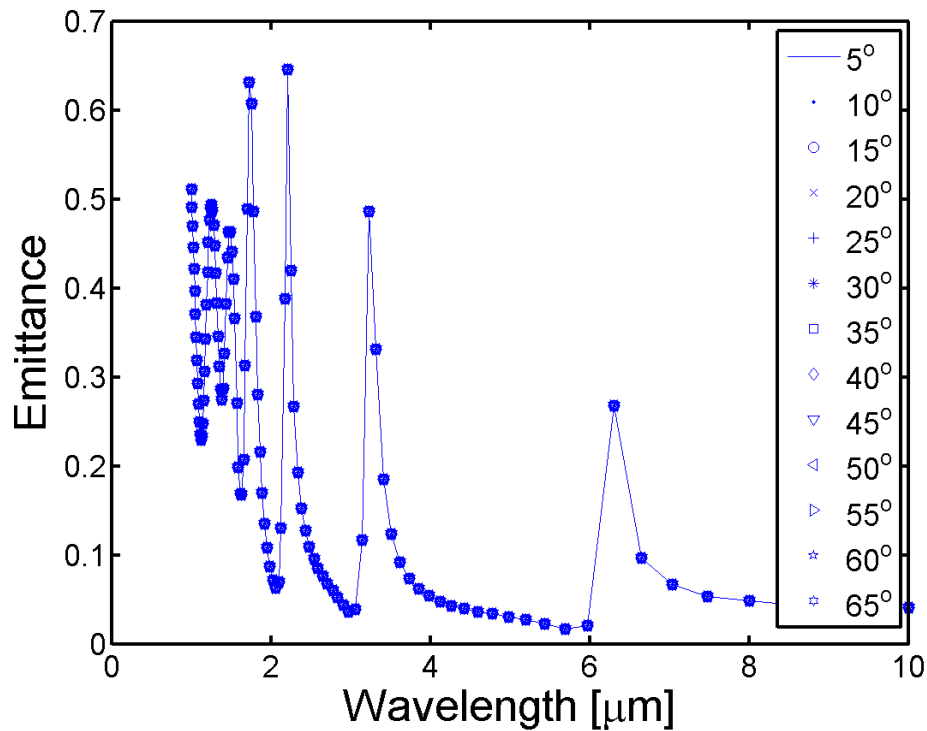


Figure 77. Theoretically inferred total emittance for p-pol source on a W-Ge-W 30-700-160nm structure simulated using Lumerical FDTD Solutions.

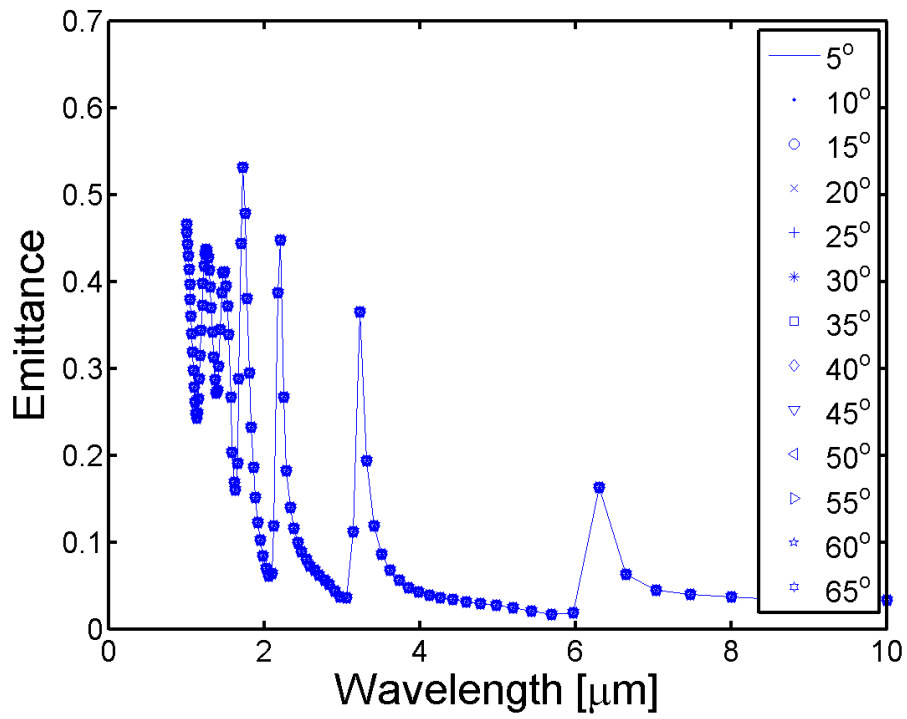


Figure 78. Theoretically inferred total emittance for p-pol source on a W-Ge-W 40-700-160nm structure simulated using Lumerical FDTD Solutions.

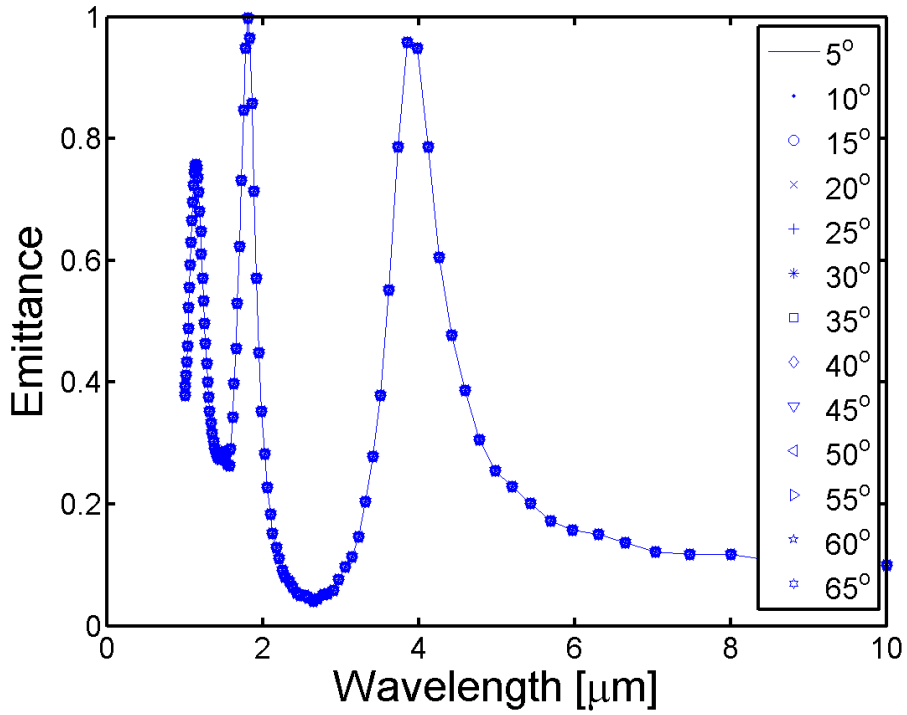


Figure 79. Theoretically inferred total emittance for p-pol source on a W-Ge-W 6-300-160nm structure simulated using Lumerical FDTD Solutions.



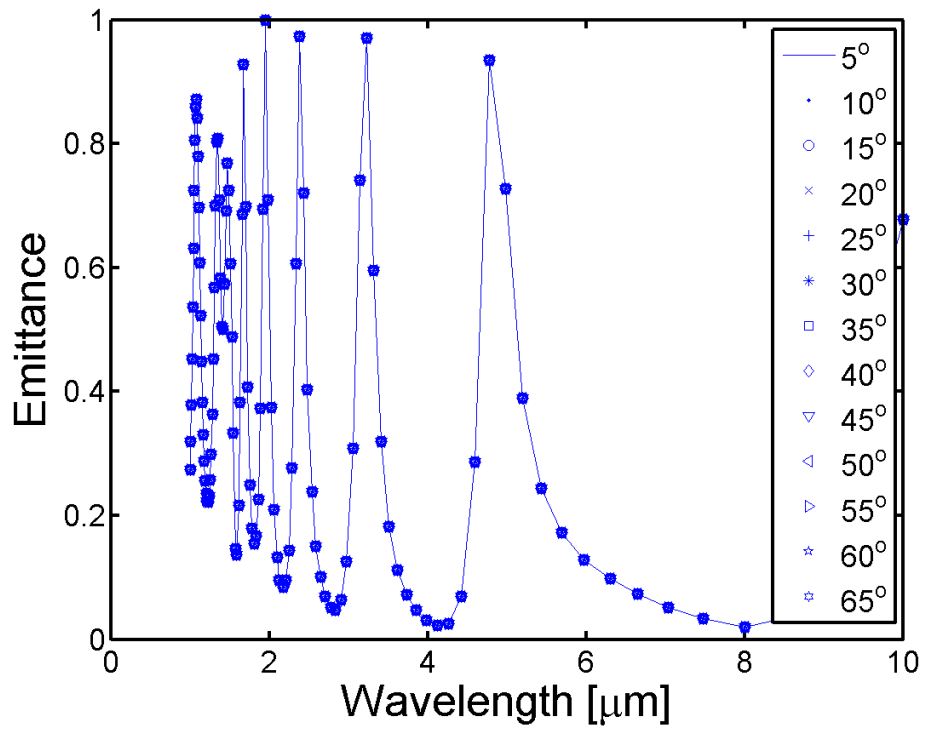


Figure 80. Theoretically inferred total emittance for p-pol source on a W-Ge-W 6-1μm-160nm structure simulated using Lumerical FDTD Solutions.

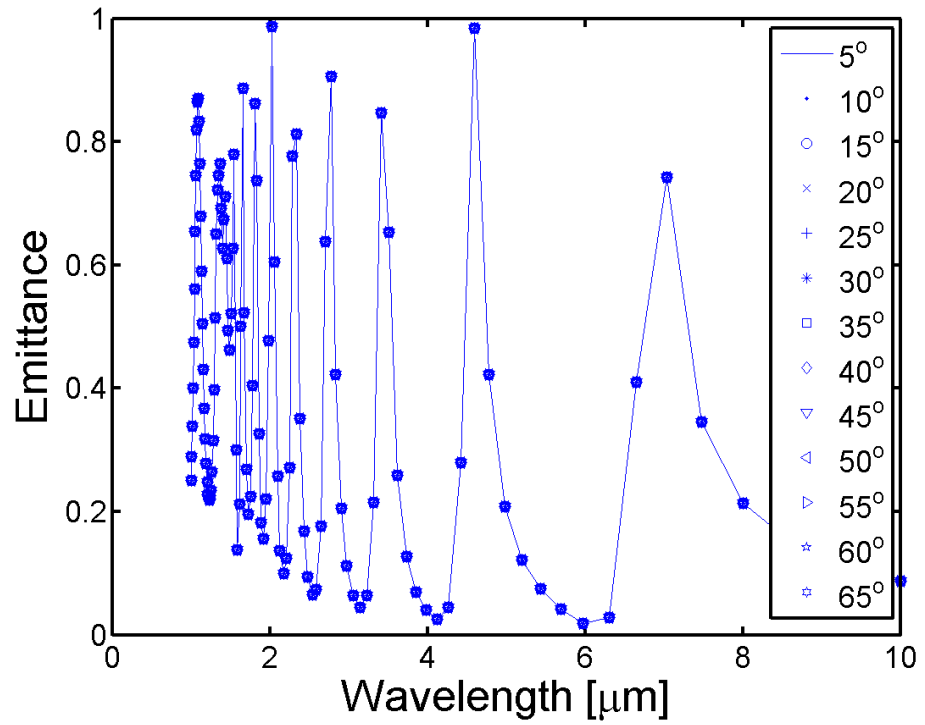


Figure 81. Theoretically inferred total emittance for p-pol source on a W-Ge-W 6-1.5μm-160nm structure simulated using Lumerical FDTD Solutions.

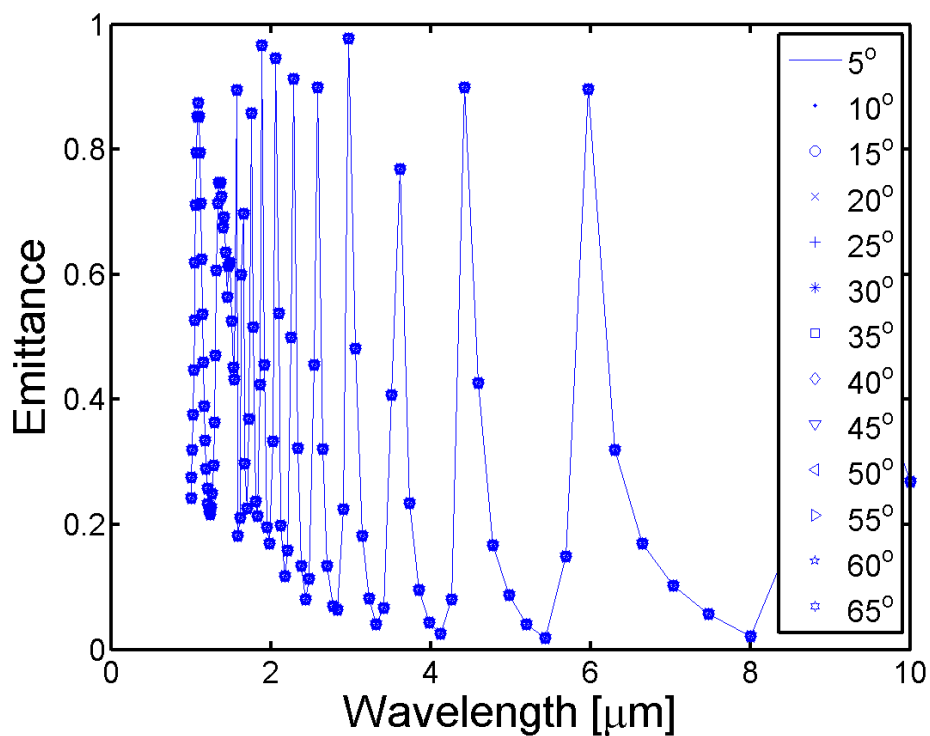


Figure 82. Theoretically inferred total emittance for p-pol source on a W-Ge-W 6-2μm-160nm structure simulated using Lumerical FDTD Solutions.

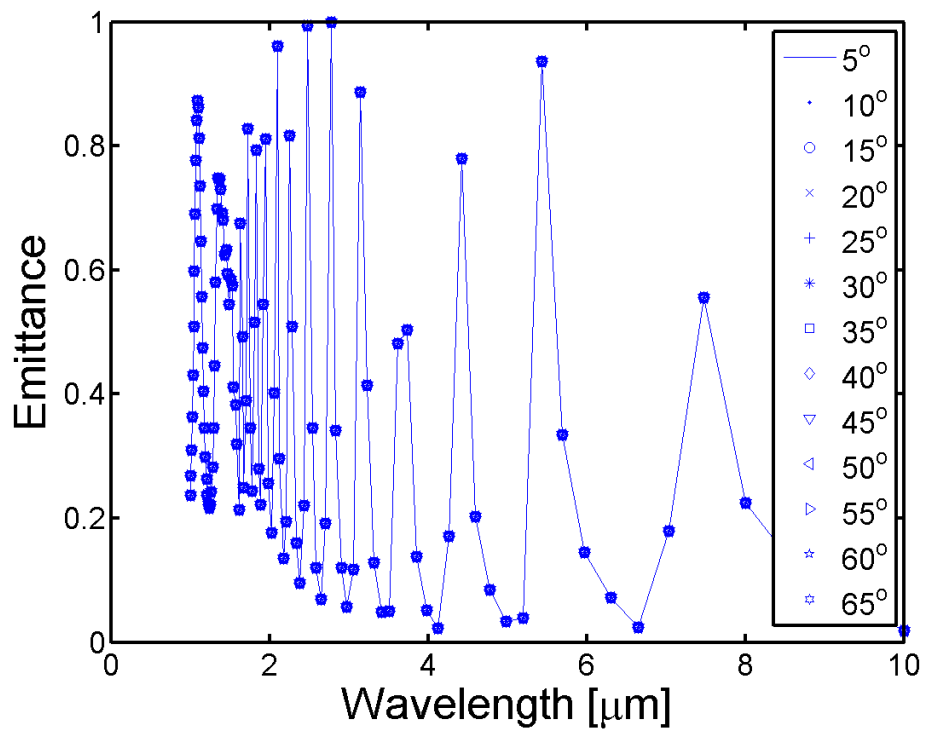


Figure 83. Theoretically inferred total emittance for p-pol source on a W-Ge-W 6-2.5μm-160nm structure simulated using Lumerical FDTD Solutions.

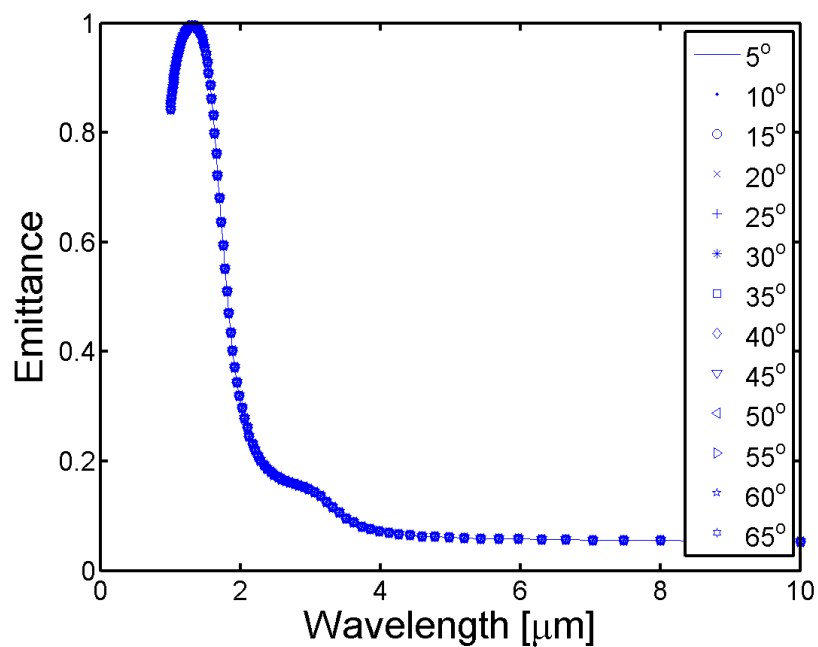


Figure 84. Theoretically inferred total emittance for p-pol source on a W-HfO<sub>2</sub>-W 6-150-160nm structure simulated using Lumerical FDTD Solutions.

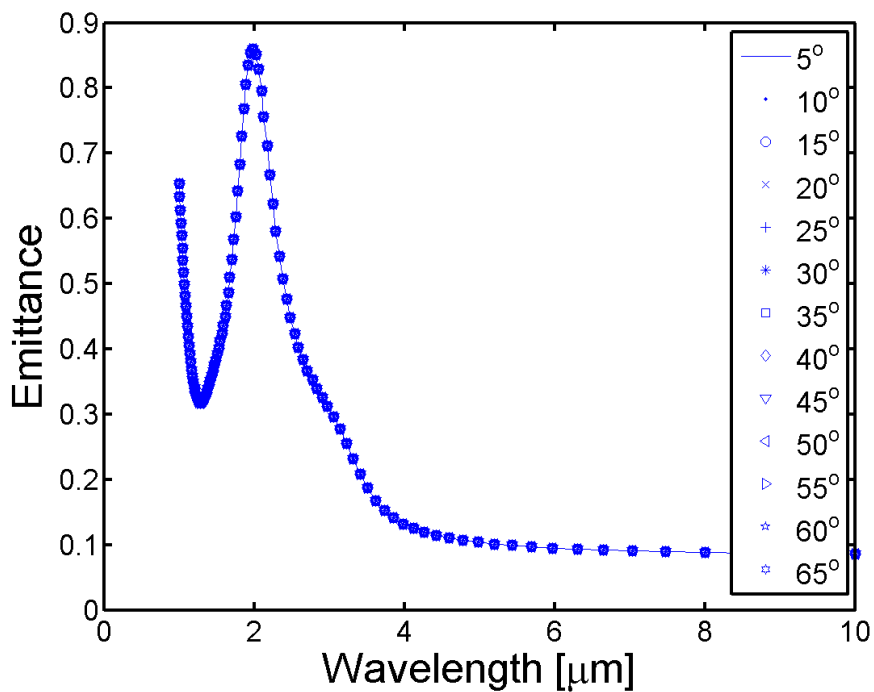


Figure 85. Theoretically inferred total emittance for p-pol source on a W-HfO<sub>2</sub>-W 6-300-160nm structure simulated using Lumerical FDTD Solutions.

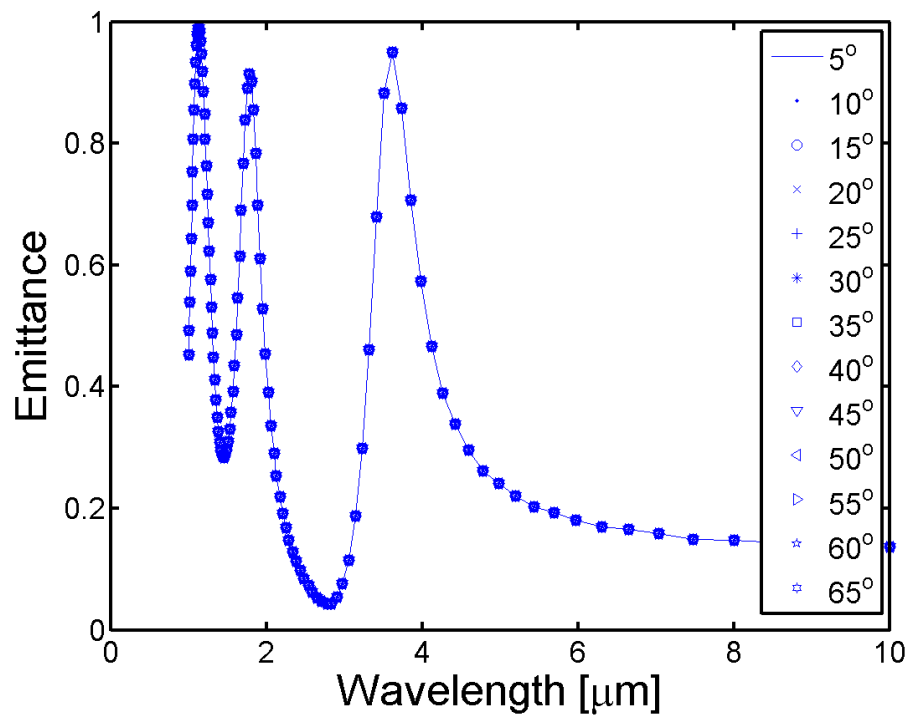


Figure 86. Theoretically inferred total emittance for p-pol source on a W-HfO<sub>2</sub>-W 6-700-160nm structure simulated using Lumerical FDTD Solutions.

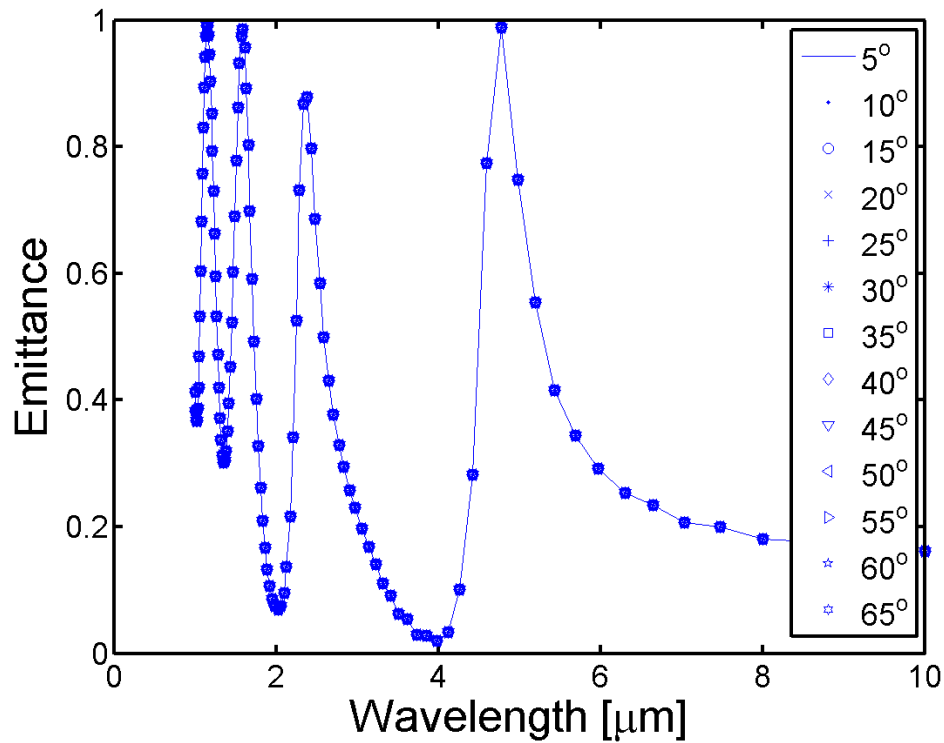


Figure 87. Theoretically inferred total emittance for p-pol source on a W-HfO<sub>2</sub>-W 6-1um-160nm structure simulated using Lumerical FDTD Solutions.

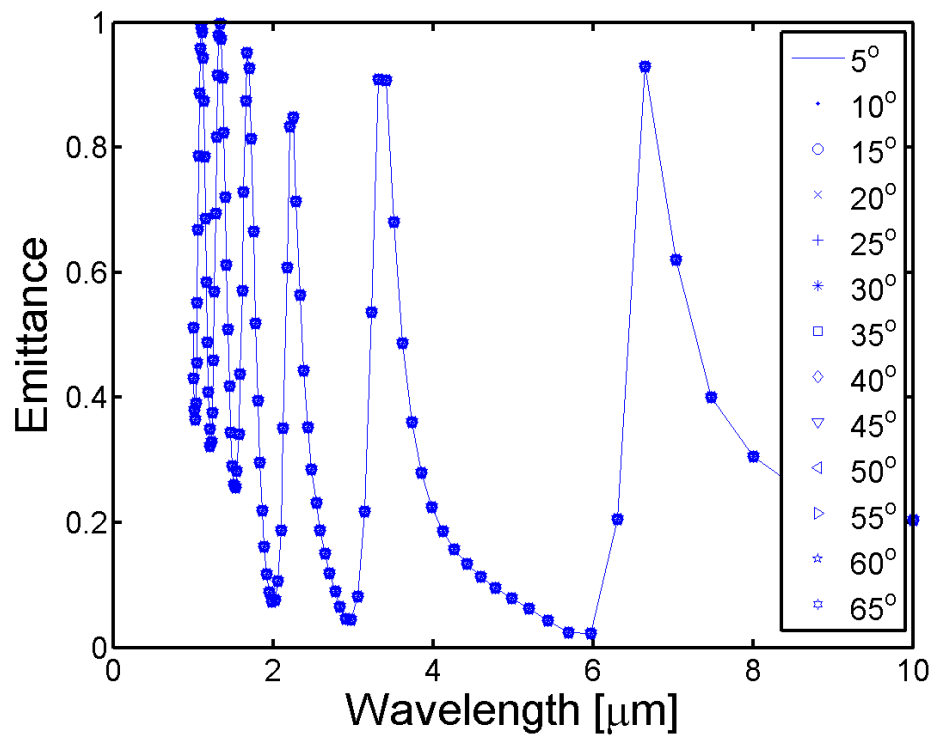


Figure 88. Theoretically inferred total emittance for p-pol source on a W-HfO<sub>2</sub>-W 6-1.5um-160nm structure simulated using Lumerical FDTD Solutions.

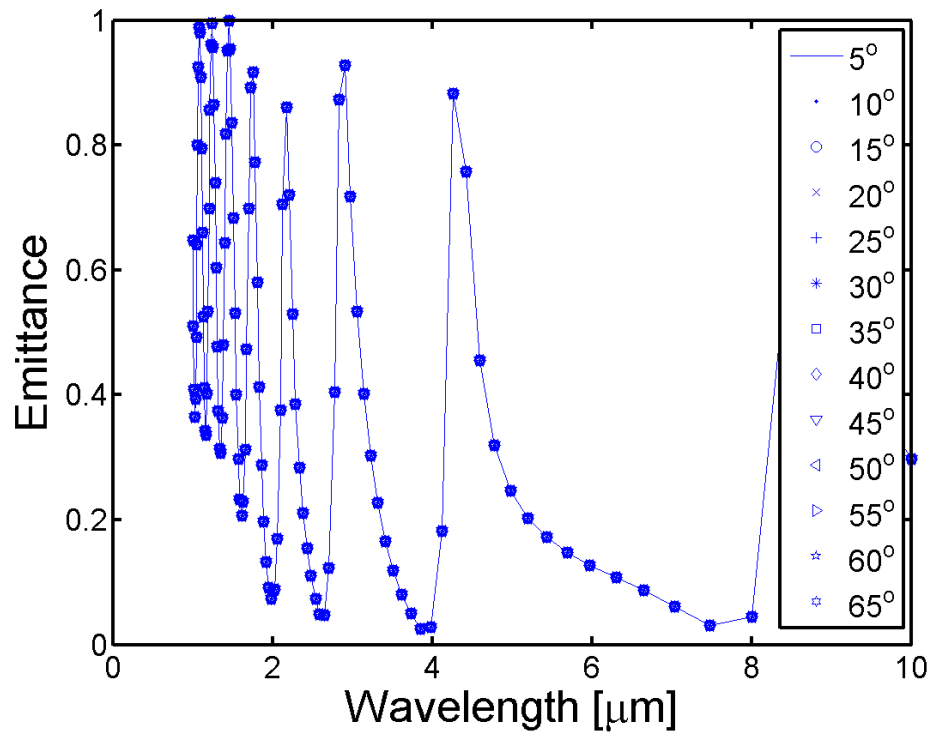
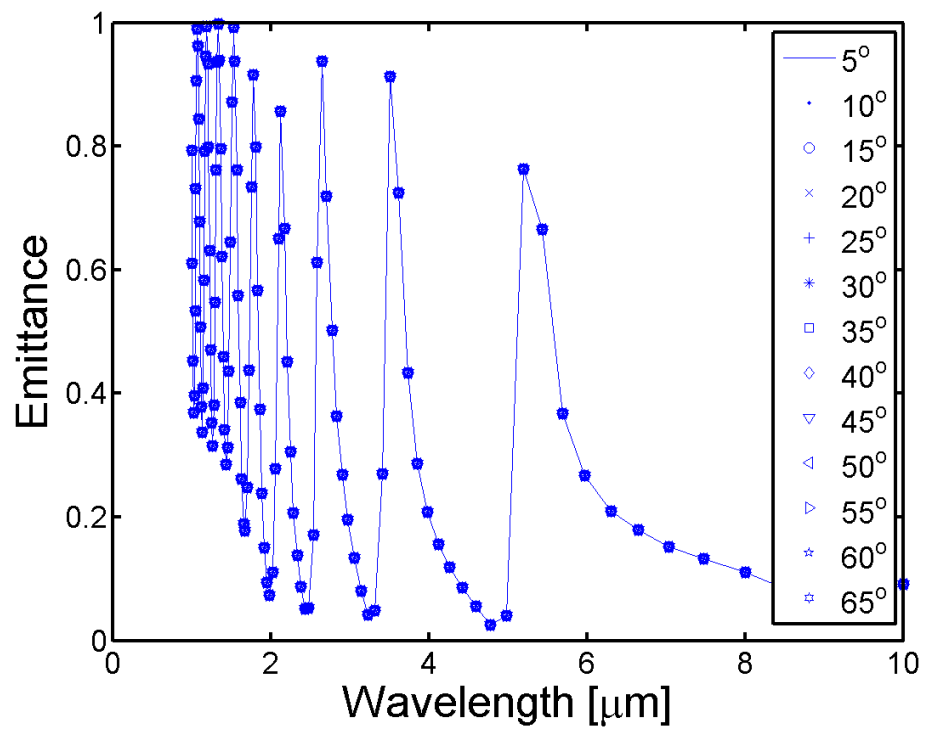


Figure 89. Theoretically inferred total emittance for p-pol source on a W-HfO<sub>2</sub>-W 6-2um-160nm structure simulated using Lumerical FDTD Solutions.



**Figure 90.** Theoretically inferred total emittance for p-pol source on a W-HfO<sub>2</sub>-W 6-2.5um-160nm structure simulated using Lumerical FDTD Solutions.

## Bibliography

- [1] Dictionary.com, 'the definition of thermal radiation', 2015. [Online]. Available: <http://dictionary.reference.com/browse/thermal+radiation>. [Accessed: 15- Feb- 2015].
- [2] J. R. Howell, Thermal Radiation Heat Transfer, Boca Raton: CRC Press, 2011.
- [3] A. Donges, 'The Coherence Length of Black-Body Radiation', *Eur. J. Phys.*, vol. 19, no. 3, pp. 245-249, 1998.
- [4] Skulls in the Stars, 'Optics basics: Coherence', 2008. [Online]. Available: <http://skullsinthestars.com/2008/09/03/optics-basics-coherence/>. [Accessed: 15- Feb- 2015].
- [5] E. L. Dereniak and G. D. Boreman, Infrared Detectors and Systems, Hoboken: John Wiley & Sons, Inc., 1996.
- [6] Goodman, *Introduction to Fourier optics*, 1st ed. Englewood, Colo.: Roberts & Co., 2005.
- [7] J.-J. Greffet, R. Carminati and K. Joulain, 'Coherent emission of light by thermal sources,' *letters to nature*, vol. 416, pp. 61-64, 2002.
- [8] C. A. Balanis, Advanced Engineering Electromagnetics, New Jersey: Wiley, 1989.
- [9] B. J. Lee and Z. M. Zhang, 'Coherent Thermal Emission from Modified Periodic Multilayer Structures,' *Journal of Heat Transfer*, vol. 129, pp. 17-26, 2007.
- [10] P. Yeh, A. Yariv and A. Cho, 'Optical surface waves in periodic layered media', *Applied Physics Letters*, vol. 32, no. 2, p. 104, 1978.
- [11] W. Robertson and M. May, 'Surface electromagnetic wave excitation on one-dimensional photonic band-gap arrays', *Applied Physics Letters*, vol. 74, no. 13, p. 1800, 1999.
- [12] J. Gaspar-Armenta and F. Villa, 'Photonic surface-wave excitation: photonic crystal-metal interface', *J. Opt. Soc. Am. B*, vol. 20, no. 11, p. 2349, 2003.

- [13] L. P. Wang, B. J. Lee, X. J. Wang and Z. M. Zhang, 'Spatial and temporal coherence of thermal radiation in asymmetric Fabry-Perot resonance cavities,' *International Journal of Heat and Mass Transfer*, vol. 52, pp. 3024-3031, 2009.
- [14] I. Celanovic, D. Perreault and J. Kassakian, 'Resonant-cavity enhanced thermal emission,' *Physical Review B*, vol. 72, no. 075127, 2005.
- [15] E. Schubert, N. Hunt, A. Vredenberg, T. Harris, J. Poate, D. Jacobson, Y. Wong and G. Zydzik, 'Enhanced photoluminescence by resonant absorption in Er-doped SiO<sub>2</sub>/Si microcavities', *Applied Physics Letters*, vol. 63, no. 19, p. 2603, 1993.
- [16] P. Ben-Abdallah and B. Ni, 'Single-defect Bragg stacks for high-power narrow-band thermal emission', *J. Appl. Phys.*, vol. 97, no. 10, p. 104910, 2005.
- [17] Y. -T. Chang, Y. -T. H. S. -W. Wu, H. -F. Huang and S. -C. Lee, 'Planar Tri-layer Ag/SiO<sub>2</sub>/Ag Plasmonic Thermal Emitter with Coherent Thermal Emission,' in *Metamorphose-VI*, London, 2009.
- [18] I. Moreno, J. Araiza, M. Avendano-Alejo, 'Thin-film spatial filters', *Optics Letters*, vol 30, iss 8, pp. 914–916, 2005.
- [19] Y. Yeng, J. Chou, V. Rinnerbauer, Y. Shen, S. Kim, J. Joannopoulos, M. Soljacic and I. Celanovic, 'Global Optimization of Omnidirectional Wavelength Selective Emitters/Absorbers based on Dielectric-filled Anti-Reflection Coated Two-Dimensional Metallic Photonic Crystals,' *Optics Express*, vol. 22, no. 18, pp. 21711–21718, 2014.
- [20] P. Berning, 'Theory and Calculations of Optical Thin Films', *Physics of Thin Films*. Academic Press, New York, NY, pp. 69-121, 1963.
- [21] J. -J. Greffet and C. Henkel, 'Coherent Thermal Radiation,' *Contemporary Physics*, vol. 48, no. 4, pp. 183-194, 2007.
- [22] B. Lee, C. Fu and Z. Zhang, 'Coherent thermal emission from one-dimensional photonic crystals', *Applied Physics Letters*, vol 87, iss 7, p. 071904, 2005.
- [23] S. Babiker, S. Yong, M. Sid-Ahmed and X. Ming, 'Thermophotovoltaic Emitters Based on a One-Dimensional Metallic-Dielectric Multilayer Nanostructures', *Journal of Electronics Cooling and Thermal Control*, vol 2014, 2014.



- [24] B. J. Lee and Z. M. Zhang, 'Design and fabrication of planar multilayer structures with coherent thermal emission characteristics,' *Journal of Applied Physics*, vol. 100, no. 063529, 2006.
- [25] J. Drevillon, K. Joulain, P. Ben-Abdallah and E. Nefzaoui, 'Far field coherent thermal emission from a bilayer structure,' *Journal of Applied Physics*, vol. 109, no. 034315, pp. 1-7, 2011.
- [26] S. A. A. Oloomi, A. Saboonchi and A. Sedaghat, 'Thermal Radiative Properties of Nanoscale Semiconductors with Incoherent Formulation,' *Majlesi Journal of Mechanical Engineering*, vol. 3, no. 2, pp. 45-52, 2010.
- [27] B. J. Lee and Z. M. Zhang, 'Coherent Thermal Emission from Modified Periodic Multilayer Structures,' *Journal of Heat Transfer*, vol. 129, pp. 17-26, 2007.
- [28] Y. -T. Chang, Y. -T. H. S. -W. Wu, H. -F. Huang and S. -C. Lee, 'Planar Tri-layer Ag/SiO<sub>2</sub>/Ag Plasmonic Thermal Emitter with Coherent Thermal Emission,' in *Metamorphose-VI*, London, 2009.
- [29] A. Narayanaswamy and G. Chen, 'Thermal Emission Control with One-Dimensional Metallodielectric Photonic Crystals,' *Physical Review B*, vol. 70, no. 12511, 2004.
- [30] M. Takagi, 'Electron-Diffraction Study of Liquid-Solid Transition of Thin Metal Films,' *Journal of the Physical Society of Japan*, vol. 9, no. 3, p. 359-363, 1954.
- [31] S. McConnell, 'Spectral and Spatial Coherent Emission of Thermal Radiation from Metal-Semiconductor Nanostructures', M.S. thesis, AFIT/EE.ABET/ENP/12-M01. School of Engineering and Management, Air Force Institute of Technology (AU), Wright-Patterson AFB OH, March 2012.
- [32] Y. Yeng, M. Ghebrebrhan, P. Bermel, W. Chan, J. Joannopoulos, M. Soljavicic and I. Celanovic, 'Enabling high-temperature nanophotonics for energy applications', *Proceedings of the National Academy of Sciences*, vol 109, iss 7, pp. 2280--2285, 2012.
- [33] O. G. Kollyukh, L. A. I. V. Morozhenko and V. I. Pipa, "Thermal radiation of planeparallel semitransparent layers," *Optics Communications*, vol. 225, pp. 349-352, 2003.
- [34] E. Nefzaoui, J. Drevillon and K. Joulain, 'Selective emitters design and optimization for thermophotovoltaic applications', *Journal of Applied Physics*, vol 111, iss 8, p. 084316, 2012.

- [35] S. Shu, L. Zheng, H. Li, C. Tsang, L. Shi and Y. Li, 'Porous metal-based multilayers for selective thermal emitters', *Optics letters*, vol 37, iss 23, pp. 4883-4885, 2012.
- [36] I. Celanovic, F. O'Sullivan, M. Ilak, J. Kassakian and D. Perreault, 'Design and optimization of one-dimensional photonic crystals for thermophotovoltaic applications', *Optics letters*, vol 29, iss 8, pp. 863-865, 2004.
- [37] J. Chou, Y. Yeng, A. Lenert, V. Rinnerbauer, I. Celanovic, M. Soljavcic, E. Wang and S. Kim, 'Design of wide-angle selective absorbers/emitters with dielectric filled metallic photonic crystals for energy applications', *Optics Express*, vol 22, iss 101, pp. 144--154, 2013.
- [38] E. D. Palik, *Handbook of Optical Constants of Solids*. San Diego: Academic Press, 1998.
- [39] Y. Shuai, H. Tan and Y. Liang, 'Polariton-enhanced emittance of metallic--dielectric multilayer structures for selective thermal emitters', *Journal of Quantitative Spectroscopy and Radiative Transfer*, vol 135, pp. 50--57, 2014.
- [40] J. A. Mason, S. Smith and D. Wasserman, 'Strong absorption and selective thermal emission from a midinfrared metamaterial,' *Applied Physics Letters*, vol. 98, no. 241105, 2011.
- [41] X. Liu, T. Tyler, T. Starr, A. F. Starr, N. M. Jokerst and W. J. Padilla, 'Taming the Blackbody with Infrared Metamaterials as Selective Thermal Emitters,' *Physical Review Letters*, vol. 107, no. 045901, pp. 1-4, 2011.
- [42] S. L. Wadsworth, P. G. Clem, E. D. Branson and G. D. Boreman, 'Broadband circularly-polarized infrared emission from multilayer metamaterials,' *Optical Materials Express*, vol. 1, no. 3, pp. 466-479, 2011.
- [43] B. Lee, L. Wang and Z. Zhang, 'Coherent thermal emission by excitation of magnetic polaritons between periodic strips and a metallic film', *Optics Express*, vol 16, iss 15, pp. 11328--11336, 2008.
- [44] K. Joulain, J.-P. Mulet, F. Marquier, R. Carminati and J.-J. Greffet, "Surface electromagnetic waves thermally excited: Radiative heat transfer, coherence properties and Casimir forces revisited in the near field," *Surface Science Reports*, vol. 57, pp. 59-112, 2005.
- [45] C.-Y. Chen, M.-W. Tsai, Y.-W. Jiang, Y.-H. Ye, Y.-T. Chang and S.-C. Lee, 'Coupling of surface plasmons between two silver films in a plasmonic thermal emitter,' *Applied Physics Letters*, vol. 91, no. 243111, 2007.

- [46] J. J. Burke, G. I. Stegeman and T. Tamir, 'Surface-polariton-like waves guided by thin, lossy metal films,' *Physical Review B*, vol. 33, pp. 5186-5201, 1986.
- [47] R. T. Holm, 'Convention Confusions,' in *Handbook of Optical Constants of Solids II*, Chestnut Hill, Academic Press, p. 21-55, 1991.
- [48] B. Saleh and M. Teich, *Fundamentals of photonics*, 2nd ed. Hoboken, NJ: Wiley, 2007, p. 211.
- [49] Lipson, S G.; Lipson, H; Tannhauser, D. S. (1995) *Optical Physics* (3<sup>rd</sup> ed). London: Cambridge U.P. p. 248
- [50] E.D. Palik. *Handbook of Optical Constants of Solids* (1<sup>st</sup> ed.), 1975.
- [51] Shackelford and W. Alexander, *CRC Materials Science and Engineering Handbook*. Boca Raton, Fl: CRC Press, 2001.
- [52] Lumerical Solutions, "Lumerical Solutions, FDTD Solutions Knowledge Base," 2014.
- [53] H. Tompkins and E. Irene, *Handbook on Ellipsometry*, Norway, NY: William Andrew Pub., 2005.
- [54] H. Fujiwara, *Spectroscopic Ellipsometry*. Chichester, England: John Wiley & Sons, 2007.
- [55] Hans-Jurgen Butt, Kh Graf, and Michael Kappl, 'Measurement of Adsorption Isotherms,' *Physics and Chemistry of Interfaces*. Weinheim: Wiley-VCH, 2006. 206-09. Print.
- [56] *A guide to using WVASE32: Spectroscopic ellipsometry data acquisition and analysis software*. J. A. Woollam Co. Inc., 1994.
- [57] E. D. Palik, *Handbook of Optical Constants of Solids*, Orlando: Academic Press, INC., 1985.
- [58] A. Rakic, A. Djurišic, J. Elazar and M. Majewski, 'Optical Properties of Metallic Films for Vertical-Cavity Optoelectronic Devices', *Applied Optics*, vol. 37, no. 22, p. 5271, 1998.
- [59] E. Ozbay, 'The Magical World of Photonic Metamaterials,' *Optics & Photonics News*, vol. 19, no. 11, p. 22, 2008.

- [60] 'Photonic Metamaterials,' *Encyclopedia of Laser Physics and Technology*. Wiley, p. 1, 2008.
- [61] Ioffe.ru, 'Physical properties of Germanium (Ge),' 2015. [Online]. Available: <http://www.ioffe.ru/SVA/NSM/Semicond/Ge/>. [Accessed: 18-Jan-2015].
- [62] Photonics.com, 'Common Infrared Optical Material,' 2015. [Online]. Available: <http://www.photonics.com/EDU/handbook.aspx?AID=25495>. [Accessed: 18-Jan-2015].
- [63] Ltschem.com, 'Hafnium Oxide,' 2015. [Online]. Available: [http://www.ltschem.com/Hafnium\\_Oxide.pdf](http://www.ltschem.com/Hafnium_Oxide.pdf). [Accessed: 18-Jan-2015].
- [64] Makeitfrom.com, 'Compare Hafnia (Hafnium Oxide, HfO<sub>2</sub>) to Polyetheretherketone (PEEK) :: MakeItFrom.com', 2015. [Online]. Available: <http://www.makeitfrom.com/compare/Hafnia-Hafnium-Oxide-HfO2/Polyetheretherketone-PEEK/>. [Accessed: 18-Jan-2015].
- [65] Engineeringtoolbox, 'Coefficient of Linear Thermal Expansion', 2015. [Online]. Available: [http://engineeringtoolbox.com/linear-expansion-coefficients-d\\_95.html](http://engineeringtoolbox.com/linear-expansion-coefficients-d_95.html). [Accessed: 18-Jan-2015].
- [66] E. Lassner and Schubert, *Tungsten*. New York: Kluwer Academic/Plenum Publishers, 1999.
- [67] Roberts, 'Optical Properties of Nickel and Tungsten and Their Interpretation According to Drude's Formula,' *Physical Review*, vol. 114, no. 1, p. 104-115, 1959.
- [68] H. Sai, Y. Kanamori and H. Yugami, 'Tuning of the thermal radiation spectrum in the near-infrared region by metallic microstructures,' *Journal of Micromechanics and Microengineering*, vol. 15, p. S243-S249, 2005.
- [69] K. Ujihara, 'Reflectivity of Metals at High Temperature,' *Journal of Applied Physics*, vol. 43, no. 5, p. 2376-2383, 1972.
- [70] M. Takagi, 'The Thickness Dependence of the Phase Transition in Thin Solid Films,' *Journal of the Physical Society of Japan*, vol. 9, no. 3, p. 3484-3487, 1986.
- [71] Q. Jiang, H. Tong, D. Hsu, K. Okuyama and F. Shi, 'Thermal Stability of crystalline thin films,' *Thin Solid Films*, vol. 32, no.1-2, p. 357-361, 1998.
- [72] P. Drude, *The Theory of Optics*. New York: Dover Publications, 1959.

- [73] Phelly.com, 'Hafnium Oxide, HfO<sub>2</sub>', 2014. [Online]. Available: <http://www.phelly.com/hfo2/>. [Accessed: 30 Oct 2014].
- [74] L. Savage, 'Property Management: A Review of Optical Materials,' *Photonics Spectra*, p. 55-58, October 2014.
- [75] N. P. Barnes and M. S. Piltch, 'Temperature-dependent Sellmeier coefficients and nonlinear optics average power limit for germanium,' *Journal of the Optical Society of America*, vol. 69, no. 1, p. 179-180, 1979.
- [76] R. F. Potter, 'Germanium (Ge),' in *Handbook of optical Constants of Solids*. Orlando: Academic Press, INC., p. 465-478, 1985.
- [77] H. H. Li, 'Refractive Index of Silicon and Germanium and Its Wavelength and Temperature Derivatives,' *J. Phys. Chem. Ref. Data*, vol. 9, no. 3, p. 561, 1980.
- [78] Soukoulis, 'Past Achievements and Future Challenges in 3D Photonic Metamaterials,' *Nature Photonics*, vol. 5, no. 523, 2011.
- [79] G. T. West, P. J. Kelly and J. W. Bradley, 'A Comparison of Thin Silver Films Grown Onto Zinc Oxide via Conventional Magnetron Sputtering and DCMS Deposition,' *IEEE Transaction on Plasma Science*, vol. 38, no. 11, p. 3057, 2010.
- [80] T. Brandt, M. Hovel, B. Gompf and M. Dressel, 'Temperature- and frequency-dependent optical properties of ultrathin Au films', *Physical Review B*, vol. 78, no. 20, 2008.
- [81] P. Winsemius, F. Kampen, H. Lenkeek and C. Went, 'Temperature dependence of the optical properties of Au, Ag and Cu', *J. Phys. F: Met. Phys.*, vol. 6, no. 8, pp. 1583-1606, 1976.
- [82] M. Moharam, D. Pommet, E. Grann and T. Gaylord, 'Stable implementation of the rigorous coupled-wave analysis for surface-relief gratings: enhanced transmittance matrix approach', *J. Opt. Soc. Am. A*, vol. 12, no. 5, p. 1077, 1995.
- [83] P. Patnaik, *Handbook of inorganic chemicals*. New York: McGraw-Hill, 2003.
- [84] S. Sellers, 'FDTD Simulation of Novel Polarimetric and Directional Reflectance and Transmittance Measurements from Optical Nano- and Micro-Structured Materials', M.S. thesis, AFIT/EE.ABET/ENP/12-M02. School of Engineering and Management, Air Force Institute of Technology (AU), Wright-Patterson AFB OH, March 2012.

REPORT DOCUMENTATION PAGE				Form Approved OMB No. 074-0188	
<p>The public reporting burden for this collection of information is estimated to average 1 hour per response, including the time for reviewing instructions, searching existing data sources, gathering and maintaining the data needed, and completing and reviewing the collection of information. Send comments regarding this burden estimate or any other aspect of the collection of information, including suggestions for reducing this burden to Department of Defense, Washington Headquarters Services, Directorate for Information Operations and Reports (0704-0188), 1215 Jefferson Davis Highway, Suite 1204, Arlington, VA 22202-4302. Respondents should be aware that notwithstanding any other provision of law, no person shall be subject to a penalty for failing to comply with a collection of information if it does not display a currently valid OMB control number.</p> <p><b>PLEASE DO NOT RETURN YOUR FORM TO THE ABOVE ADDRESS.</b></p>					
1. REPORT DATE (DD-MM-YYYY) 06-03-2015		2. REPORT TYPE Master's Thesis		3. DATES COVERED (From – To) 1 Oct 2013 – 26 March 2015	
TITLE AND SUBTITLE  COHERENT THERMAL EMISSION FROM PHOTONIC NANOSTRUCTURES COMPOSED OF TA, W, GE, AND HfO <sub>2</sub> THIN FILMS				5a. CONTRACT NUMBER	
				5b. GRANT NUMBER	
				5c. PROGRAM ELEMENT NUMBER	
6. AUTHOR(S)  Dodd, Mark T., Mr., Civ				5d. PROJECT NUMBER DAGSI RX2-AFIT-13-2	
				5e. TASK NUMBER	
				5f. WORK UNIT NUMBER	
7. PERFORMING ORGANIZATION NAMES(S) AND ADDRESS(S) Air Force Institute of Technology Graduate School of Engineering and Management (AFIT/ENP) 2950 Hobson Way, Building 640 WPAFB OH 45433-8865				8. PERFORMING ORGANIZATION REPORT NUMBER  AFIT-ENP-15-M-06	
9. SPONSORING/MONITORING AGENCY NAME(S) AND ADDRESS(ES) Dayton Area Graduate Studies Institute 3155 Research Boulevard, Suite 205 Kettering, OH, 45420				10. SPONSOR/MONITOR'S ACRONYM(S)  DAGSI	
				11. SPONSOR/MONITOR'S REPORT NUMBER(S)	
12. DISTRIBUTION/AVAILABILITY STATEMENT DISTRIBUTION STATEMENT A. APPROVED FOR PUBLIC RELEASE; DISTRIBUTION UNLIMITED.					
13. SUPPLEMENTARY NOTES This material is declared a work of the U.S. Government and is not subject to copyright protection in the United States.					
14. ABSTRACT  Combining an understanding of thin films and structure/property relationships, photonic nano-structures were developed in order to affect the spectral and directional radiative properties of coherent thermal emission. The targeted emission range was 2-20 $\mu\text{m}$ . Structures with appropriate materials in order to achieve thermal stability were designed and tested. Implementing a Finite Difference Time Domain numerical method, four truncated multilayer resonators were designed to selectively emit at certain transmissive wavelength bands of the atmosphere in 2-20 $\mu\text{m}$ . Ellipsometric measurements and models were used in order to extract the optical constants of thin layers of materials chosen for the resonator designs. These values showed significant disagreement with bulk values found in literature and were used to make more accurate theoretical predictions. A Direct Current Magnetron Sputtering technique was used to fabricate the four resonators, W-Ge-W, W-HfO <sub>2</sub> -W, Ta-Ge-Ta, and Ta-HfO <sub>2</sub> -Ta, with layer thicknesses of 10-760-145 nm, 10-701-145 nm, 9.6-728-169 nm, and 9.6-301-169 nm, respectively. Reflectance measurements were taken at room temperature and various high temperatures to investigate the thermal stability of the spectral reflectance of the structures. From these reflectance measurements, the W-Ge-W and Ta-Ge-Ta designs proved to hold up the best at higher temperatures.					
15. SUBJECT TERMS Coherence, Thermal Radiation, Nano-structures, Infrared, Thermal Stability					
16. SECURITY CLASSIFICATION OF:			17. LIMITATION OF ABSTRACT  UU	18. NUMBER OF PAGES  150	19a. NAME OF RESPONSIBLE PERSON Marciniak, Michael, PhD, USAF, AFIT/ENP
a. REPORT  U	b. ABSTRACT  U	c. THIS PAGE  U			19b. TELEPHONE NUMBER (Include area code) (937) 255-3636, ext 4529 (Michael.Marciniak@afit.edu)

Standard Form 298 (Rev. 8-98)  
Prescribed by ANSI Std. Z39-18